Fredrik Haakonsen

Optimizing of Strømhard austenitic manganese steel

Thesis for the degree of Philosophiae Doctor

Trondheim, May 2009

Norwegian University of Science and Technology
Faculty of Natural Sciences and Technology
Department of Materials Science and Engineering

NTNU
Norwegian University of
Science and Technology

Preface

This work has been carried out at the Department of Materials Technology, Norwegian University of Science and Technology between November 2004 and March 2009. The work was sponsored by the university and Scana Steel Stavanger.

Professor Jan Ketil Solberg was the supervisor during the whole period of study.

Trondheim
March 2009

_____

Fredrik Haakonsen

Acknowledgements

Abstract

In the present doctoral thesis the focus has been on two different ways to achieve improvement of the mechanical properties of an austenitic manganese steel. One of them was to introduce substrate particles and see if this could nucleate grains during solidification, giving grain refinement. The other one was to add a strong carbide forming element to the alloy, and affect the mechanical properties by precipitating carbides in the microstructure.

The base for the experiments was the steel Strømhard. Strømhard is a former patented steel produced by Scana Steel Stavanger AS. It is a modification of the Hadfield steels, and is used as a wear steel for typically handling and crushing rock and stone. As one of the main products of this company and with the expiration of the patent, an upgrade of this alloy was desired, to continue to be leading in this marked.

Cerium was chosen as the most likely grain refinement addition. As a highly reactive compound, cerium reacts with oxygen and sulfur already in the melt, forming cerium oxides and –sulfides which acts as substrate particles for melted steel to solidify on. Different amounts of additions, some times in combination with aluminum, were performed. Grain refinement was obtained in a casting added cerium in combination with aluminum, in which CeO_2 was the supposed substrate particle.

To form carbides, vanadium was added in different amounts to form various alloys. Several heat treatments were carried out, to create a microstructure with increased resistance to abrasive wear, by precipitating carbides within the grains. Increased hardness with aging after austenitizing was detected, but most of these microstructures did not improve the wear resistance. Two heat treatment procedures seemed to give promising microstructures. One of these was the standard form of heat treatment for austenitic manganese steels, which left a portion of the vanadium carbides remaining in the microstructure, the other being the standard heat treatment followed by aging at 950 °C for 200 hours, giving evenly distributed carbides within the grains. However, neither of these treatments improved the wear properties.

Table of contents

1   Introduction

Austenitic manganese steels are widely used in the mining industry and in cement production, diggers and railroads. These steels usually go under the name of Hadfield steels, [1] and contain around 12.5 % manganese and 1.2 % carbon. (All compositions in this thesis are given in weight %, unless otherwise stated.) Austenitic manganese steels combine a good ductility with a high gouging abrasion resistance and resistance to metal-to-metal wear. [2] Blows under crushing will deform the surface and give work hardening, increasing the wear resistance. Wear steels are used in components such as crushing plates and cones for ore and rock, grinding mills, power shovel buckets, pumps handling abrasive fluids, and heavily stressed railway trackwork. Considering the economic factor, these steels are superior in their designated use. Components are cast to final shape, and then austenitized and water quenched to dissolve carbides formed at solidification, so that a completely austenitic structure is accomplished.

Scana Steel Stavanger produces a group of steels under the designation Strømhard. Compared to conventional Hadfield steels, Strømhard steels have a considerable higher content of manganese and carbon, i.e. approximately 20 % manganese and 1.4 % carbon. This, in combination with additions of chromium, increases initial hardness, maximum hardness after work hardening, and wear resistance. [3]

The high manganese and carbon content in Strømhard result in a structure that solidifies with an austenitic microstructure, and lack a solid state phase transformation that could refine the grain structure during subsequent cooling and heat treatment. To obtain a finer grain structure during casting is therefore important to improve the properties of these alloys. The components made of Strømhard are usually relatively large and are cast in sand moulds, which yield segregations, large grains and large temperature gradients upon cooling. This increases the danger of hot cracking, brittleness and uneven wear properties. These conditions may be improved by a better casting procedure and a refining of the grain size, achieving an increased fraction of equiaxed grains at the expense of columnar grains, and a reduction of macro and micro segregations. Non-

1

metallic inclusions have often been regarded as negative in steels, but with a good process control and metallurgical insight it would be possible to use inclusions to achieve a finer microstructure.

As the original Strømhard has a single phase microstructure, adding particles to increase wear resistance is possible. Additions of hard phases are well known to increase abrasive wear resistance. A large number of particles in the microstructure could also increase initial hardness by a precipitation hardening mechanism, if the particles are coherent/semi coherent, or contribute to increase the strain hardening rate during use by introducing dislocation loops around incoherent particles. [4]

2 Theoretical background

2.1 *Wear of steel in the mining and mineral industries*

Wear is defined as damage to a solid surface caused by the removal or displacement of material by the mechanical action of a contacting solid, liquid or gas. [5] Except in the case of seizure and fracture, wear is a gradual process, and a slow degradation of the component will lead to reduced performance. Abrasive wear is the displacement of material from a solid surface due to hard particles or protuberances sliding along the surface. Abrasive wear can be divided into two-body and three-body abrasion. In two-body abrasion the abrading particles are fixed to one of the two surfaces in relative motion. In three-body abrasion, loose abrading particles are present between the two surfaces in relative motion. In three-body abrasion the particles have the opportunity to roll, and thereby abrade less on the surfaces. If loose particles attaches to one of the surfaces, the mechanism will change from three-body to two-body abrasion, and the wear rate can increase.

The most common damages to wear steels are abrasive wear and brittle fracture. [6] A more relevant classification of abrasive wear for mining industry is into groups of low-stress, high-stress, or impact abrasion. Low-stress abrasion does not involve fracture of the abrasive material, and typical cases are the transportation of hard particles or mediums containing such particles. The metal removal processes are scratching or micro metal removal. Hard materials are used to reduce the wear.

High-stress abrasion is encountered when hard particles are caught between two normally loaded surfaces. Examples of processes are rock crushers and ball mills. Metal removal is due to scratching and plastic deformation. High yield strength in combination with high hardness reduces the wear.

Impact abrasion is a result of direct impact and high localized pressures. This is the typical wear mechanism of shovels and pulverizing mills. The abrasive particles cuts into the metal surface, and large gouges and scratches are made. Materials with high toughness in combination with high hardness are preferred to resist this type of wear. Austenitic manganese steels are often used in these situations, as this group of steel is very tenacious, with an increase in hardness at the surface when it is deformed under use.

2.2 Austenitic manganese steel in wear parts

The first austenitic manganese steel was developed in 1882 by Robert Abbott Hadfield. [1] Hadfield had done a series of test with adding ferromanganese containing 80 % manganese and 7 % carbon to decarbonised iron. Increasing manganese and carbon contents led to increasing brittleness up to 7.5 % manganese. At manganese contents above 10 % however, the steel became remarkably tough. The toughness increased by heating the steel to 1000 °C followed by water quenching, a treatment that would render carbon steel very brittle. The alloy introduced commercially contained 1.2 % carbon and 12.5 % manganese. This composition is used even today, and the steel is still known as Hadfield steel.

Austenitic manganese steels have a proven high resistance to abrasive wear including blows and metal-to-metal wear, even though they have a low initial hardness. These steels are supposed to work harden under use and thus give a hard wear resistant surface, but it has been reported that these steels have a good wear resistance in components even without heavy mechanical deformation. [2] These steels are for instance used in mining machinery like shovels and crushers, and railway points and crossings.

Laboratory abrasive wear test methods have often low reliability compared to the industrial process, especially for manganese steels where work hardening produced by the service conditions, that are essential for wear resistance, can be difficult to simulate. Still, numerous test methods can be found in the literature. Result from laboratory tests are shown in Figure 2.1 and 2.2. [1] The results in Figure 2.1 were from a pure rolling abrasion wear test, and Hadfield steels at approximately 200 Brinell show less wear than low alloyed martensitic steel with hardness up to approximately 750 Brinell. Figure 2.2 show wear of several types of steel tested in a tumbler barrel during the fettling of steel castings. This process would induce impact to the steel, introducing work hardening, and the hardness was measured with scleroscope after the wear test giving the acquired surface hardness. This graph shows a more typical relation between wear resistance and hardness, where wear resistance increases with hardness.
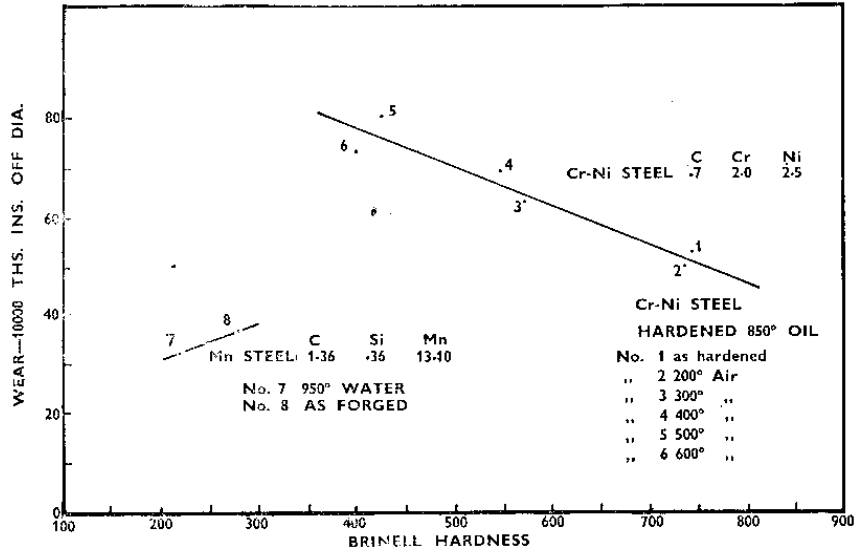
Figure 2.1. Rolling abrasion wear test of Hadfield and martensitic steels. [1]

6
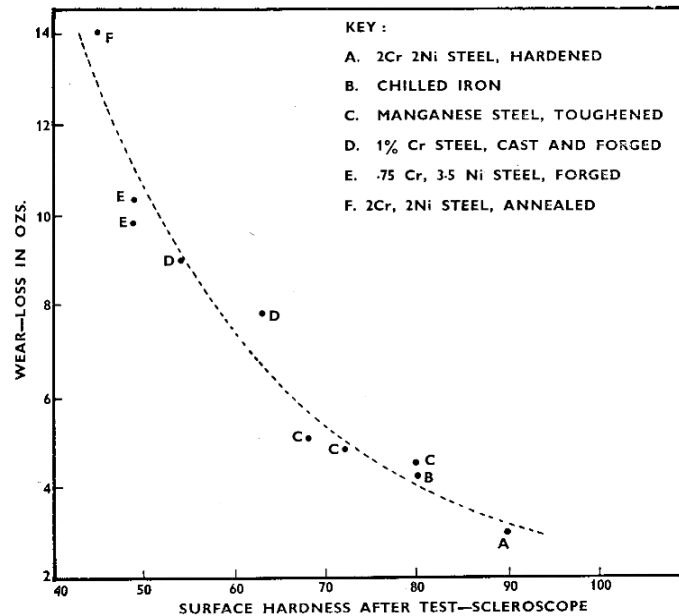
Figure 2.2. Result from tumbler barrel wear test. Graph showing relation between wear resistance and acquired hardness. [1]

To achieve the desired mechanical properties, the manganese steels have to be heat treated above the A_{cm}-line of the phase diagram, a procedure referred to as austenitizing or solution annealing, followed by water quenching. The austenitizing will dissolve carbides from the eutectic formation at the end of solidification, and also contribute to remove some microsegregation in the microstructure. The water quenching should prevent new carbides to form during cooling from the austenitizing temperature, although in larger components some precipitation must be expected. Carbide-forming elements such as chromium, molybdenum and vanadium will increase the chance of undissolved carbides or precipitation of carbides during cooling of the steel. Subsequent reheating is in general not recommended for austenitic manganese steels. Reheating between 260 °C and the A_{cm}-temperature can lead to precipitation of carbides giving embrittlement. Low carbon contents and additions of molybdenum and nickel can suppress embrittlement to some extent. [2]

7

Several mechanisms have been found to contribute to work hardening; these will be influenced by alloy composition, temperature and strain rate. Differences in composition will effect stacking fault energy and strain rate sensitivity. The mechanisms found to be present are twinning or pseudo twinning [8], stacking fault formation, and dynamic strain aging [9] [10]. Deformation-induced transformation to martensite is not found in Hadfield type manganese steels, but can be found in surface areas with reduced carbon and manganese contents, and in alloys containing approximately 0.6 % carbon and 8 % manganese. [2]

2.3   Effect of atomic elements on manganese steels

Carbon and manganese are the primary alloying elements. Typical concentrations are 0.7-1.45 % carbon and 11-14 % manganese, although Strømhard manganese steel contains approximately 20 % manganese. These two elements stabilize austenite and give solid solution strengthening. Manganese also stabilizes austenite by delaying the transformation/increasing the hardenability. A higher austenitizing temperature is needed with higher contents of carbon and manganese. [2]

The silicon content is around 1.0 %. This element has little effect on the mechanical properties if kept under this value. Amounts of 0.10 % increases fluidity during casting. Above 2.2 % silicon there is a sharp reduction in ductility and strength. [1] [2]

Chromium increases the initial hardness and the hardness after deformation. Chromium modified manganese steels usually contain 2-4 % chromium. [1] [2]

Molybdenum in the amount of 0.5-2 % improves the toughness and resistance to cracking before heat treatment. Molybdenum also suppresses embrittlement during reheating. The improvement is thought to be due to the formation of nodular carbides instead of continuous bands around austenite dendrites. By heating a standard grade manganese steel containing 2 % molybdenum for 8 to 12 hours at 595 °C and water quenching it from 980 °C, a structure of finely dispersed carbides in austenite should form, improving abrasion resistance. [2]

Vanadium is a strong carbide former. It increases yield strength with a reduction in ductility. Additions of 0.5-2 % give precipitation hardening when solution treated at 1120-1175 °C and aged at 500-650 °C [2] [11], see also section 2.4.

Nickel increases ductility and stabilizes austenite. [1] [2]

2.4 Additions of vanadium to manganese steels

There are several references on adding vanadium to manganese steels to improve the wear resistance. In Ref. [2] vanadium is said to increase yield strength, but decrease ductility. A precipitation-hardening effect is described in manganese steel on adding 0.5-2 % vanadium. Solution treatment at 1120-1175 °C, quenching and subsequent aging at 500-650 °C may increase the yield strength to 700 MPa. Borik performed tests [11] with steels of the composition of 0.3, 0.6 and 0.9 % C, 13.8 % Mn, 3.1 % Ni, 1.8 % Mo and 0.61 % V. The alloys were heat treated at 1145 °C for two hours, water quenched, and aged at 705 °C for 8 hours. These alloys showed a higher initial hardness after heat treatment compared to regular types of manganese steels. The hardness of the worn surface after gouging abrasion was similar or lower for the precipitate-hardened steel than for regular types of manganese steel. The precipitate-hardened steel also possessed a lower wear resistance than the regular Hadfield steels.

A patent has been filed by Mackay and Smith [12] on a heat treatment procedure on an alloy containing 1.1-1.4 % C, 10-14 % Mn, 1 % Si max, and 1.2-2 % V, giving an austenitic matrix structure with vanadium carbide particles substantially uniformly distributed therein. One of the heat treatments was comprised of soaking the alloy at a temperature in the range 1050-1150 °C for at least 6 hours per inch of section followed by water quenching, the other was to soak the alloy in the range of 1100-1150 °C for at least 30 minutes per inch of section, followed by water quenching, annealing at 950 °C for at least 6 hours per inch of section followed by water quenching. This patent refers to abrasive wear testing in which these alloys have up to a five fold increase in wear resistance compared to regular Hadfield steels, and Izod impact testing of the last mentioned heat treatment gave toughness values in excess of 120 foot-pounds, whereas Hadfield steel gave around 100 foot-pounds.

By using a step-aging procedure after austenitization of an alloy containing 0.8 % C-13 % Mn-1 % V, Atasoy, Ozbaysal and Inal [13] obtained carbides homogeneously distributed throught the austenitic matrix. The "step-aging" consisted of heating to 650

°C for 1 hour followed by 950 °C for 6 hours. The first step worked as a pre-aging forming precipitates above the critical size required for nucleation at the second stage. According to the article the precipitated carbides were identified as V_4C_3 with a NaCl unit cell that exhibited a cube-cube orientation relationship with the austenite.

Imai and Namekata [14] showed age-hardening in a 0.44% C-17% Mn-12% Cr-2% Ni-2.37% V austenitic steel. After a solution treatment at 1200 °C for 1 hour samples were aged at 500 °C, 600 °C, 700 °C, 800 °C and 900 °C for times up to 150 hours. For increased aging temperature the hardness peak showed up at shorter aging times. The highest hardness of 450 HV was reached after 150 hours at 600 °C and after 5 hours at 700 °C. The precipitates were confirmed to be V_4C_3, that precipitate in the relationship to the matrix definite in the orientation parallel to {110} plane in the <111> orientation. The hardness increase was related to coherency strains associated with these particles up to 160 Å. When particles grew above this size, the coherency strain was relaxed and the hardness decreased.

2.5 Refining of steel

Both in the aspect of additions of grain refiners in the melt and for the quality of the steel, the content of what is usually looked upon as unwanted elements is important to reduce and/or control. These elements are oxygen, nitrogen, sulfur and phosphorus, among others. High-alloy steels are often based on the remelting of scrap steel, so that the amount of unwanted elements in the melt will be influenced by the contents in the scrap, in addition to their contents in the alloying elements being added.

To remove oxygen dissolved in the melt, elements with a strong affinity to oxygen are added. These are typically aluminum, silicon and manganese. As manganese is a substantial alloying element in austenitic manganese steels, this element is not regarded as a deoxidizer in these steels. Silicon is in many steels used as a deoxidizer, but in manganese steels, silicon needs to be kept low because of its negative effect on ductility [1]. Aluminum is seen as the main deoxidizer, and is added either as pure aluminum or ferroaluminum, reacting with oxygen and forming Al_2O_3. Titanium is added to remove nitrogen from the melt.

2.6 Phases and phase conditions in high carbon, high manganese steels

Table 2.1 shows the composition of Strømhard high manganese steel. Aluminum is added for deoxidation, titanium is added to remove nitrogen, and silicon is introduced from the melted steel scrap. Sulfur, phosphorus, oxygen and nitrogen are unwanted impurities, and their contents should be as low as possible. For the evaluation of phases, only iron, manganese and carbon are considered. The effect of the other elements on the solidification and phase conditions are not considered important in a coarse estimate.

Table 2.1. Approximate composition of Strømhard steel. Values are in weight percent.

C	Mn	Cr	Si	Al	Ti	O	S	N	P
1.42	19.5	2.4	0.7	0.03	0.15	0.005	0.005	0.01	0.04

From the binary phase diagram in Figure 2.3 the liquidus and solidus temperatures for iron containing 20 % manganese can be found. These are respectively 1440 °C and 1425 °C, and correspond to a solidification range of 15 centigrades. The binary alloy would, according to the phase diagram, solidify with an austenitic structure that would be stable down to 500 °C, and then enter the two-phase area where ferrite would start to form. In reality, however, because of low diffusivity of substitutional atoms, this alloy would most likely stay austenitic down to room temperature.
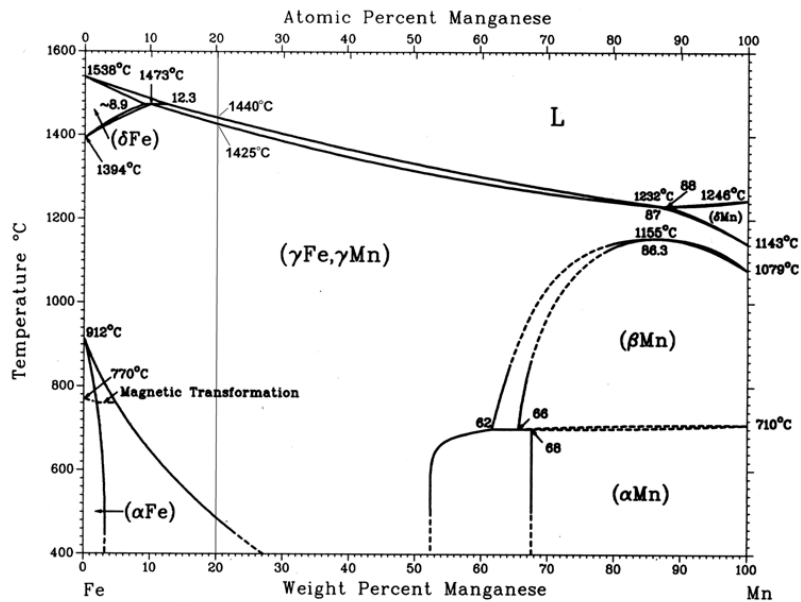
Figure 2.3. Fe-Mn phase diagram. [15] The vertical line at the left indicate a composition of iron containing 20 % manganese.

Going further to the metastable ternary iron-manganese-carbon phase diagram, the effect of carbon on the phase formation is clear. Figure 2.4 shows a vertical section with the manganese content kept constant at 20 %. Figure 2.5 shows how this section is oriented in the ternary phase diagram. From the line drawn for 1.45 % carbon (6.4 at.%) in Figure 2.4, the liquidus- and solidus temperatures can be found. These are respectively 1350 °C and 1125 °C. Carbon has thus a significant effect on the solidification range which now is 225 centigrades. The solidification range will have a large influence on the casting properties of the steel.
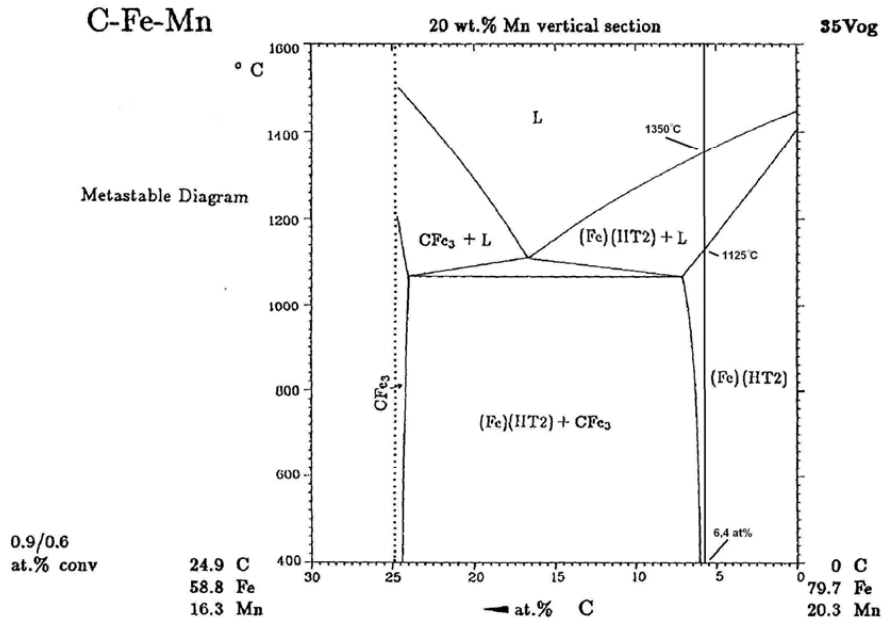
Figure 2.4. Vertical section in the metastable ternary C-Fe-Mn phase diagram at 20 % manganese. [16] The vertical line is corresponding to 1.45 % carbon. (HT2) indicates austenite phase. This phase diagram is in atomic percent.
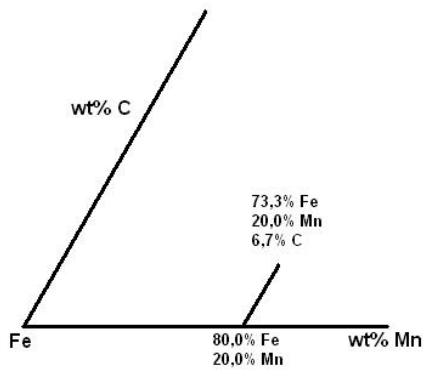
Figure 2.5. A sketch showing the orientation of the section shown in Figure 2 in the ternary C-Fe-Mn phase diagram. Values are in weight percent.

From Figure 2.4 it is also seen that the austenite is stable down too 400 °C, so the ferrite formation is even more suppressed by the addition of carbon. This is as expected as

15

carbon is a strong austenite former in steels. The possibility of attaining grain refinement by heat treatment in the solid state (normalizing), as in low alloyed steels, is not present.

2.7   Solidification of high carbon, high manganese steels

Strømhard steels are often used in large components that are cast in sand moulds. Typical components are crushing plates, with dimensions $2 \times 1 \times 0.2$ m^3 and a weight of approximately 3 metric tons, and crushing cones. As mentioned earlier, the liquidus temperature for this alloy is 1350 °C, and the casting temperature is approximately 50 centigrades above this. Solidification starts at the surface against the sand mould, and coarse columnar crystals grow into the melt towards the centre of the casting. If the total undercooling of the melt, ΔT, is large enough, equiaxed grains will start to grow ahead of the solidification front, see Figure 2.6. These will nucleate when $\Delta T > \Delta T_n$, where ΔT_n is the necessary undercooling for heterogeneous nucleation.
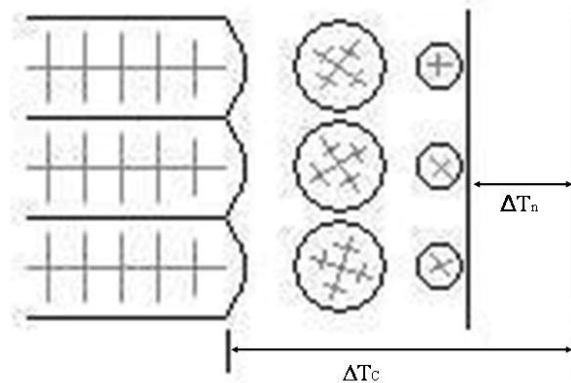
Figure 2. 6. A schematic picture of the solidification at the transition from columnary growth to growth of equiaxed grains. Columnary grains are shown on the left and equiaxed grains are shown on the right.

The very large solidification range of this steel results in considerable microsegregation. On the other hand, this will contribute to a large constitutional undercooled zone ahead of the solidification front. The degree of constitutional undercooling, ΔT_C, is expressed by the simplified formula [17]:

17

$$\Delta T_C = mC_0(k-1)\left(\frac{vr}{2D_l}\right) \qquad (1)$$

With reference to Figure 2.7, for a binary alloy, m is the slope of the liquidus line, C_0 is the concentration of the alloy in consideration, k is the distribution coefficient, v is the solidification speed, r is the radius of the dendrite tip, and D_l is the diffusivity of an alloying element in the melt. The last term in formula (1) is also known as the Péclet number, and is given by:

$$P_c = \frac{vr}{2D_l} \qquad (2)$$
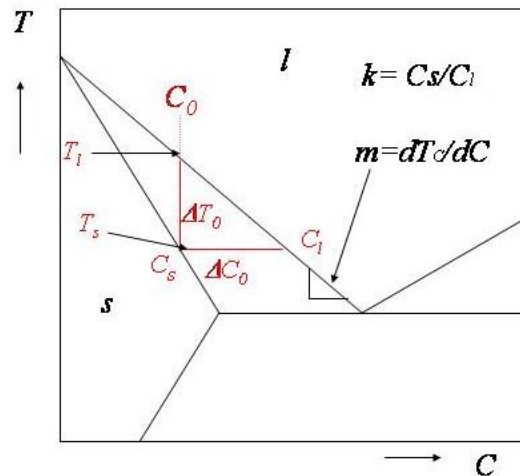
Figure 2.7. Definition of different solidification parameters which is represented in equation (1).

By dividing ΔT_C with P_C it is possible to rank the influence of the different alloying elements on the undercooling:

$$\frac{\Delta T_C}{P_C} = mC_0(k-1) \qquad (3)$$

2.8 Substrate particles in steel

Due to the lack of solid phase transformations in Strømhard steel, grain refining during casting is the only way to reduce the grain size in a cast component. Grain refining during casting may yield improvements as better resistance to hot tearing during solidification, higher ductility and toughness, better fatigue resistance, reduced porosity and better feeding of the casting. [18]

To achieve a smaller grain size and a larger fraction of equiaxed grains at the expense of columnar crystals, particles can be introduced for solid nuclei to form on. By heterogeneous nucleation, the surface-to-volume ratio of the nucleus decreases, and the new surface energy is reduced. In this way the nucleus becomes stable at a lower undercooling than for homogeneous nucleation. In aluminum, these substrate particles can be intermetallic compounds like TiB_2 that have been added to the melt. In steel, it is more common to add alloying elements that react with other elements in the melt, often elements that otherwise are considered unwanted. These elements precipitate as non-metallic inclusions above the liquidus temperature for the alloy in consideration. Examples of non-metallic inclusions that are known to promote grain refinement in steels are CeS, RE_2O_3, TiN and Al_2O_3 [19].

In reality, the degree of grain refinement that is achieved, is an interplay of several parameters that can be identified, but not quantified. Some of these parameters are the number density of substrate particles, the size distribution of substrate particles, and the wetability between metal and particle, being dependent on the local boundary surface energy. The following is a closer review of their contributions.

2.8.1 Number density of substrate particles

To achieve the finest possible equiaxed structure, as many nucleation sites as possible are wanted. The upper limit of solidified nuclei is given by the number density of substrate

particles. For a given volume fraction, f_v, the relation between number density, N_v, and particle diameter, d, is given by the formula:

$$f_v = \frac{\pi}{6} d^3 N_v \qquad\qquad (4)$$

Equation (4) applies to a monodispersive system of spheres, and shows that for such systems, the smallest possible diameter is the best way to get the highest possible number density. A small particle size is also favorable to avoid crack initiation in the finished component. The average diameter of substrate particles should be around 1 μm to give an adequate fine-grained structure, and they should be evenly distributed in the melt.

2.8.2 Size distribution of substrate particles

In the previous paragraph, there was pointed out that the substrate particles should be small, but they must not be too small. The reason for this is that the curvature of round particles introduces a barrier to nucleation, and effect the ability of the particles to act as substrates. As shown in Figure 2.8, the size of the nucleus have to be larger, as the substrate particle gets smaller, if the wetting angle is to be the same. The nucleation barrier will increase as the substrate particle gets smaller, until it loses its ability to act as a precipitating agent. The borderline case will be when the energy barrier reaches that of homogenous nucleation. It is known that the undercooling for homogenous nucleation during solidification can be as high as 200-300 centigrades, i.e. an order of magnitude larger than what is possible by constitutional undercooling.
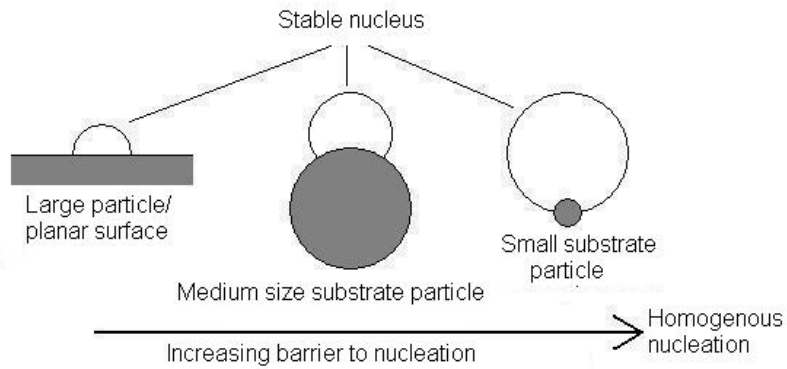
Figure 2.8. The effect of the size of the substrate particles on the energy barrier at heterogeneous nucleation. This example show nucleus on a substrate with an wetting angle of approximately 90 degrees.

From this reasoning there should be an optimum size of the substrate particles to get the finest possible equiaxed grain structure after solidification. As illustrated in Figure 2.9, the size distribution should be as sharp and narrow as possible, with an average diameter in the order of 1 μm. A distribution like this is difficult to achieve in real life because of coarsening reactions in the melt.
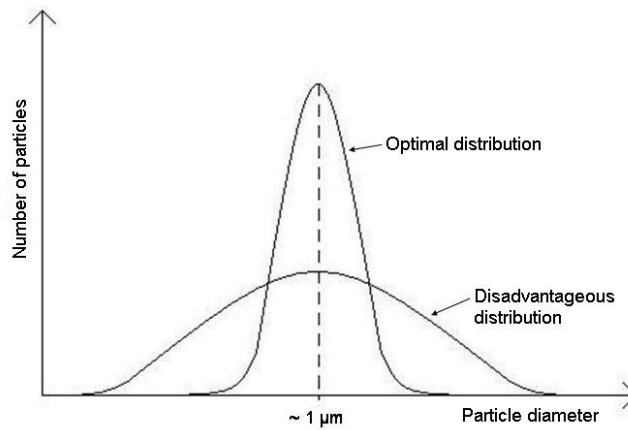

Figure 2.9. A schematic drawing of a favorable and an unfavorable size distribution of substrate particles.

2.8.3 The ability of substrate particles to nucleate a solid phase

The ability of substrate particles to nucleate a solid phase is dependent on the constitutional undercooling. Gradually, as the lattice fit decreases and the wetting angle increases, the necessary undercooling to get heterogeneous nucleation increases. As the constitutional undercooling during solidification is given by the alloy composition and the casting parameters, the substrate particles have to be operational as nucleation sites at this given undercooling to give grain refinement. For high carbon, high manganese austenitic steels, austenite has to grow epitaxialy on the substrate particles. The lattice parameter and crystal structure of the substrate particles should therefore be compatible with austenite.

From solidification theory, it is known that the energy barrier against nucleation is directly related to the wetting angle, θ. This is, as illustrated in Figure 2.10, defined as the angle between the substrate and the tangent of the nucleus surface at the rim.
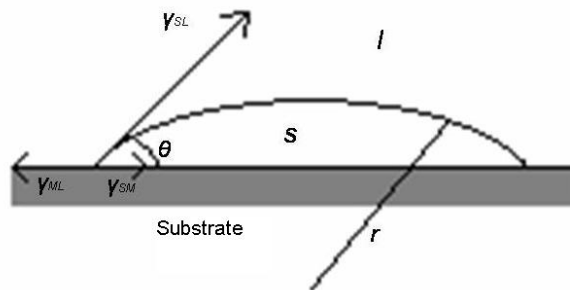
Figure 2.10. Definition of the boundary surface tension and the wetting angle. The figure shows heterogeneous nucleation of a spherical nucleus segment on a flat substrate.

For a nucleus with the shape of a spherical segment, the following relation applies between wetting angle, θ, and the boundary surface tension values between solid/liquid, γ_{SL}, solid/substrate, γ_{SM}, and substrate/liquid, γ_{ML}:

$$\cos\theta = \frac{\gamma_{ML} - \gamma_{SM}}{\gamma_{SL}} \qquad (5)$$

The energy barrier against heterogeneous nucleation, ΔG^*_{het}, is in turn connected to the wetting angle, θ, through relation [19]:

$$\Delta G^*_{het} = S(\theta)\Delta G^*_{hom} \qquad (6)$$

where ΔG^*_{hom} is the corresponding energy barrier for homogeneous nucleation, and $S(\theta)$ is a so-called shape factor, given as [19]:

$$S(\theta) = (2 + \cos\theta)(1 - \cos\theta)^2 / 4 \qquad (7)$$

It follows from equation (6) and (7) that $\Delta G^*_{het} \to 0$ when $\cos\theta \to 1$, that corresponds to full wetting $(\theta \to 0)$. In accordance with equation (5) and (7), this occurs when:

$$\gamma_{ML} \geq \gamma_{SL} + \gamma_{SM} \qquad (8)$$

Consequently, if the boundary surface tension between the nucleus and the substrate, Y_{SM}, is small enough, the energy barrier against nucleation will be sufficiently low for the new phase to form ahead of the solidification front in accordance with the sketch in Figure 4. This in turn requires a coherent or semi coherent interface with a very small mismatch. According to Bramfitt [20], the lattice mismatch, δ, can be estimated from the equation:

$$\delta^{(hkl)_s}_{(hkl)_n} = \sum_{i=1}^{3} \frac{1}{3} \left(\frac{\left| \left(d_{uvw_s^i} \cos\gamma \right) - d_{uvw_n^i} \right|}{d_{uvw_n^i}} \right) \qquad (9)$$

23

where $(hkl)_s$ is a low index plane of the substrate, $[uvw]_s$ is a low index direction in $(hkl)_s$, $(hkl)_n$ is a low index plane in the nucleus, $[uvw]_n$ is a low index direction in $(hkl)_n$, $d[uvw]_n$ is the inter atomic spacing along $[uvw]_n$ and γ is the angle between $[uvw]_s$ and $[uvw]_n$.

In the literature, there seems to be no report on how the undercooling, ΔT, during solidification is related to the lattice mismatch, δ, for steels that solidify with an austenitic structure, but for ferritic steels this connection is known. As shown in Figure 2.11, substrate particles of the type CeS, CaS, TiN and TiC can nucleate ferrite at an undercooling in the order of 1 centigrade or lower. These particles have a mismatch to ferrite of less than 5 %.
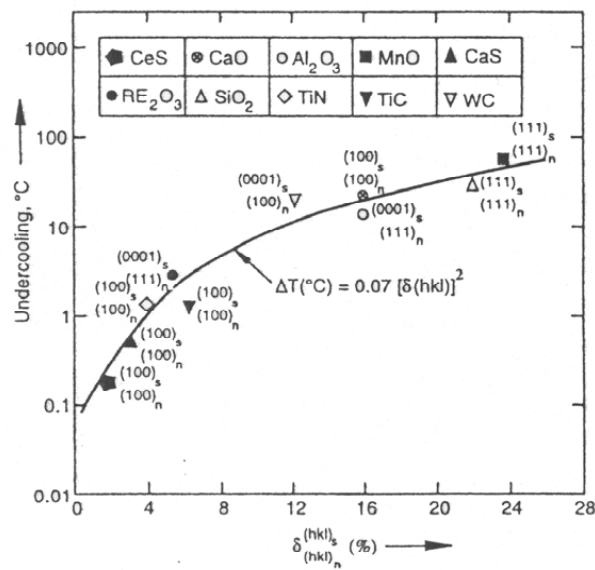

Figure 2.11. The relation between undercooling and mismatch for different inclusion in a ferritic steel. [21]

24

2.9 Previous results on grain refinement of steels

Previous research on grain refinement of steels has primary been focused on steels that solidify as δ-ferrite. The reason for this is most likely the fact that ferritic steels have the largest share of the marked. Even many of the austenitic steels solidify as δ-ferrite, so also for these steels, the δ -ferrite is decisive for achieving grain refinement. In all these cases the substrate particles must nucleate ferrite to give grain refining. Examples of non-metallic inclusions that nucleate ferrite, are titanium oxides and -nitrides and various types of cerium-/lanthanum containing oxides and sulfides [21]. Cerium and lanthanum are usually added in the melt as REM (Rare Earth Metals), or Mischmetal, a designation used for an alloy containing rare earth species in the same relative amounts as in nature, i.e. approximately 50 % cerium, the rest being lanthanum, neodymium and others.

Cerium has also been added to austenitic stainless steels with good result. For instance, by adding 0.4 % cerium to an austenitic steel containing 25 % chromium and 20 % nickel, a prominent reduction in grain size was obtained compared to in the same alloy without cerium additions, as shown in Figure 2.12.
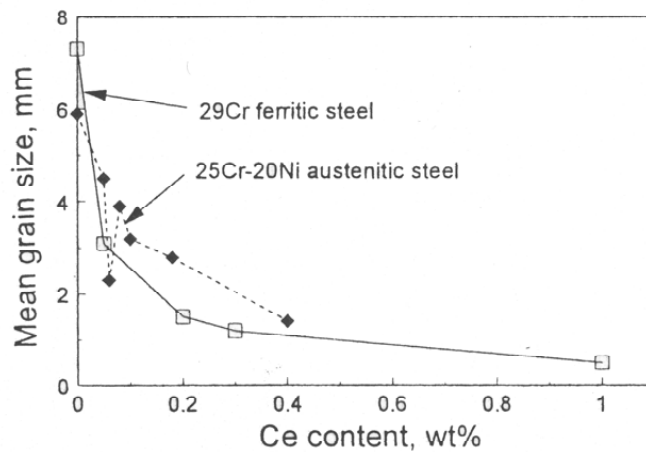

Figure 2.12. The effect of cerium on grain size in a 25 %Cr-20 %Ni austenitic steel and a 29 %Cr ferritic steel after solidification. [22]

25

Recently, experiments have been carried out with grain refinement of 254 SMO, a super-austenitic stainless steel of composition 20 % chromium, 18 % nickel and 6 % molybdenum [23]. This is a steel that solidifies completely austenitic and undergoes no phase transformation in solid state. Under these circumstances, grain refinement during solidification is of great importance to improve the mechanical properties. In the experiments with grain refinement of 254 SMO, two full scale trials of 5 tons were conducted at Scana Steel Stavanger, i.e. one reference casting in which cerium and lanthanum were added as Mischmetal, and one casting to which a preconditioner was added. The preconditioner was added in an amount of 3.5 kg per ton steel, and consisted of 32.0 % chromium, 17.6 % silicon, 8.7 % cerium, 1.24 % carbon and iron balance. It is standard practice at Scana Steel to add Mischmetal to 254 SMO. The results showed a considerable refinement of the dendrite structure in the alloy added with preconditioner, compared to the reference casting with only Mischmetal added. At the same time, a significant improvement in the forging properties was accomplished, eliminating cracking along primary crystal boundaries. Analysis of the particles that refined the structure, showed that they were $AlCeO_3$ in the test alloy and $Ce_{0.73}La_{0.27}O_{1.87}$ in the reference alloy. The former phase has a very low mismatch towards austenite, as shown in Table 2.2, which explains why the additions improved the casting.

Table 2.2. Calculated mismatch between austenitic steel and observed oxides in 254 SMO produced at Scana Steel Stavanger. [23]

	Lattice parameters 293 K	Lattice parameters (1773 K)	Mismatch to austenite	Orientation
Austenite	0.356	0.368		
$AlCeO_3$	0.3767 (a)	0.382	3.82 %	$(100)_\gamma//(100)_{AlCeO3}$ $[100]_\gamma//[100]_{AlCeO3}$
	0.3797 (c)	0.385	4.65 %	$(100)_\gamma//(001)_{AlCeO3}$ $[100]_\gamma//[001]_{AlCeO3}$
$Ce_{0.73}La_{0.27}O_{1.87}$	0.549	0.557	6.26 %	$(100)_\gamma//(111)_{CeLaO2}$ $[001]_\gamma//[110]_{CeLaO2}$

These studies clearly show that especially cerium has a grain refining effect in austenitic steels.

The lattice disregistry between austenite and $CeAlO_3$, CeO_2 and TiN versus temperature is shown in Figure 2.13. [24] Disregistry between austenite and Ce_2O_2S is also presented, but only at a low temperature.

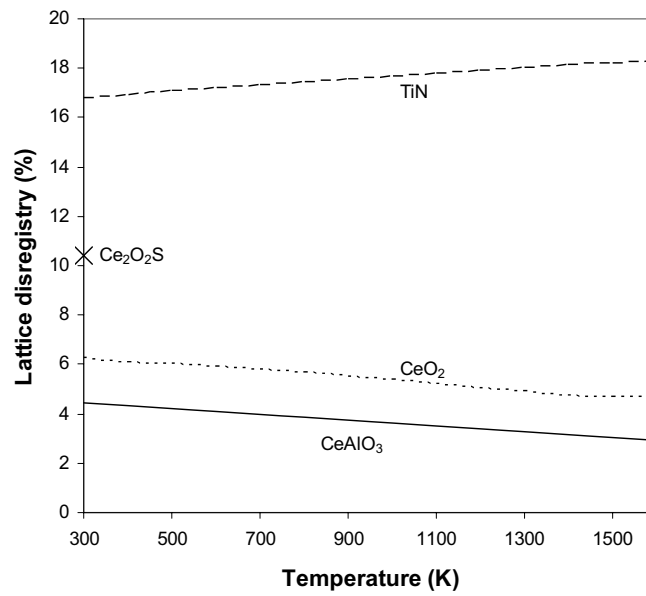**Figure 2.13. Planar lattice disregistry between austenitic steel and selected non-metallic inclusions versus temperature. [24]**

3   Experimental procedure

In this work, the focus has been on developing the alloy composition of an austenitic manganese steel. The base alloy is called Strømhard, and it is a modified Hadfield steel produced by Scana Steel Stavanger. The trials have been divided into two paths. One of them has focused on grain refinement, as this is a well-known way to improve mechanical properties of most steels, especially of cast steel structures. A commercial cerium-based grain refiner produced by Elkem Bjølvefossen, Ålvik, was used for this purpose. The other focus has been on improving the abrasive wear resistance by introducing particles. As Strømhard contains a relatively high amount of carbon, carbides was an obvious particle type to concentrate on. The carbide former tested was vanadium.

The basis for the experiments was remelting and casting of Strømhard steel with selected additions, followed by microstructure and chemical analyze of the cast and heat treated samples. Hardness and wear testing have also been conducted.

Nine large scale castings were produced at Elkem Bjølvefossen with different additions of grain refiner, including one reference casting. Preliminary tests on laboratory scale with grain refiners were performed first as a base, but the results from these tests are not included here. All of the tests with carbide formers were conducted at NTNU in Trondheim, on laboratory scale. Three alloys containing vanadium and one reference alloy were produced.

3.1 Pilot scale grain refiner experiment

Cerium in the form of an iron-chromium-silicon-cerium alloy was chosen as a grain refiner for these tests. This alloy is produced by Elkem under the name Elkem Grain Refiner (EGR). EGR is commercially available and have been tested in austenitic stainless steels with positive results. [23] Cerium is a very reactive element, on a level with aluminum, and form oxide- and sulfide compounds. The EGR alloy was in the form of crushed pieces in a size of 2-20 mm.

The basis for the experiments in the large scale tests was scrap/returns from production of Strømhard steel from Scana Steel Stavanger. At Scana Steel, the steel was melted in an electric arc furnace, where alloying elements were added to get an approximate chemical composition. The melted steel was then pored into a ladle, and alloying additions and deoxidation agents in the form of ferroaluminum and ferrotitanium were added prior to casting in sand moulds. It was not possible to estimate an exact chemical composition of the steel before remelting, as the scrap/returns were taken from different batches, but as they came from regular production, the composition should be within the specification for the Strømhard alloy.

The melting was done in a high frequency induction furnace at Elkem Bjølvefossen. The pieces of steel were cut and sandblasted before remelting. They were placed in the furnace before the heating started. The furnace had a maximum capacity of 2 tons. Steel for the whole test was melted together to reduce differences in chemical composition between the different castings. The ladle used for casting was preheated for three hours with a propane burner. The ladle had a capacity of approximately 300 kg steel, and was transported by a crane during the experiment. The samples to be cast were massive with dimensions $270 \times 150 \times 270$ cm^3. A drawing of the model used to make the sand moulds is shown in Figure 3.1. The sand moulds were made of olivine sand, 30 % new and the rest regenerated. There was added 3 % binder. The binder was of the type Carsil 2000, and the hardener was of the type Permasil. There were two castings in each mould. 1300 kg steel was heated to 1600 °C, and for each test, 120 kg steel was pored into the ladle. The

amount of steel in the ladle was weighted by a scale, on which the ladle stood during tapping. The grain refiner and deoxidizing agents were added during tapping from the furnace to the ladle. The ladle was then transported to the mould, the temperature was measured, and the metal was cast in the sand mould. If the temperature of the melt was higher than the wanted casting temperature, the casting was delayed until the correct temperature was reached. The castings were removed from the mould when they had cooled down. Do to shortage of steel, only nine out of ten castings were conducted, and the ninth was poured from a too low temperature.
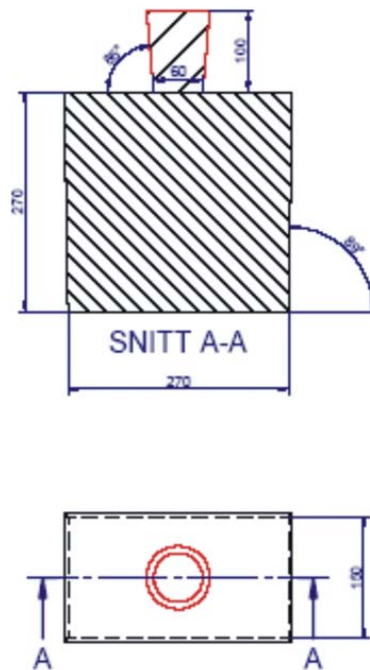
Figure 3.1. Construction drawing of the sand moulds. The upper sketch is a section of the side view and the lower sketch is the top view. The sketch was drawn by Scana Steel Stavanger.

In a preliminary experiment there was conducted a test to measure the cooling rate of a corresponding casting. Three S-type thermocouples were mounted inside AlSint tubes and placed inside a sand mould. The thermocouples were located vertically from the top,

one in the middle, one close to the mould wall, and one between these two. The tip of the thermocouples was approximately 14 cm from the top of the casting. The casting procedure was the same as described above. This casting was done without any extra additions.

The additions to the different castings of the grain refinement experiment are given in Table 3.1. The additions were made with EGR containing 10 % cerium, 20 % silicon, 35 % chromium and 35 % iron. Aluminum was added as ferroaluminum (FeAl) containing 38 % aluminum, and titanium was added as ferrotitanium (FeTi) containing 70 % titanium. Casting 1 was not added any elements. Casting 2 was alloyed with 0.1% aluminum and 0.4 % titanium. This is the same addition that is used in Strømhard at Scana Steel Stavanger. Casting 3, 4 and 5 were alloyed with increasing amounts of cerium, respectively 0.03 %, 0.06 % and 0.12 % cerium. Casting 6 was alloyed with 0.06 % cerium and 20 ppm boron in the form 35 % ferroboron. Casting 7 was alloyed with 0.06 % cerium and 0.05 % aluminum. Casting 8 was alloyed with 0.12 % cerium and 0.02 % aluminum.

Table 3.1. Additions of grain refiner and deoxidizer to the experimental castings. Values are in weight percent.

Casting	%EGR (10%)	%Ce	%FeAl (38%)	%Al	%FeTi (70%)	%Ti
1	-	-	-	-	-	-
2	-	-	0.26	0.1	0.57	0.4
3	0.3	0.03	-	-	-	-
4	0.6	0.06	-	-	-	-
5	1.2	0.12	-	-	-	-
6	0.6	0.06	-	-	-	-
7	0.6	0.06	0.13	0.05	-	-
8	1.2	0.12	0.053	0.02	-	-

After casting, a vertical section of approximately 150 mm width, 270 mm height and 10 mm thickness was cut with a water jet cutting machine, from the centre of each casting. These plates were cut with a Struers Discotom 5 to get smaller samples.

3.2 Laboratory scale experiment with carbide-forming elements

The basis for these experiments have been blocks of cast Strømhard steel from Scana Steel Stavanger, produced as described in section 3.1. The steel was remelted and added alloying elements in a laboratory furnace.

The received castings were cut to blocks of appropriate size to fit an AlSint crucible. The AlSint crucible had internal dimensions of 60 mm in diameter and 105 mm in height, and external dimensions of 65 mm in diameter and 107 mm in height. This crucible was then placed inside a graphite crucible with internal diameter 67 mm, internal height 127 mm, external diameter 100 mm and external height 145 mm. The main purpose of the graphite crucible was to protect the furnace if the AlSint crucible broke, but an additional effect was the heat source produced by the induction heating of the graphite. On top of the graphite crucible there was mounted a graphite lid to act as a hot topping. A hot topping is a source of heat on top of the crucible to reduce the problem of solidification of the melt surface which would give locations of shrinkage deep inside the casting. The graphite lid was 100 mm in diameter and 26 mm thick. The temperature was measured with an S-type thermocouple (Pt – Pt-10%Rh). The thermocouple was protected by an AlSint tube. It was placed in the crucible before heating, and went through a hole in the lid.

The applied furnace was a Balzers induction vacuum furnace. After the crucible with the steel block and alloying elements had been placed inside the induction coil, the chamber was sealed and evacuated to 0.2 mbar pressure and purged with argon to 500 mbar pressure three times. The purpose of this procedure was to remove as much as possible of oxygen in the chamber. The metal was heated to approximately 1200 °C in an argon atmosphere, and then the chamber was evacuated to remove gasses in the melt. When the melt reached 1600 °C, the chamber was filled with argon to atmospheric pressure and the furnace switched off.

The crucible with the casting was removed after 1-2 hours. Cutting was done with water-cooled abrasive cutting in a Struers Discotom 5, and wire electrical discharge machining (EDM) in a Makino U53K.

Three castings with vanadium additions and one reference alloy without additions were made. The additions are given in Table 3.2. Manganese was added to compensate for manganese loss during melting. Aluminum was added in the form of ferroaluminum to reduce porosity that would harm the mechanical properties.

Table 3.2. Additions to the laboratory castings. Vanadium was added as 50 % FeV, aluminum as 38 % FeAl and carbon and manganese as pure materials. Values are in weight percent.

Alloy	V	C	Mn	Al
1	-	-	1 %	0.1 %
2	1 %	-	1 %	0.1 %
3	1 %	0.2 %	1 %	0.1 %
4	2 %	-	1 %	0.1%

3.3 Heat treatment

The standard Strømhard alloy was austenitized at 1120 °C for 4 hours, as is the industrial procedure. The Strømhard alloyed with vanadium was austenitized at 1180 °C for 4 hours to dissolve the more stable carbides. A muffle furnace with purging argon gas was used for these heat treatments. After austenitizing the samples were water quenched.

The precipitation treatment/aging was performed in salt baths for temperatures of 500 and 600 °C, and in muffle furnaces for 700, 800, 900 and 950 °C. To avoid oxidation and decarburization, the samples that were annealed in the muffle furnace, were packed in thin steel foils or in evacuated glass ampoules. When the heat treatment was finished, the samples were water-cooled. Aging times of 8, 24 and 200 hours was used.

The purpose with the aging was to study the development in microstructure, hardness and wear resistance with increasing aging time. Experimental scatter due to macrosegregations was eliminated by applying the same specimen for all aging times at the same temperature. For each aging condition, the mentioned material properties were evaluated before the aging was resumed. An exception was the aging performed at 950 °C. These experiments were performed later than the others, and separate specimens were aged for 8 and 200 hours.

3.4 Light microscopy

For light microscopy, the samples were ground with a Struers Rotoforce-4 / Rotopol-31 automatic sample grinding machine. The abrasive mediums were MD piano 80, 220 and 1200 diamond discs from Struers. Polishing was performed in a Struers Tegraforce-5 / Tegrapol-31 / Tegradoser-5 automatic sample polishing machine. The polishing mediums were of the type Struers Diapro DAC and NAP-B. Etching was done in 2 % Nital for 60 seconds, followed by washing with ethanol and drying. A Leica MeF4M microscope attached with a Progress 3000 digital camera was used to record micrographs.

3.5 Hardness testing

The microhardness measurements were done with a Leica VMHT MOT. Six impressions were made in each phase in the microstructure to get an average value. The weight was 100 g, the speed of indenter was 60 μm/sec, and the holding time was 15 seconds. The readings were done by using an objective lens of 100 times magnification. Hardness impressions should be at least 2×diameter from the nearest neighbor impression or another phase, and this principle was followed as far as possible.

3.6 Abrasive wear testing

The abrasive wear tests was, in the lack of a standardized wear test machine, done in a six-specimen Struers Rotoforce-4 metallographic grinding machine, applying FEPA P#80 SiC abrasive paper (~200 μm particle size) of 300 mm diameter. Steel samples of 1 cm^2 were cast in Struers EpoFix embedding system with a diameter of 25 mm, to fit the sample holder. As the weight loss of plastic should be proportional to the weight loss of steel, the total weight loss was measured. In this machine the pressure is the same for all six pistons, but the samples were also systematically moved in position to compensate for a possible difference in pressure. The force on each piston was 30 N. Six samples were tested each time, and every 30 seconds the positions were changed and the grinding paper was exchanged to a new. For each aging condition, this was done a total of six times with weight measurements every second time, applying a Sartorius CP324S weight of 0.1 mg accuracy. Seen from above, the grinding disk with the SiC paper rotated counterclockwise at 150 RPM, and the sample holder rotated clockwise. Before each weighing, the samples were successively washed in water, in ethanol, and in an ultrasonic bath for 5 minutes, and finally they were dried at 50 °C for 30 minutes.

3.7 Chemical analysis

Chemical analysis was done with an Optical Emission Spectrograph (OES) at Scana Steel Stavanger. Two- three parallel analyses were performed on each sample. For the alloys produced in the laboratory, both a piece from the top and from the bottom where analyzed to map segregation. Inductively Coupled Plasma Mass Spectroscopy (ICP-MS) was used to detect cerium.

3.8 TEM

Specimens for transmission electron microscopy (TEM) were prepared by first cutting thin sheets of approximately 300 μm thickness by wire EDM. The sheets where ground down to 50-100 μm. A specialized tool was used to punch circular TEM-foils from these sheets. These were then dimpled to 25-30 μm in a Gatan model 656 dimple grinder, and ion thinned in a Gatan Precision Ion Polishing System (PIPS) using 4° angle of incidence and 4KeV accelerating voltage.

For imaging and diffraction studies, a conventional Philips CM30 TEM was applied. A JEOL 2010F was used for EDS analysis in addition to imaging. This microscope was equipped with a field emission electron gun, making it capable to work with a probe diameter of ~1nm for the analysis. An annular dark-field detector in the JEOL 2010F was used to get atomic number contrast from small carbide precipitates. Both instruments were operated at 200kV.

3.9 EPMA/SEM/EBSD

Samples for Electron Probe Micro Analysis (EPMA), Scanning Electron Microscopy (SEM) and Electron Backscatter Diffraction (EBSD) were first ground and polished as for light microscopy. The samples where then ion etched in an Ion Tech ion etcher, applying the parameters 15° angle of incidence, 4kV accelerating voltage and 4mA beam current for 2 hours.

Overview micrographs of cerium inclusions were taken in a Zeiss Ultra 55 SEM, applying a Back Scatter Detector (BSD) to get atomic number contrast. In BSD-imaging, phases containing heavy atoms will show up with a higher intensity than phases of a lower atomic number. The acceleration voltage was 15 kV, and the working distance was 5 mm. The area of each micrograph was 571 μm by 412 μm, and 10 micrographs of each casting were recorded. Particle clusters smaller than approximately 30 μm was counted as

one particle, as such clusters were not expected to give additional grain refinement compared to single particles. Counting of particles was only done for the castings containing cerium additions.

EPMA was performed in a Jeol JXA-8500F Hyperprobe, equipped with 5 Wavelength Dispersive X-ray spectrometers (WDS). The acceleration voltage was 15 kV, and the beam current was 30 nA.

3.10 XRD

The instrument used for the X-Ray Diffraction (XRD) was a Siemens D5005 powder diffractometer equipped with a Cu K-alpha radiation source and a secondary monochromator. Data were collected from 20-85 degrees 2-theta using a variable divergence slit set to illuminate a 6mm section of sample at all collection angles.

4 Results

4.1 Grain refining of Strømhard

4.1.1 Chemical composition

Chemical compositions measured with Optical Emission Spectrograph (OES) are given in Table 4.1. The castings were cast in the order they are listed. The contents of carbon, silicon, manganese, sulfur, phosphorus and chromium are similar for the different castings. The contents of carbon and manganese are lower for the experimental castings than for the standard Strømhard alloy that should contain 1.42 % carbon and 19.5 % manganese. Aluminum and titanium are found in all castings, even if not added. This is residue from the production of the steel at Scana Steel Stavanger. In casting 2, the aluminum and titanium contents are higher than in the others, as expected as this casting was added these elements. The nitrogen content in this casting is also lower than in the others, because of the reaction with the added titanium to form TiN that subsequently was removed by settling to the slag. The high contents of aluminum and titanium in casting 3 are most likely residues in the ladle from casting 2. Casting 7 and 8 have a higher content of aluminum as a result of additions. The higher amount of aluminum in casting 8 compared to in casting 7, even though the former was alloyed with less aluminum than the latter, is again likely to be caused by residue in the ladle from the previous casting.

Table 4.1. Chemical composition measured with Optical Emission Spectrograph. Values are in weight percent.

Casting	C	Si	Mn	S	P	Cr	Al	Ti	N
1	1.29	0.33	18.0	0.005	0.043	2.42	0.002	0.004	0.023
2	1.31	0.33	18.0	0.004	0.042	2.42	0.043	0.098	0.010
3	1.31	0.36	17.9	0.005	0.041	2.48	0.016	0.050	0.035
4	1.31	0.38	17.8	0.004	0.040	2.60	0.005	0.005	0.027
5	1.28	0.49	17.7	0.004	0.038	2.78	0.005	0.004	0.027
6	1.29	0.34	17.8	0.004	0.041	2.60	0.002	0.003	0.029
7	1.30	0.31	17.9	0.004	0.041	2.56	0.015	0.004	0.029
8	1.27	0.40	17.6	0.004	0.042	2.80	0.019	0.003	0.029

Table 4.2 shows the casting temperatures for the different castings, measured grain size, cerium and boron content measured with Inductively Coupled Plasma Mass Spectroscopy (ICP-MS), yield of cerium, result from particle counting, and the length of the columnar zone. The casting temperature for casting 1 was not measured, but is expected to be in the lower region as this was in the start of the experiment and the ladle was not fully heated. Castings 3, 6 and 8 had lower casting temperatures than the other castings. The grain sizes of casting 1 and 8 were quite small, the grain size in casting 2 was intermediate, and the grain sizes of casting 3, 4, 5, 6, and 7 were high. Increasing amounts of cerium from casting 3 to casting 5 is as expected, from the amounts being added (Table 3.1). Castings 4, 6 and 7 were added the same amount of cerium, with small differences in the remaining content. Castings 5 and 8 were also added the same amount of cerium, with a little higher content remaining in casting 8, probably due to the extra aluminum added to casting 8, being available to react with oxygen. Yield of cerium is for all castings between 30 % and 52 %. Boron content was unexpectedly high for all castings, with the highest content in casting 6. Casting 6 was added 20 ppm boron extra. The numbers of particles in the castings added cerium are given in the right column. As only cerium based particles where counted, there are no result for castings 1 and 2. The highest number of particles is found in casting 8. The columnar zone was shortest for casting 1 and 8.

Casting	Casting temp	Grain size	Ce (Yield)	B	Part./mm^2	Col. zone
1	-	320 µm	-	0.015	-	0.66 mm
2	1425 °C	570 µm		0.014	-	1.3 mm
3	1411 °C	930 µm	0.009 (30%)	0.014	49	1.0 mm
4	1425 °C	820 µm	0.025 (42%)	0.018	81	1.2 mm
5	1427 °C	970 µm	0.037 (31%)	0.020	157	0.83 mm
6	1407 °C	810 µm	0.031 (52%)	0.022	50	1.2 mm
7	1424 °C	1060 µm	0.021 (35%)	0.017	97	1.3 mm
8	1402 °C	270 µm	0.050 (42%)	0.020	188	0.69 mm

4.1.2 Macro- and microstructures of castings

Photographs of the vertical disks taken from the 270 mm ×150 mm × 270 mm castings are shown in Figure 4.1-4.8. The images are rotated 90°, so the top of the casting is to the right. The disks are approximately 270 mm high and 150 mm wide. Castings 1, 6 and 8 had external shrinkage in center thickness from solid feeding, and casting 2, 3, 4, 5 and 7 had considerable shrinkage cavities from liquid feeding to the rest of the casting.

Figure 4.1. Section of casting 1.

Figure 4.2. Section of casting 2.

Figure 4. 3. Section of casting 3.

Figure 4.4. Section of casting 1.

Figure 4.5. Section of casting 5.

**Figure 4.6. Section of casting 6.**

Figure 4.7. Section of casting 7.

Figure 4.8. Section of casting 8.

The macrostructure of the different alloys are shown in Figure 4.9-4.16. The bottom of each casting is seen to the left, and the distance from the bottom increases to the right. 30 mm of the sample are shown in the image. The unit of the scale bar is millimeter. The black and blue areas are austenitic dendrites, whereas the bright areas are eutectic structure comprised of carbides and austenite between the dendrites. The dendrites show up as black structures with one long primary dendrite arm, with short secondary dendrite arms sticking out perpendicular to the direction of the primary dendrite arm. This "tree"

41

is then surrounded by the eutectic structure, having a white-gray color. In castings 2, 3, 4, 5, 6 and 7 (Figure 4.10-4.15) dendrites are clearly visible in the images. In castings 1 (Figure 4.9) a few dendrites can be seen. In casting 8 (Figure 4.16), the structure seem to be too fine to show the typical dendrite trees in the structure. From these images it appears that casting 8 has a finer macrostructure than the other castings. The macrostructure seems to get coarser approximately 5 mm from the bottom for all castings except for casting 8 which seems to retain this fine structure in the whole sample. The columnar zones close to the surface (c.f. Figure 2.6) are not visible on these images, because of rounding of the samples during the metallographic preparation.
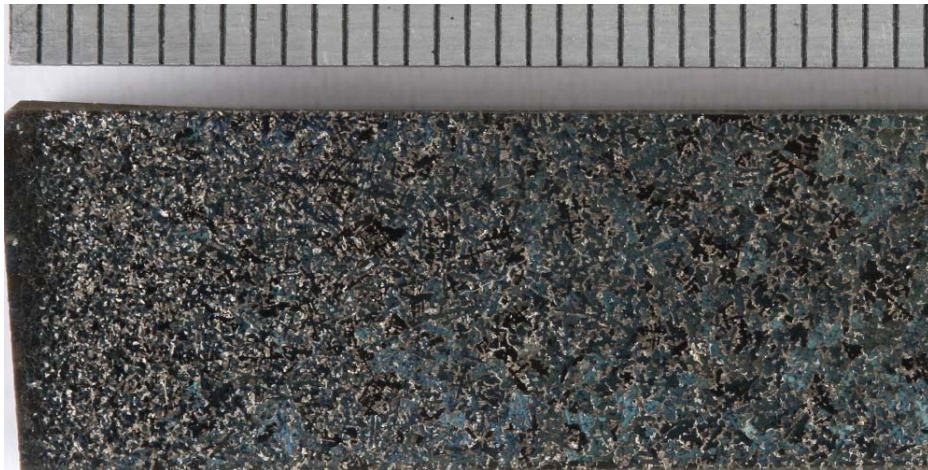
Figure 4.9. Macrostructure of casting 1. (Scale bar unit 1mm.)
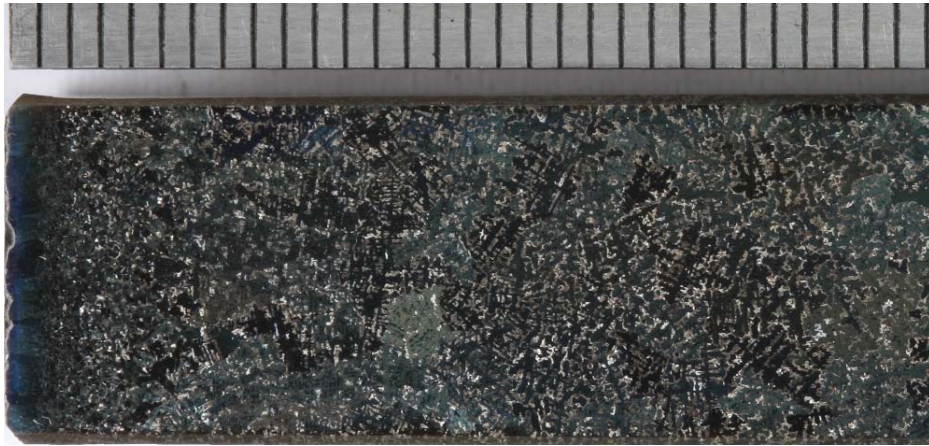
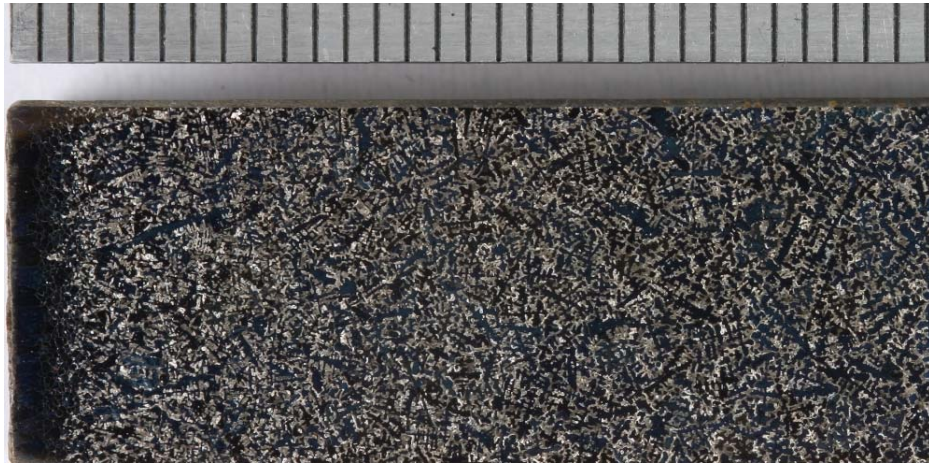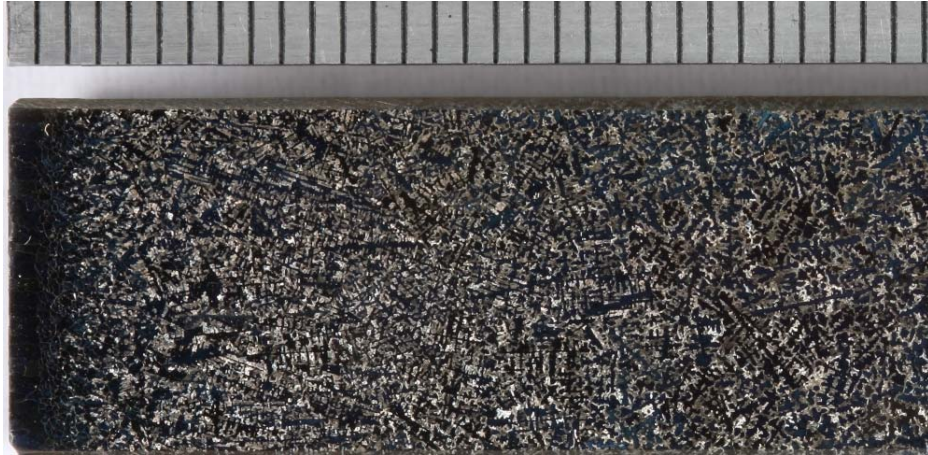**Figure 4.10. Macrostructure of casting 2. (Scale bar unit 1mm.)**
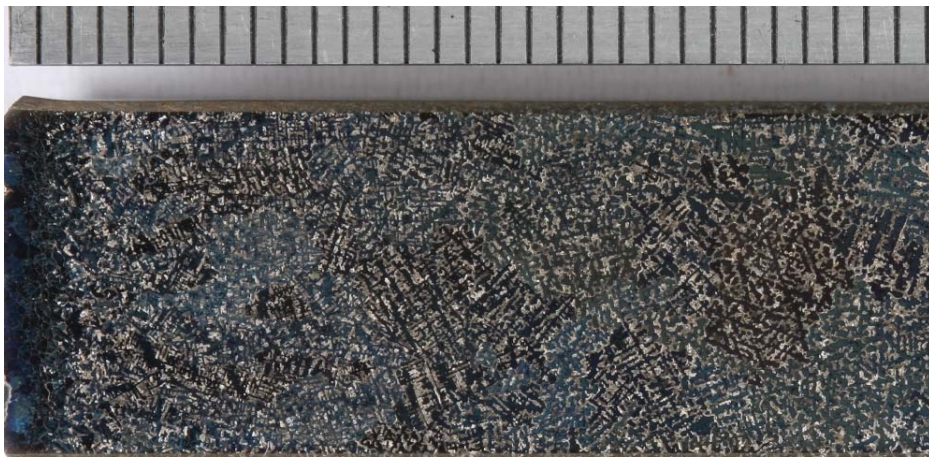
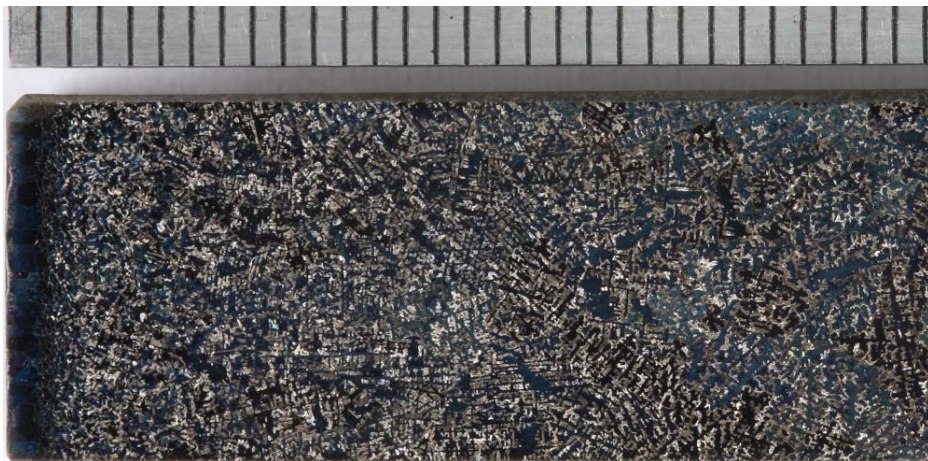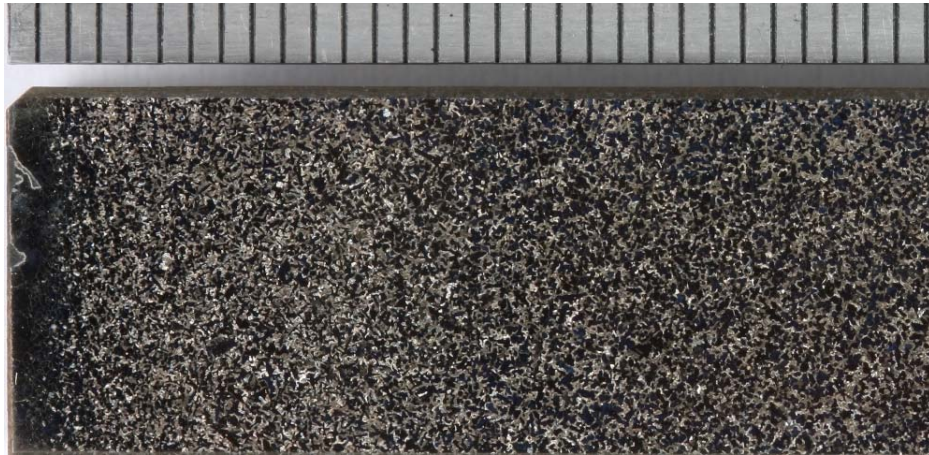**Figure 4.11. Macrostructure of casting 3. (Scale bar unit 1mm.)**

Figure 4.12. Macrostructure of casting 4. (Scale bar unit 1mm.)

Figure 4.13. Macrostructure of casting 5. (Scale bar unit 1mm.)

Figure 4.14. Macrostructure of casting 6. (Scale bar unit 1mm.)

Figure 4.15. Macrostructure of casting 7. (Scale bar unit 1mm.)

45

Figure 4.16. Macrostructure of casting 8. (Scale bar unit 1mm.)

Figures 4.17 to 4.24 show the as-cast microstructures of the eight castings. These micrographs provide a better basis for analyzing the effect of the grain refiners than the macrographs do. Each casting has an austenitic microstructure with a eutectic structure along grain boundaries. The eutectic structure consists of carbides and austenite. The austenite matrix show up white/brown in the images, and the eutectic is black with white areas within. All austenitic manganese steels are used in the heat treated condition, and the austenitization treatment remove practically all of the eutectic structure. The brighter areas in the austenite matrix are a sign of microsegregation, and these areas are higher in alloying elements. Casting 8, Figure 4.24, has clearly smaller grains than the other castings.
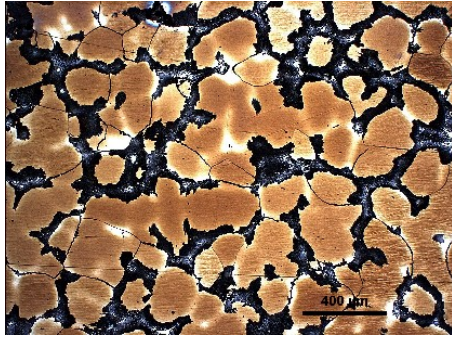
Figure 4.17. Microstructure of casting 1.
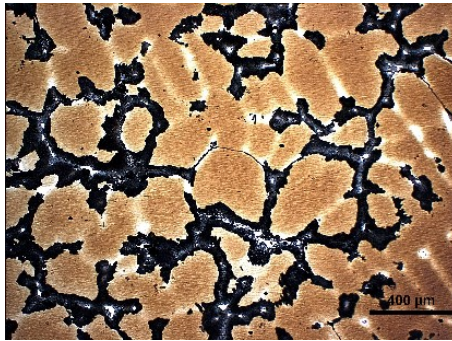

Figure 4.18. Microstructure of casting 2.
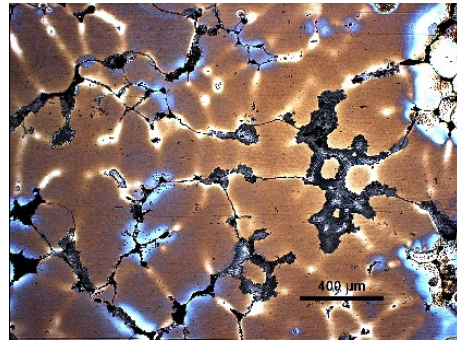

Figure 4.19. Microstructure of casting 3.

Figure 4.20. Microstructure of casting 4.

Figure 4.21. Microstructure of casting 5.
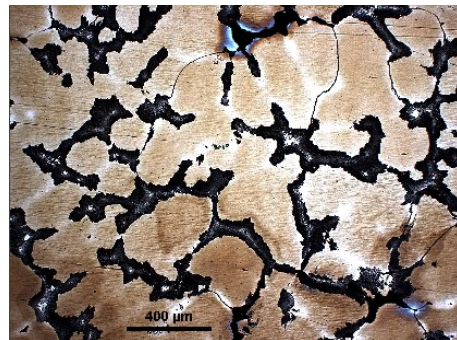

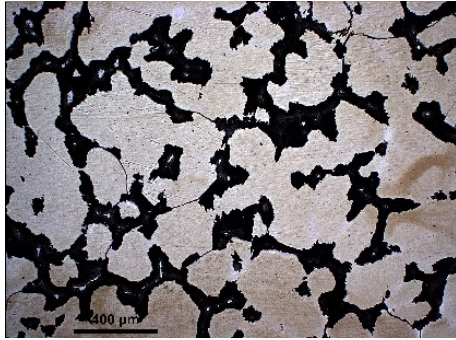**Figure 4.22. Microstructure of casting 6.**

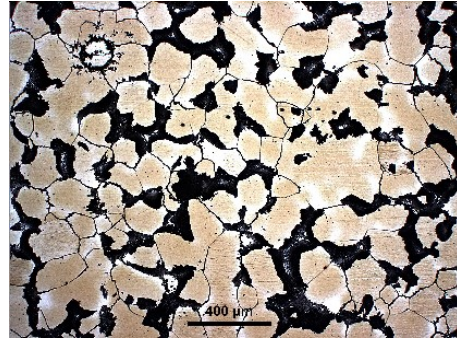**Figure 4.23. Microstructure of casting 7.**

Figure 4.24. Microstructure of casting 8.

4.1.3 Particle analysis

Figure 4.25-4.27 show images aquired with a backscatter detector in the EPMA. Note the different magnifications of the images. The numbers indicate positions for WDS analyses, and the results are given in Table 4.3, in atomic percent. The column to the right gives the names of well-known phases that fit reasonably well with the measured compositions. Particle 1 is assumed to be TiN from its rectangular shape, even though the analysis included much oxygen. The cerium-based particles found in the alloys added cerium were most likely CeO_2, $CeAlO_3$ or Ce_2O_2S.
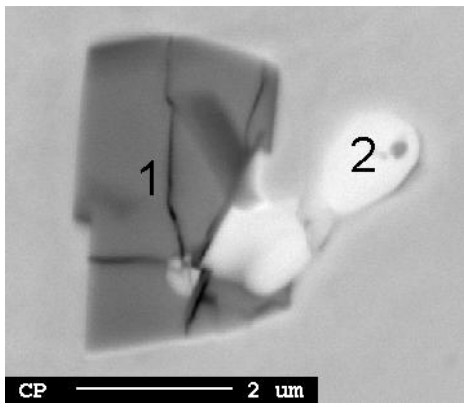

Figure 4.25. Particles of TiN (1) and CeAlO₃ (2) found in casting 3.

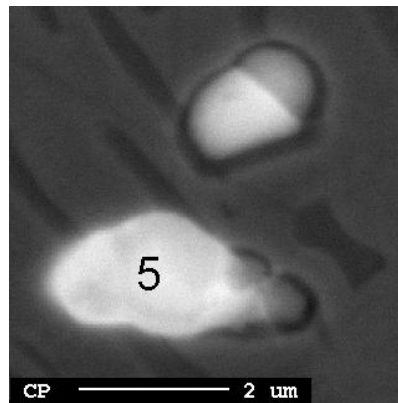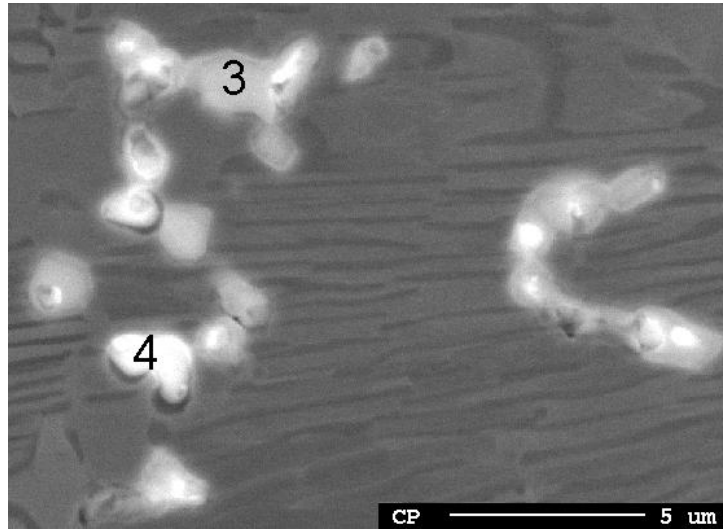**Figure 4.26. CeO₂ particle in casting 8.**

Figure 4.27. A cluster of particles in casting 4. The particle marked 3 is most likely CeAlO$_3$ and the one marked 4 is Ce$_2$O$_2$S.

Table 4.3. Chemical composition of particles in Figure 25, 26, and 27. Values are in atomic percent and normalized to 100%. (Minor elements are not included.)

No.	O	S	Al	N	Ti	Ce	Mn	Fe	Phase
1	15.4	0.017	1.43	29.8	50.2	0.527	0.629	2.02	TiN
2	36.0	0.013	6.76	0.0250	0.214	6.63	5.42	45.0	CeAlO$_3$
3	60.0	0.0020	17.8	0.124	0.309	18.3	0.736	3.11	CeAlO$_3$
4	31.2	12.5	0.089	0.480	0.00	26.7	4.35	24.7	Ce$_2$O$_2$S
5	53.6	0.230	0.059	1.19	0.00	32.2	2.32	10.4	CeO$_2$

Table 4.4 shows the result of additional WDS-analyses of an arbitrary selection of particles found in the six castings added cerium. The particles were recognized from their chemical composition. All the particles found in casting 3 were of the CeAlO$_3$ type. In casting 4 and 6 there were a predominance of CeO$_2$ particles, but a fraction of CeAlO$_3$ and Ce$_2$O$_2$S was also found. Most particles in casting 5 and all particles in casting 8 were of the CeO$_2$ type. Casting 7 had a slight predominance of CeAlO$_3$, in addition to Ce$_2$O$_2$S

and CeAlO$_3$. The mean particle size was between 1.0 and 1.8 μm. There seemed not to be any difference in size between the different types of particles.

Table 4.4. The percentage and type of detected oxides, number of particles analyzed in the EPMA and mean particle size of these particles.

Casting	Phase			Number of particles analyzed	Mean particle size
	CeO2	CeAlO3	Ce2O2S		
3	-	100 %	-	10	1.0 μm
4	50 %	20 %	30 %	10	1.3 μm
5	90 %	-	10 %	20	1.6 μm
6	60 %	20 %	20 %	10	1.8 μm
7	20 %	45 %	35 %	20	1.2 μm
8	100 %	-	-	20	1.6 μm

4.1.4 Cooling rate measurement

The fall in temperature during casting was measured in an additional experiment that was performed without any addition of grain refiner. Thermocouples were mounted in the centre of the mould, halfway to the surface and near the surface. The casting temperature was approximately 1385 °C, and the results obtained during the experiment are given in Figure 4.28. Apart from the fact that a lower maximum temperature was recorded near the surface than in the interior, it is seen that the cooling rate was very constant throughout the casting.
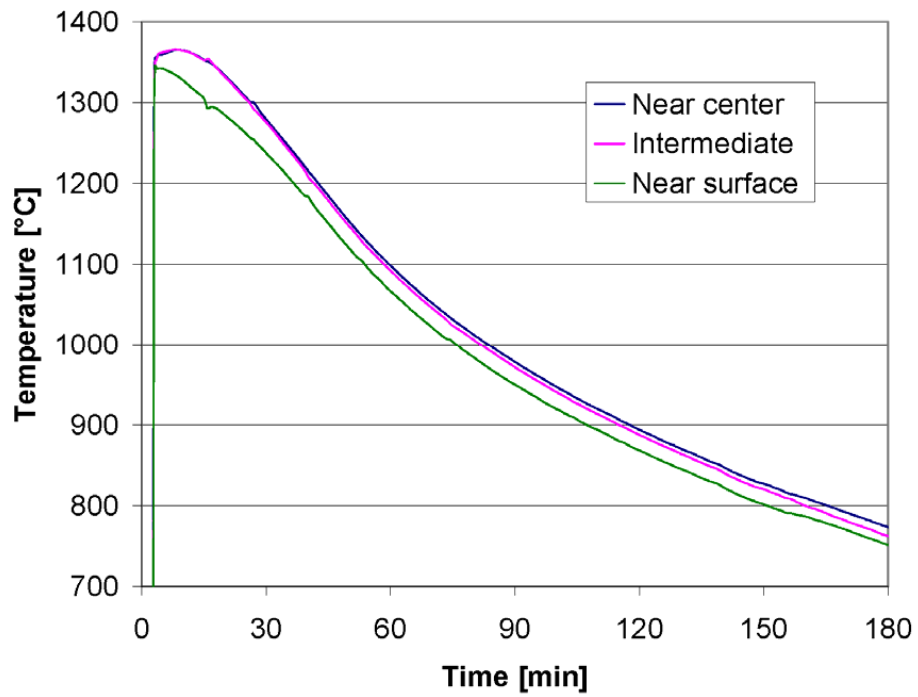
Figure 4.28. Typical temperature evolution during sand casting in the present experimental work on grain refinement.

4.2 Addition of carbide forming elements to Strømhard

4.2.1 Chemical composition

Chemical compositions measured with Optical Emission Spectrograph (OES) are given in Table 4.5. The contents of silicon, manganese, sulphur, phosphorus, chromium, molybdenum and titanium were similar for the different castings. The aluminum content was a little higher in alloy 1 than in the others. Alloy 1 had a little higher carbon content than expected, except from this its composition corresponded to the standard Strømhard alloy. Alloy 2 contained the target carbon content, and a vanadium content of 1 %. Alloy 3 contained 1.88 % carbon even thought only 0.20 % carbon was added in excess to the standard composition of Strømhard. It also contained 1 % vanadium. Alloy 4 had a carbon content of 1.79 % and a vanadium content of 2 %. No extra addition of carbon was made to this alloy. The unexpected high contents of carbon in alloy 1, 3 and 4 most likely came from contaminations from the graphite lid, used as a hot topping.

Table 4.5. Chemical composition measured with Optical Emission Spectrograph. Values are in weight percent.

Alloy	Additions	C	Si	Mn	S	P	Cr	V	Mo	Al	Ti
1	-	1.47	0.50	19.4	0.003	0.05	2.4	0.05	0.18	0.11	0.14
2	1% V	1.43	0.52	19.5	0.002	0.04	2.5	1.01	0.18	0.07	0.13
3	1% V, 0.2% C	1.88	0.53	19.4	0.003	0.04	2.5	1.04	0.18	0.06	0.14
4	2% V	1.79	0.50	19.1	0.003	0.05	2.5	2.16	0.17	0.06	0.15

4.2.2 Microstructure

The microstructure after austenitizing of Strømhard with its standard composition, alloy 1, is given in Figure 4.29 and 4.30. The bulk phase is austenite, and there are a few carbides within the grains and along grain boundaries. Dendritic microsegregation is visible from the etching. Cubic particles, most likely cubic titanium nitrides, in the size of a few micrometers were often observed, as seen to the left in Figure 4.30.
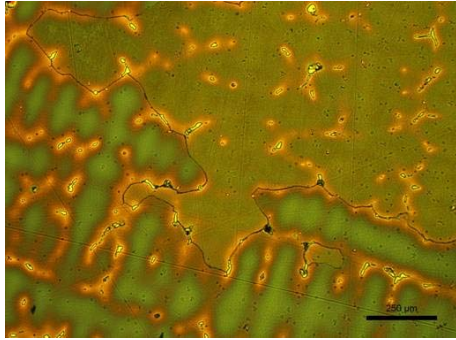
Figure 4.29. Alloy 1 represent standard Strømhard alloy. The microstructure is mainly austenitic with a few undissolved carbides. (Scale bar is 250 µm.)
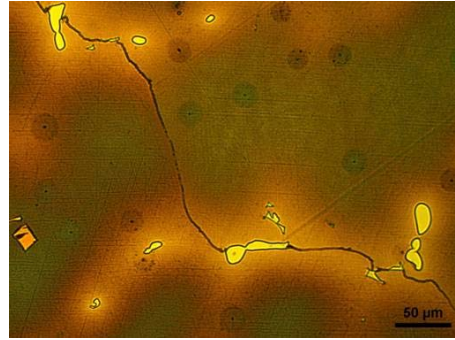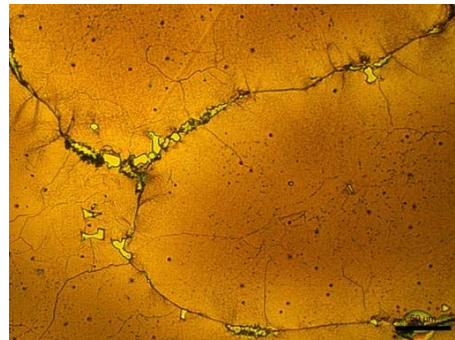

Figure 4.30. Grain boundary in alloy 1 with undissolved carbides. Two titanium nitrides are located to the left. (Scale bar is 50 µm.)

The microstructures of alloy 2, 3 and 4 after austenitizing at 1180 °C are shown in Figure 4.31, 4.33 and 4.35, and at a higher magnification in Figure 4.32, 4.34 and 4.36. There are increasing amounts of carbides both at grain boundaries and within the grains compared to in the alloys not added vanadium. Particularly alloy 4 had a large fraction of small particles within the grains. The carbide size was around 1 micrometer, and carbides were not present close to grain boundaries.
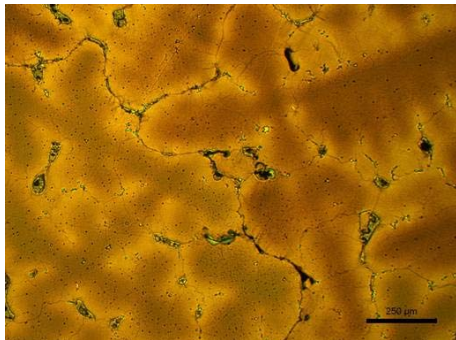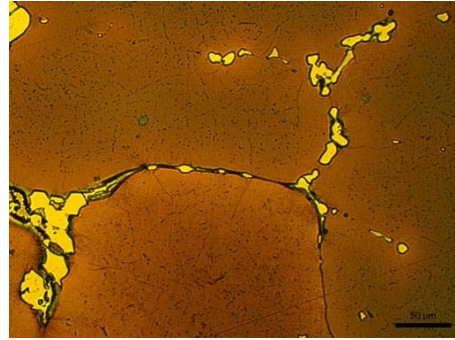

**Figure 4.31. Alloy 2 had an austenitic structure with undissolved carbides. (Scale bar is 250 µm.)**

Figure 4.32. A grain boundary in alloy 2 showing undissolved carbides. (Scale bar is 50 µm.)
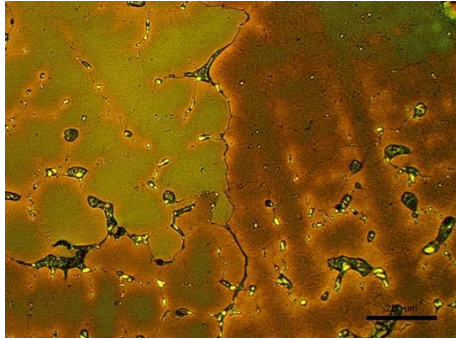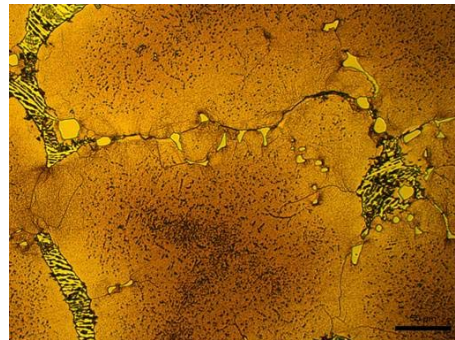
Figure 4.33. Alloy 3 containing undissolved carbides in an austenitic microstructure. (Scale bar is 250 μm.)

Figure 4.34. Undissolved carbides at a grain boundary in alloy 3. (Scale bar is 50 μm.)
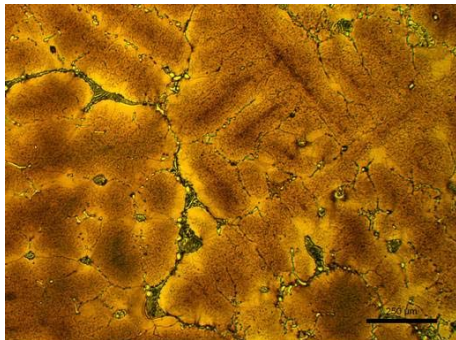
Figure 4.35. Alloy 4 contained both undissolved carbides along grain boundaries as well as evenly distributed smaller carbides within the grains. (Scale bar is 250 μm.)

Figure 4.36. Undissolved carbides at a grain boundary in alloy 4. Smaller carbides within the grains are visible as dark dots. (Scale bar is 50 μm.)

After aging at 500 °C for 8 hours there was almost no change in the microstructures of the vanadium added alloys. After 24 hours at this temperature, there was a small increase in the amount of grain boundary carbides in alloy 2. In alloy 3, precipitation of a needle shaped phase had occured within the grains. This particles, most certainly carbides (Section 4.2.3), was 20-50 μm long and 1-2 μm thick. These particles are visible in Figure 4.37. Alloy 4 had developed a small fraction of a grey microstructure constituent. This constituent was a very fine pearlite-like structure, with plates of carbide between ferrite. The presence of ferrite was confirmed by a magnet for all three alloys aged at 500

°C and 600 °C, and by an XRD analysis performed on alloy 4 (Section 4.2.3). After 200 hours, all three alloys had a large volume fraction of these fine pearlite-like constituents, see Figure 4.38 that is a micrograph from alloy 2 annealed for 200 hours at 500 °C. The higher magnification SEM backscatter electron image in Figure 4.39 shows a pearlite-like colony in alloy 3, aged at 500 °C for 200 hours. The plate structure is visible at several locations. Due to etching, the backscatter contrast in this image is opposite to what is normally abtained between carbide and ferrite, the former being light, and the latter being dark since it has been etched away.
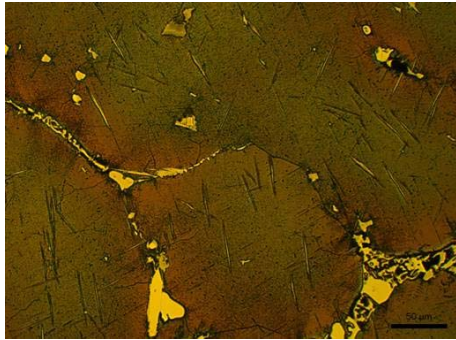
Figure 4.37. Alloy 3 after aging at 500 °C for 24 hours. The microstructure contains grain boundary carbides and needle shaped carbides within the grains. (Scale bar is 50 µm.)
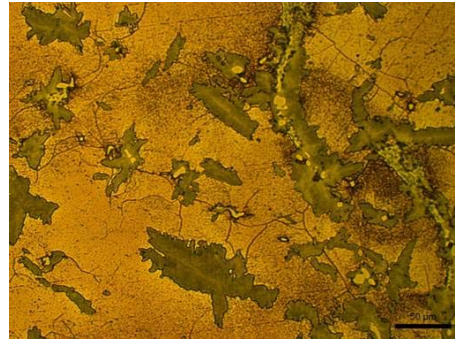
Figure 4.38. Alloy 2 after aging at 500 °C for 200 hours. The microstructure contains a pearlite-like constituent, gray in color in the image. (Scale bar is 50 µm.)
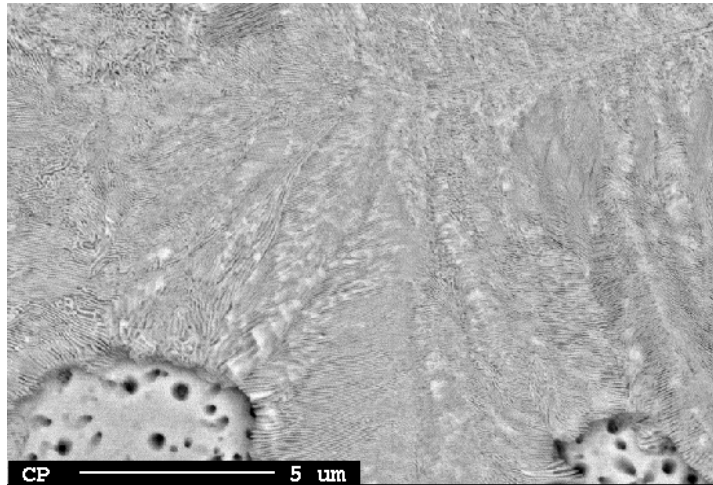
Figure 4.39. BSD-image of a fine peralite-like structure formed in alloy 3 after aging at 500 °C for 200 h. Within the lamellar colony, the carbide phase is light and the ferrite is dark.

After aging at 600 °C, pearlite-like colonies were present in all three alloys and after all aging times. One example is seen to the left in Figure 4.40. The pearlite structure in alloy 2 after aging at 600 °C for 200 hours is shown at high magnification in Figure 4.44. Aging at 700 °C gave a structure with carbides on the grain boundaries and in interdendritic zones, and a pearlite-like structure growing out from this. As the samples aged at 700 °C, 800 °C and 900 °C were not magnetic, the structure consists most likely of plates of carbides between austenite. The carbides in interdendritic zones are visible in Figure 4.41. Alloy 3 had also needle shaped particles within the grain after this treatment both after 8 and 24 hours. Grain boundary carbides and needle shaped particles in alloy 3 after 8 hours are shown in Figure 4.42. Figure 4.43 show grain boundary carbides and the lamella-like structure (similar to pearlite) of carbides and austenite in alloy 4 after 8 hours. The lamella-like structure composed of carbide and austenite is shown at high magnification in Figure 4.45. This image was taken with a BS-detector from alloy 3 after aging at 700 °C for 200 hours. Again, the ferrite appears dark in the image, and the carbide appears light.
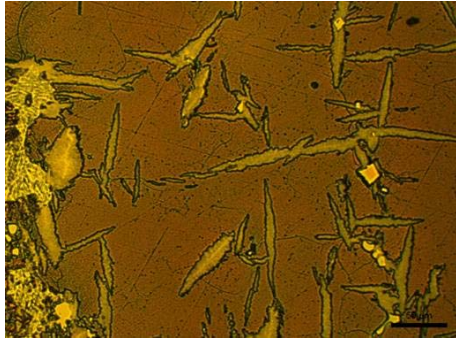
Figure 4.40. Alloy 2 after aging at 600 °C for 24 hours. The gray constituent is a pearlite-like phase. (Scale bar is 50 µm.)
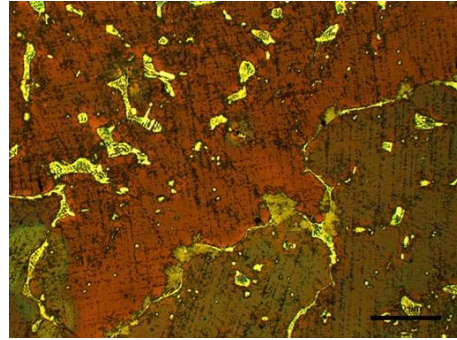
Figure 4.41. Alloy 3 after aging at 700 °C for 8 hours. The precipitated carbides seem to be located at interdendritic zones, as well as on the grain boundary. (Scale bar is 250 µm.)
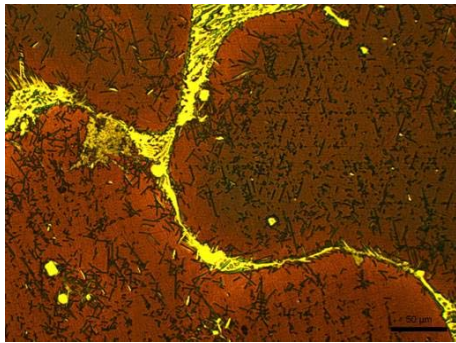
Figure 4.42. Alloy 3 after aging at 700 °C for 8 hours. The microstructure contains continuous grain boundary carbides (yellow in color) and needle-shaped carbides within the grains. (Scale bar is 50 µm.)
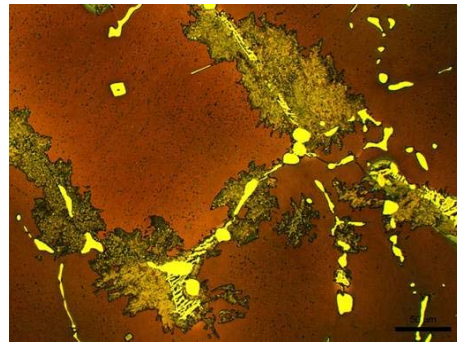
Figure 4.43. Alloy 4 after aging at 700 °C for 8 hours. A lamella like structure grow out from the grain boundary carbides (yellow I color). (Scale bar is 50 µm.)
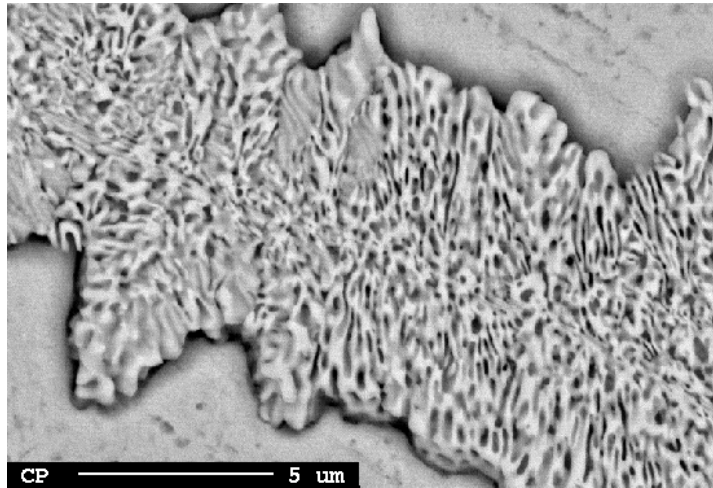
Figure 4.44. BSD-image of alloy 2 after aging at 600 °C for 200 hours. This is equivalent to the pearlitic-like structure present to the left in Figure 4.40.
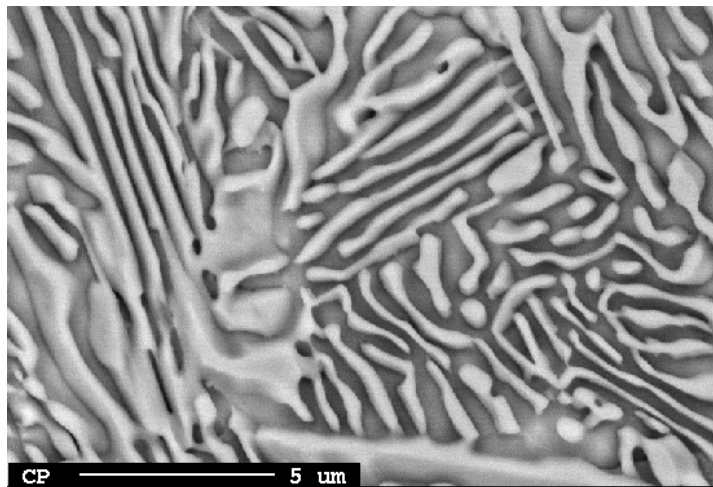
Figure 4.45. BSD-image of alloy 3 after aging at 700 °C for 200 hours. A course lamella/pearlite-like structure containing austenite (dark) and carbide (light).

After aging for 8 hours at 800 °C there was little precipitation in alloy 2, except for a continuous phase on the grain boundary. There was also a lamella like structure growing from the grain boundaries, Figure 4.46. In alloy 3 and 4 there was pronounced precipitation of grain boundary carbides and lamellar colonies that had grown out from these carbides, as shown in Figure 4.47. The lamellar structure is imaged at a higher

magnification in Figure 4.48 which was recorded from alloy 4 after only 8 hours at 800 °C. After 24 hours at 800 °C, lamellar colonies were present in all alloys. Aging at 900 °C gave similar microstructures as those obtained at 800 °C, but the lamellar microstructure was coarser. Figure 4.49 shows alloy 3 after 8 hours at 900 °C. Aging at 950 °C for 8 hours gave similar microstructures as aging at 900 °C.
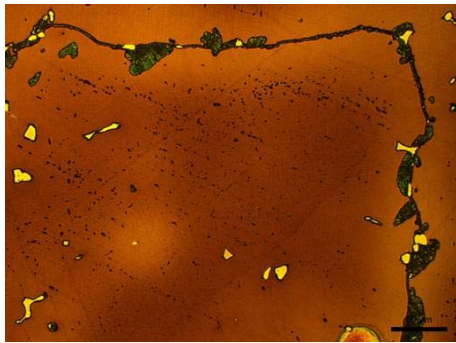
Figure 4.46. Alloy 2 after aging at 800 °C for 8 hours. A grain boundary is shown at right and top, covered by a precipitated constituent. (Scale bar is 50 μm.)
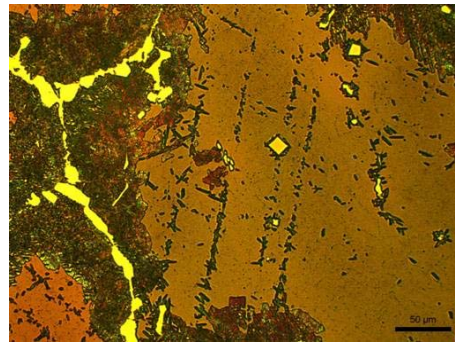
Figure 4.47. Alloy 3 after aging at 800 °C for 8 hours. A structure of lamella colonies is growing out of the grain boundary carbides (in yellow). (Scale bar is 50 μm.)
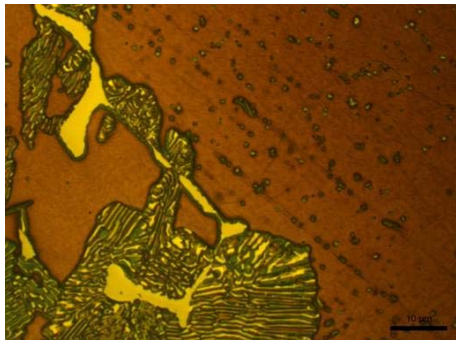
Figure 4.48. Alloy 4 after aging at 800 °C for 8 hours. The lamella structure at higher magnification. Small carbides also visible on the right. (See Figure 4.60). (Scale bar is 10 μm.)
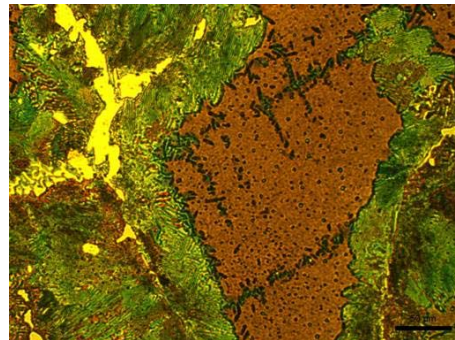
Figure 4.49. Alloy 3 after aging at 900 °C for 8 hours. A lamella structure is covering coarser carbides (in yellow). (Scale bar is 50 μm.)

After aging at 950 °C for 200 hours, a microstructure of austenite with finely dispersed particles appeared in the three alloys. There were still carbides on the grain boundaries, but these did not form a continuous belt as they did after aging at the lower temperatures. This type of microstructure is shown in Figure 4.50, and at higher magnification in Figure 4.51. The particles are visible both as globular and needle-shaped, but the possibility exist that all the particles are needle-shaped, but that the ones appearing round are needles that are oriented with an angle to the specimen surface. The round particles are 1-3 μm in diameter, and the needle-shaped particles are approximately 1 μm wide and 10-30 μm long. These particles are visible at an even higher magnification in the EPMA electron backscatter image of Figure 4.52, acquired from alloy 2 (etched sample). Figure 4.53 show the same structure in alloy 4 at an even higher magnification (not etched sample), and the small carbides found in the grain after austenitization are still present here (Figure 4.36). Some of these particles are cross shaped, indicating a growth relation to the matrix.
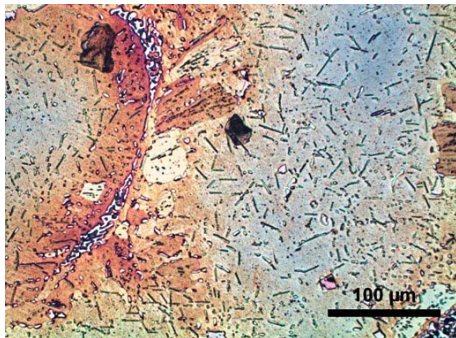
Figure 4.50. Alloy 2 after aging at 950 °C for 200 hours. The microstructure consists of precipitated carbides within the grain and non-continuous carbides on the grain boundary in the left of the image.
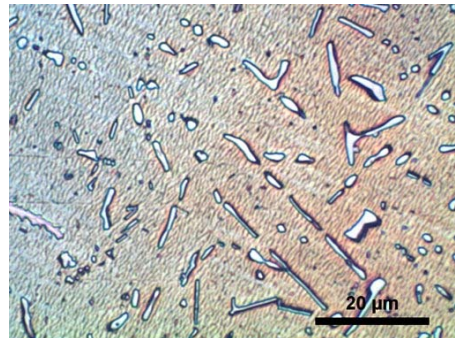
Figure 4.51. Alloy 2 after aging at 950 °C for 200 hours. Image of the carbides precipitated within the grain.
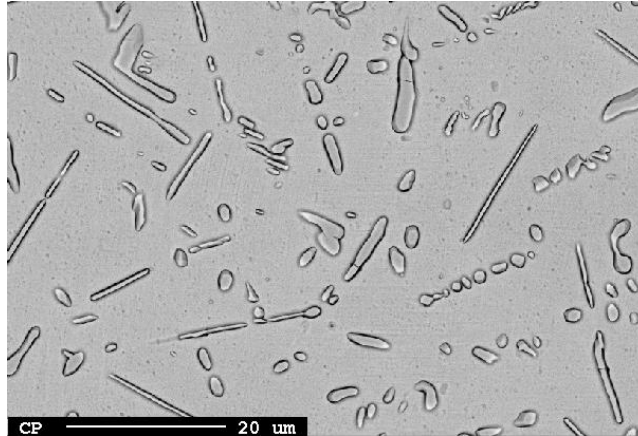
Figure 4.52. BS image of alloy 2 after aging at 950 °C for 200 hour, showing precipitated particles.
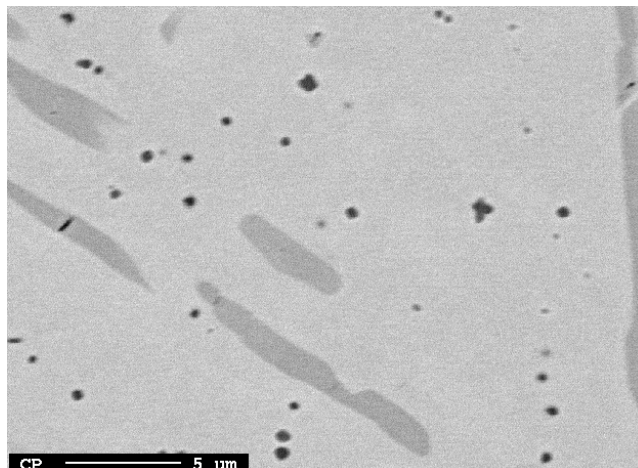
Figure 4.53. BS image of alloy 4 after aging at 950 °C for 200 hour, showing cross-shaped particles, present also after austenitizing, in addition to the precipitated needle-shaped and globular particles.

4.2.3 Particle identification

EPMA

Table 4.6 contains point analyses acquired with EPMA of precipitated particles in alloy 4 aged at 950 °C for 200 hours, both within the grains and on grain boundaries. These

particles are equivalent to those seen in Figure 4.50, 4.51 and 4.52. The grain boundary carbides have approximately the same composition as the intergranular carbides. The carbides are complex, containing vanadium, chromium, manganese and possibly iron. As the particles are in the same range of size as the resolution of the analysis volume in the EPMA, the compositional values may include contributions from the steel matrix. Especially, this concerns the values for iron and manganese that are the richest elements of the matrix.

Table 4.6. Chemical composition of precipitated carbides in alloy 2, 3 and 4 aged for 200 hours at 950 °C. Values are in atomic percent and normalized to 100%. (Minor elements are not included.)

Alloy	Phase	C	V	Cr	Fe	Mn
2	Carbide	20.3	6.2	15.3	32.9	24.7
3	Carbide	21.1	5.4	12.4	36.8	23.7
3	GB-carbide	19.6	8.4	13.5	32.9	24.9
4	Carbide	19.6	6.6	13.9	33.2	26.0
4	GB-carbide	20.2	6.7	12.9	34.3	25.4

The carbon content of the steel matrix (between the carbides) was measured by WDS in alloy 2 after aging at 950 °C for 200 hours and in alloy 4 after aging at 950 °C for 8 hours and 200 hours, applying a sample from the recast Strømhard alloy (Table 4.5, Figure 4.29) as a standard specimen. The results of these measurements are given in Table 4.7, and they show that the matrix is depleted on carbon after the aging. The depletion increased with increasing aging time.

Table 4.7. WDS analysis of carbon content in austenitic matrix. Values are in weight percent.

Sample	C
Alloy 2 950 °C 200 h	1.19
Alloy 4 950 °C 8 h	1.27
Alloy 4 950 °C 200 h	1.11

TEM

A TEM diffraction pattern is shown in Figure 4.54 and 4.55. The sample is alloy 4 austenitized and subsequently aged at 800 °C for 200 hours to achieve over-aged particles that ease their detection in TEM. The strong austenite diffraction spots are indexed according to a 111 type zone axis pattern. Weak precipitate spots are surrounding 000 and the 220 type matrix spots. Those precipitate spots that are located on the inside of the 220 matrix spots in the direction of 000, can be indexed according to the cubic unit cell of VC, having a NaCl crystal structure with lattice parameter 0.41599 nm [25]. The other weak precipitate spots surrounding 000 and the matrix spots can easily be explained by double diffraction.

Figure 4.56 and 4.57 are darkfield images formed by the precipitate diffraction spot on the inside of the matrix spot $0\bar{2}2$. The images show a high number of small globular particles being about 10 nm in diameter and a few larger particles of diameter 50-100 nm.
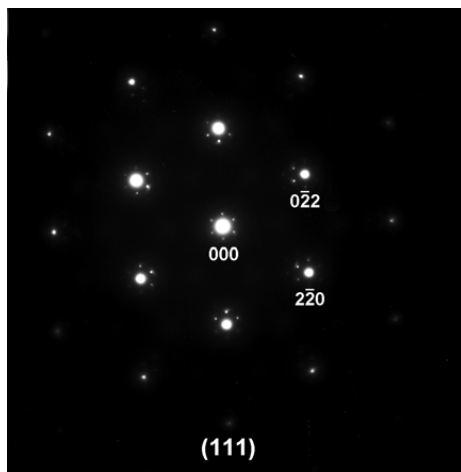
Figure 4.54. Diffraction pattern of the (111)-zone axis in austenite.
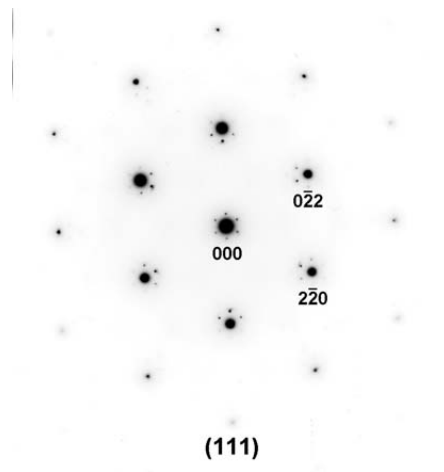
Figure 4.55. The diffraction pattern in Figure 4.54 inverted to display the week precipitate spots better.
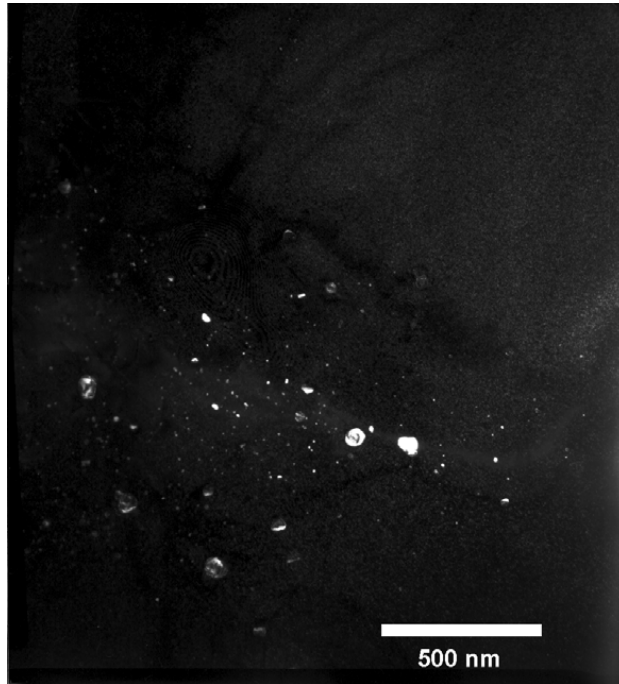
Figure 4.56. Dark field image of particles precipitated in alloy 4 after aging at 800 °C for 200 hours. The largest particles are approximately 60 nm in diameter.
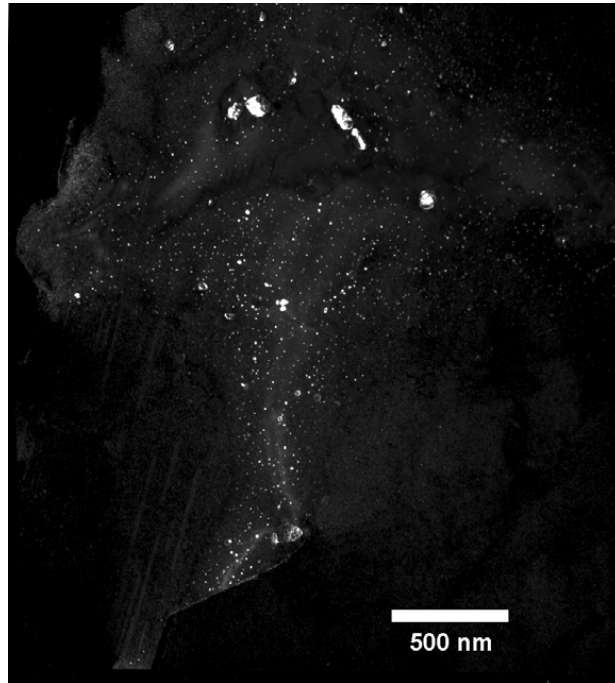
Figure 4.57. Dark field image of particles precipitated in alloy 4 after aging at 800 °C for 200 hours. The largest particles are approximately 100 nm, and the smaller visible particles are around 10 nm.

Figure 4.58 and 4.59 show a diffraction pattern from the about 300 nm large particle shown in the center of the bright field image of Figure 4.60 (same alloy and aging condition as above). In this pattern, the particle reflections are generally stronger than the matrix reflections, some of the latter are indexed. As in the diffraction pattern of Figures 4.54-55, precipitate reflection spots are located on the inside of matrix reflections, and also these spots can be indexed according to well-known NaCl-type vanadium carbide unit cell, although the lattice parameter seems to be 1-2 % larger for the particle in Figure 4.60 than for the small particles in Figures 4.56-4.57. In addition to the strong particle reflection spots, weaker spots are halving the reciprocal distance in the $1\bar{1}\bar{1}$ matrix direction. The particle has thus a superlattice crystal structure, and to further complicate the structure, superlattice streaking can be observed in the $1\bar{1}\bar{1}$ matrix direction. These superlattice diffraction effects have earlier been reported for V_6C_5 that has a monoclinic superstructure of lattice parameters a = 0.509 nm, b = 1.018 nm, c = 0.882 nm, and with

65

an angle between the a- and c-axes of 109.5°. [26] In Figures 4.58-4.59, a strong orientation relationship is seen to exist between the carbide and the austenite steel matrix. There were also found similar particles which display the same carbide diffraction pattern as seen in Figures 4.58-4.59, but the orientation relationship between matrix and carbide has been lost.
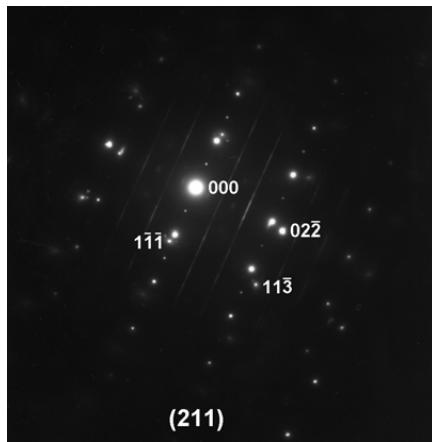
Figure 4.58. Diffraction pattern from the particle seen in Figure 4.60. The matrix reflections are indexed according to an austenite 211 zone axis.
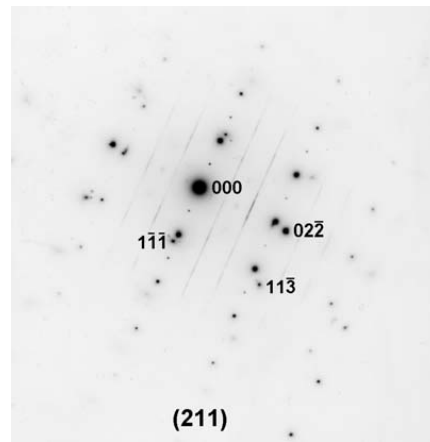
Figure 4.59. The diffraction pattern in Figure 4.58 inverted to display the week precipitate spots better.
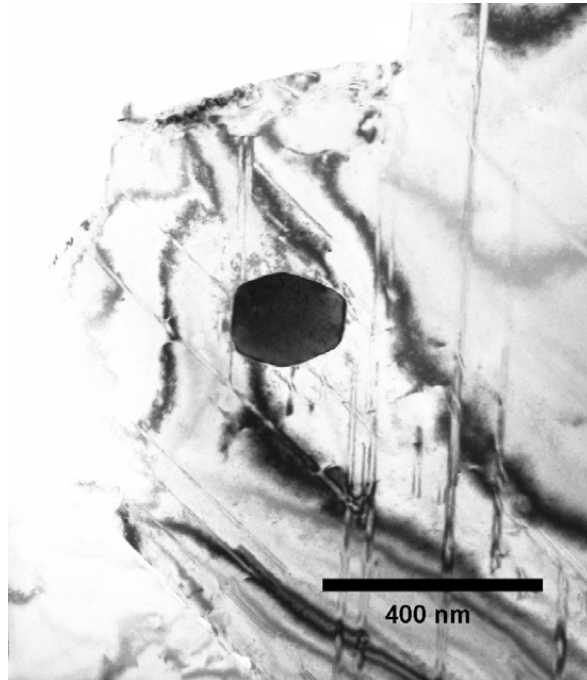
Figure 4.60. Bright field image of particle in alloy 4 after aging at 800 °C for 200 hours, assumed to be similar to the small particles within the grains of Figure 4.36 and Figure 4.53.

Compositional EDS analyses of selected particles were performed in a FEG transmission electron microscope. Figure 4.61 shows a bright field image of 10 nm large particles in alloy 4, aged for 200 hours at 800°C, with an accompanying EDS spectrum from the particle located in the center of the image. As these particles are very small, they will only make up a small fraction of the thickness of the sample. The spectrum therefore contains strong contributions from the surrounding steel matrix, which is responsible for the high iron and manganese peaks. The relatively strong vanadium peak confirms the presence of vanadium in the small precipitates.
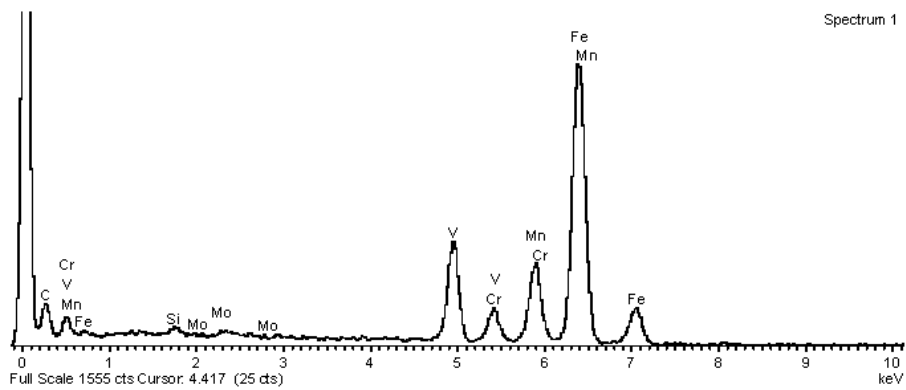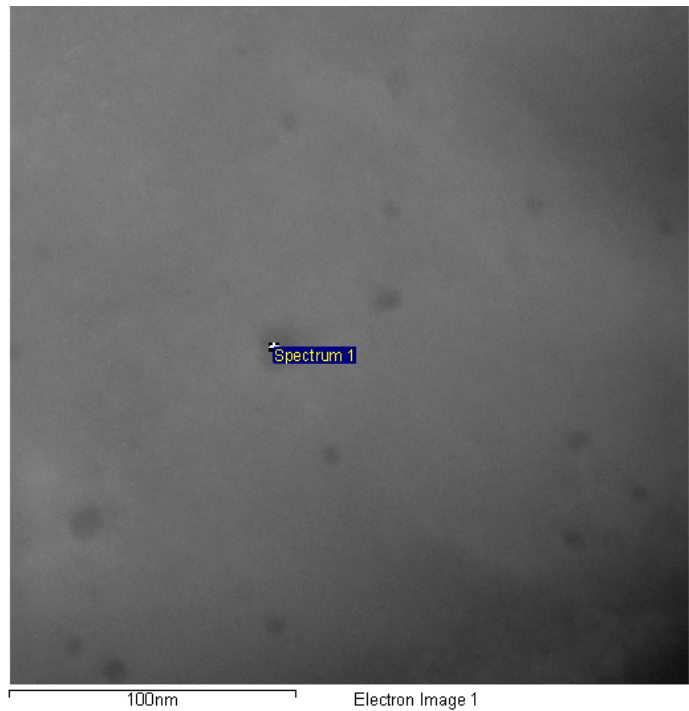
Figure 4.61. A bright field image of 10 nm small particles precipitated in alloy 4 during 200 hours aging at 800 °C, with an accompanying EDS-spectrum.

Figure 4.62 shows a bright field image of some larger particles in the same sample, with an accompanying spectrum from the particle located in the lower part of the image. The high peak for vanadium confirms that also this particle is vanadium carbide. The particles

in Figure 4.62 are similar to the particle in Figure 4.60, and are also believed to be identical to the small particles that are seen within the grains in the light optic micrograph of Figure 4.36 and 4.53.
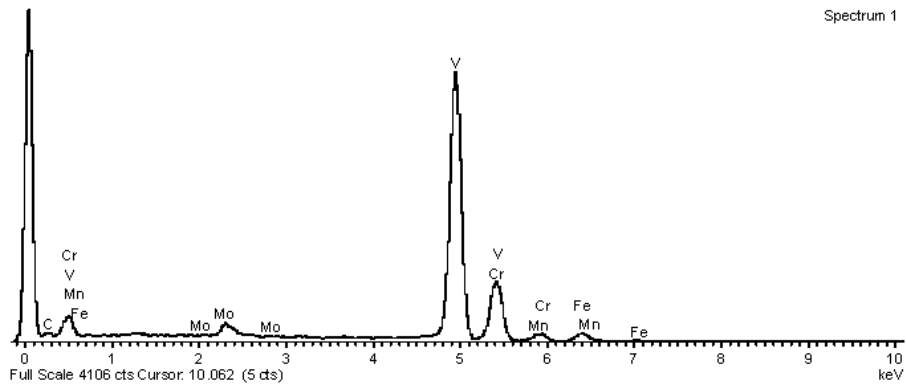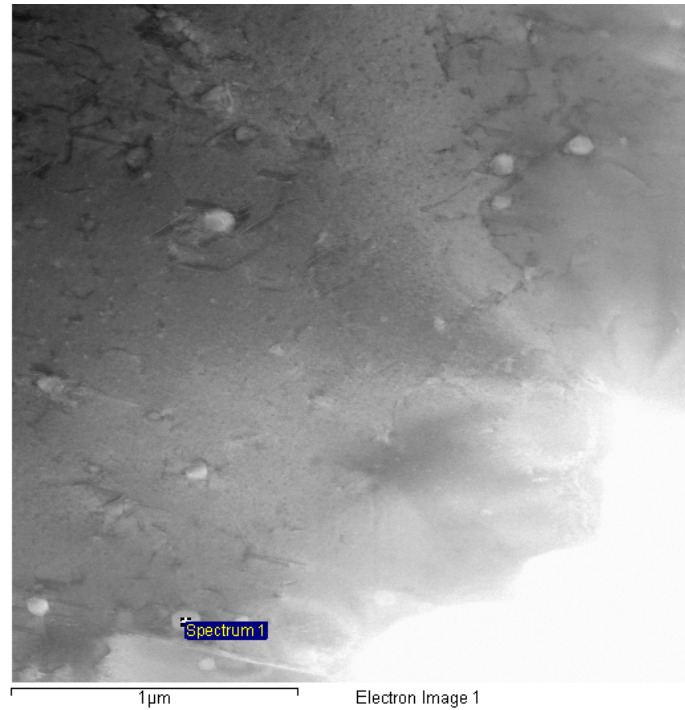
Figure 4.62. A bright field image of particles similar to the 300 nm large particle in Figure 4.60, with an accompanying TEM EDS-spectrum.

XRD

X-ray diffraction was performed on selected specimens to identify phases of high enough volume fraction to be detectable by this technique (in the order of 1 mass %). The spectrum in Figure 4.63 was acquired from the original Strømhard alloy, recast at Elkem Bjølvefossen during the grain refining experiments and with no subsequent heat tratment. Three strong austenite peaks are present in the spectrum in addition to a very faint extra peak that is interpreted as M_3C. Its position deviates slightly from the exact position of Fe_3C, so it is assumed that the cementite phase contains some manganese and chromium in addition to iron. The M_3C peak is most probably associated with the lamellar constituent that is decorating the grain boundaries of Strømhard in the as-cast condition, see Figure 4.17. Figure 4.64 shows the XRD spectrum obtained from alloy 4 annealed at 500 °C for 200 hours. This spectrum confirms the presence of ferrite in this aging condition. In addition, an unambiguous identification of vanadium carbide is being made. Corresponding vanadium carbide peaks are present in the spectrum of Figure. 4.65, recorded from alloy 4 after aging at 950 °C for 200 hours. In this spectrum, additional peaks from a M_7C_3 phase are present.
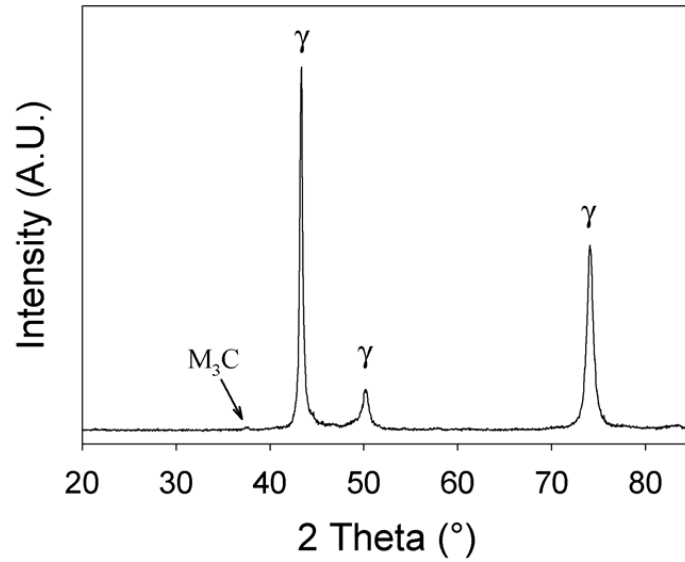
Figure 4.63. Spectrum aquired at the XRD for a Strømhard alloy in the as-cast condition. The peaks verifies an austenitic structure with a small fraction of M₃C.
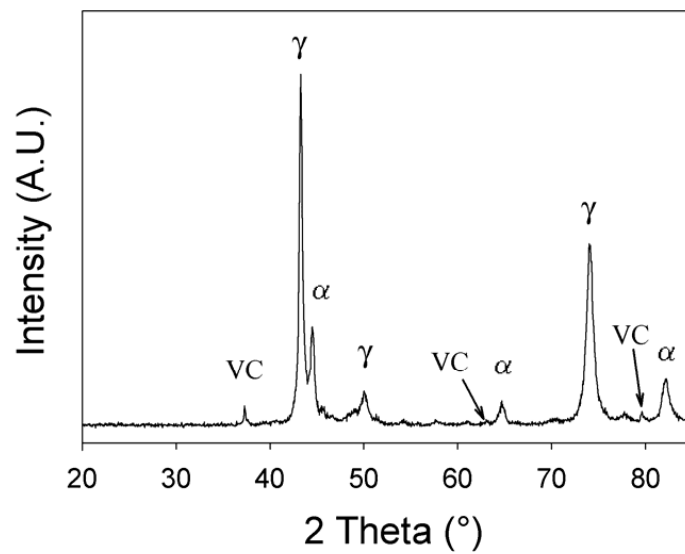
Figure 4.64. Spectrum aquired at the XRD for alloy 4 after aging at 500 °C for 200 hours. The peaks verifies an austenitic structure with a small fraction of ferrite and VC.
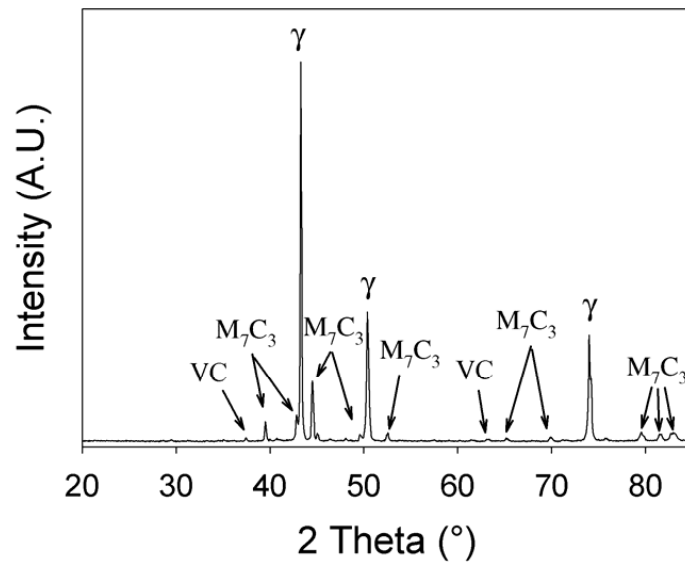
Figure 4.65. Spectrum aquired at the XRD for alloy 4 after aging at 950 °C for 200 hours. The peaks verifies an austenitic structure with a small fraction of M_7C_3 and VC.

4.2.4 Hardness measurements

The hardness values of the alloys after austenitizing and aging are shown in Figure 4.66, 4.67, 4.68 and 4.69. The hardness measurements were taken between the carbide particles that were visible in the light microscope, i.e. corresponding to those seen within the grains in Figure 4.51. The hardness of alloy 1 (recast Strømhard without vanadium additions) is marked with a single red square, and is in the figures referred to as "Reference". The standard deviation varies considerably between the samples, from 5 HV units to 44 HV units, but the mean standard deviation was approximately 16 HV units. All three alloys showed a hardness increase after aging in the temperature range 500 °C - 900 °C, either after 8 hours or after 24 hours. Alloy 3 has an inexplicable drop in hardness after aging at 600 °C for 24 hours. Upon aging at 950 °C, Figure 4.69, alloys 2 and 4 experienced slight decreases in hardness after 8 hours and a marked increase in hardness after 200 hours. For alloy 3, no essential hardness change was measured upon aging at 950 °C.
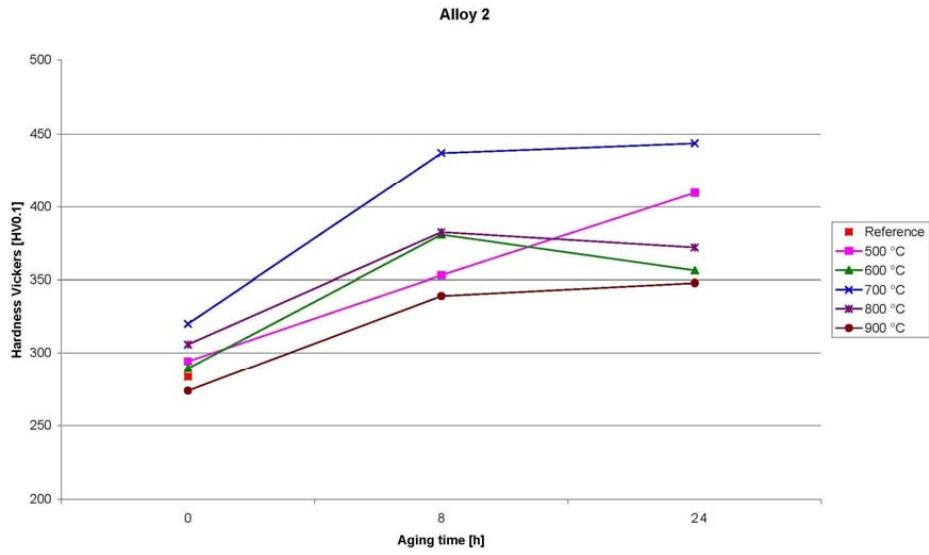
Figure 4.66. Hardness values of alloy 2 after austenitizing and aging for 8 and 24 hours.
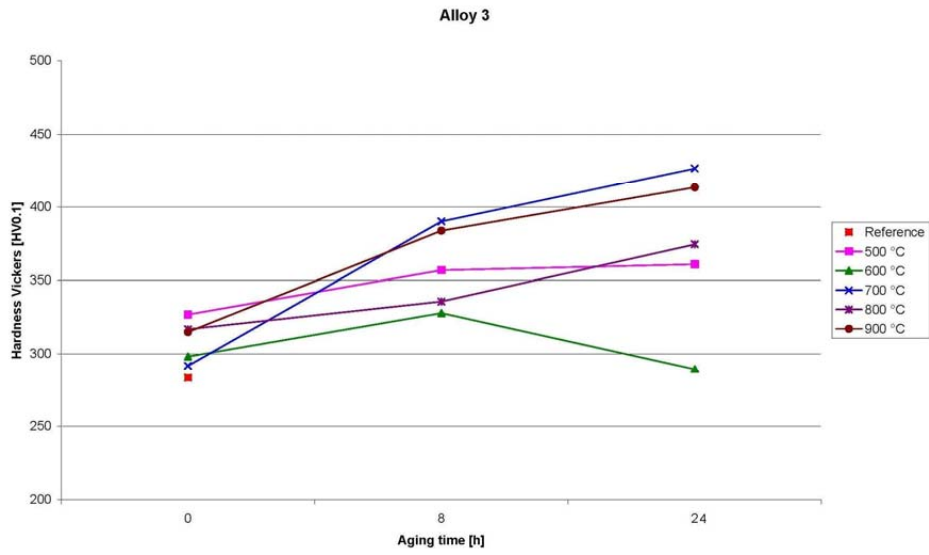
Figure 4.67. Hardness values of alloy 3 after austenitizing and aging for 8 and 24 hours.

73
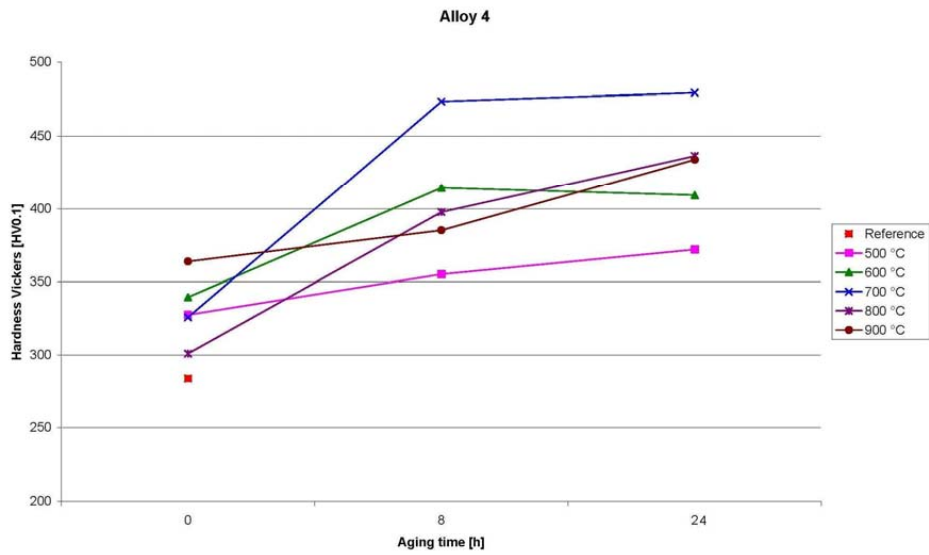
Figure 4.68. Hardness values of alloy 4 after austenitizing and aging for 8 and 24 hours.
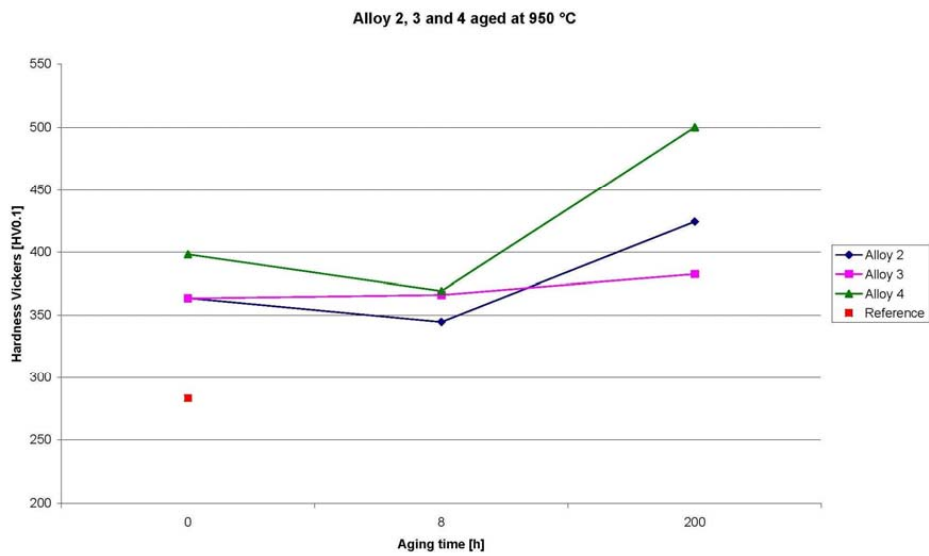
Figure 4.69. Hardness values of alloy 2, 3 and 4 after austenitizing and aging 950 °C for 8 and 200 hours. (The time axis is different from Figures 4.62-4.64.)

4.2.5 Abrasive wear testing

The results from the abrasive wear test after austenitization and aging at temperatures between 500 °C and 900 °C are shown in Figure 4.70. The weight loss of alloy 1 (the original Strømhard alloy) is indicated with single red squares, marked "Reference". The two most obvious trends that can be read from the figure are that, (i) the wear resistance increases with increasing amount of alloying elements (in the order alloy 2-3-4), and that, (ii) the wear resistance decreases with increasing aging temperature. For the lowest aging temperature, there is an increase in wear resistance with aging time. For the aging temperature 600 °C the effect of aging is minor, and for higher aging temperatures, the wear resistance decreases with increasing aging time.

Due to the apparent promising microstructures obtained after aging at 950 °C (Figures 4.50-4.52), an additional series of wear tests were conducted on specimens aged for 8 and 200 hours at this temperature. In this test series, the weight loss of the various test specimens was not measured after the austenitizing treatment. Instead, the average weight loss of the five other as-austenitized specimens of each alloy was taken as the as-austenitized weight loss. Due to the limitation of only six samples in the wear test apparatus, alloy 3 aged for 8 hours was omitted from the tests. The obtained weight loss values are plotted in Figure 4.71, but, unfortunately, it is seen that the results fall in line with the trend from Figure 4.70. The negative effect of the aging is, however, not as strong as after aging at 900 °C. The improved wear resistance with increased alloy contents is maintained for the aging temperature of 950 °C, at least partly.
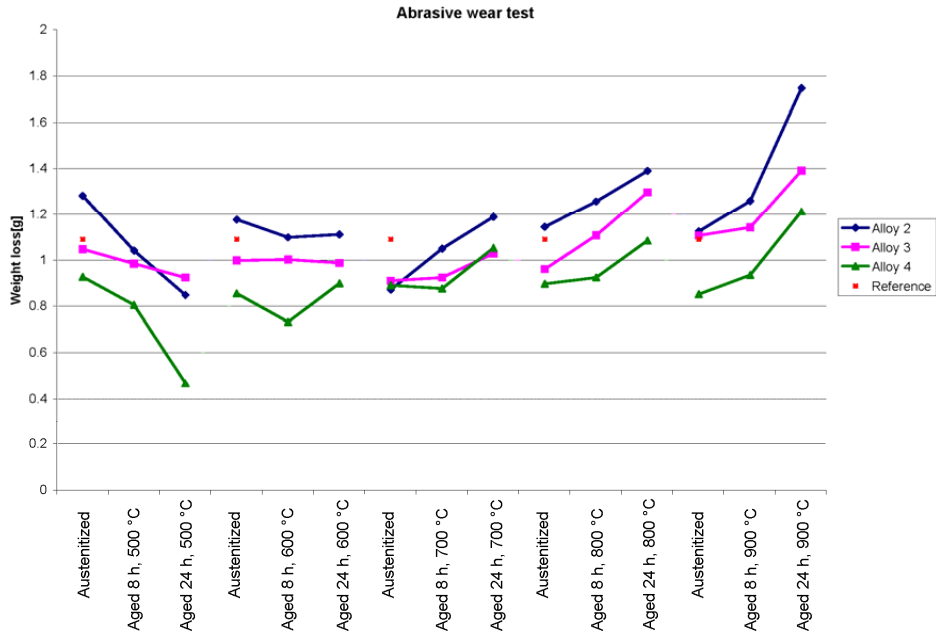
Figure 4.70. Weight loss for the different alloys and heat treatments from the abrasive wear test.
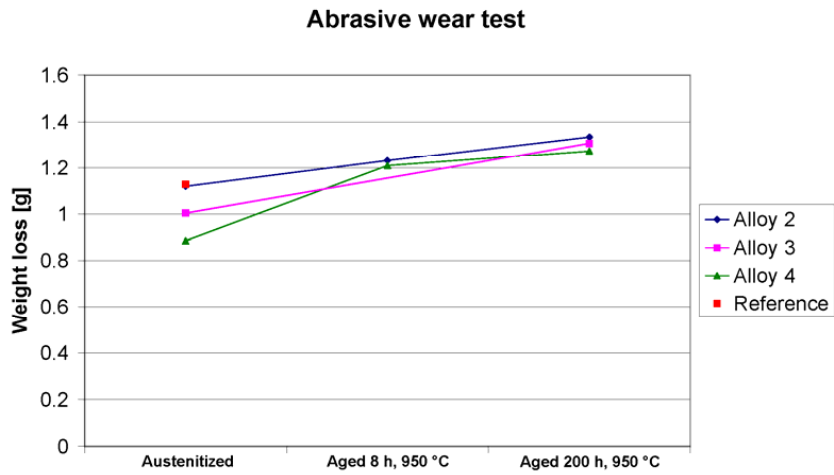
Figure 4.71. Weight loss for the different alloys after austenitization, and after aging at 950 °C for 8 and 200 hours.

Wear surfaces from austenitized alloy 1 (Strømhard), alloy 4 aged at 950 °C for 8 and 200 hours, and alloy 2 aged at 950 °C for 200 hours were analyzed in the EPMA to reveal the dominating wear mechanism, see Figures 4.72-4.74 from alloy 1 and 4. For all three alloys it was clear that the main abrasive wear mechanism is ploughing, creating furrows in random directions due to the rotational movement of both specimen and abrasive paper. The furrows were generally wider and deeper in alloy 1 than in alloy 4. Occasionally, craters from crushed and removed particles were observed within or adjacent to the furrows. These craters appeared in a higher number in the V-containing alloys than in the reference Strømhard alloy that did not contain vanadium. In the former alloys, the craters were usually associated with course vanadium containing carbides on grain boundaries or within the grains, e.g. craters A, B, and C in Figure 4.73. In the electron backscatter image of Figure 4.74 (CP=ComPosite) it is seen that these craters coincide with a medium dark phase, which from the WDS element maps of carbon (C) and vanadium (V) (Figure 4.74) is seen to be a vanadium containing carbide phase, corresponding to the carbide particles identified in Table 4.6. EDS spot analyses performed from the inside of the craters confirmed the presence of vanadium. In the wear surface of the reference alloy, the craters were far lower in number, and by EDS analysis titanium was detected inside the craters, probably in the form of brittle TiN particles. Ti-containing craters were also rarely observed in the wear surface of the V-containing alloys. No crater associated with alloy carbides was detected in the wear surface of alloy 1. There was no obvious difference between the two wear surfaces of alloy 4 annealed for 8 hours and for 200 hours at 950 °C, although the former contained a high amount of lamellar cells around the grain boundaries. Apparently, the lamellar cells seem therefore to have no negative effect on the wear mechanism. A carbon line profile was recorded from one of the outer edges of the polished surface to its centre by WDS in the EPMA in alloy 3 aged for 200 hours at 950 °C to test the material for decarburization during the prolonged annealing at 950 °C, but no sign of decarburization was detected.
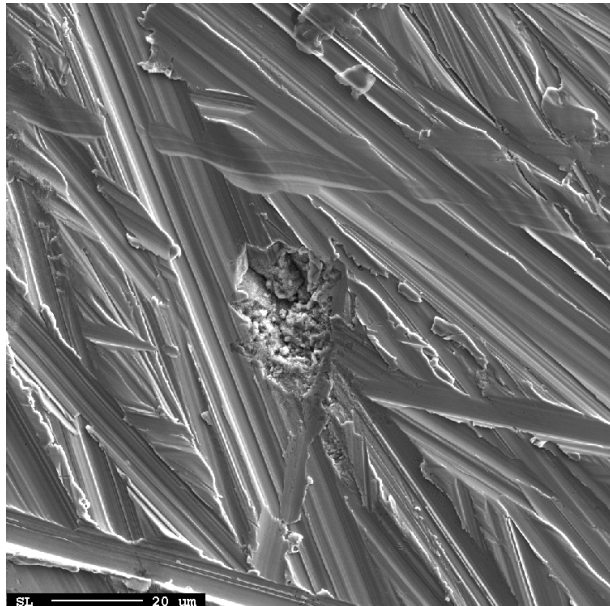
Figure 4.72. Secondary electron image of wear surface on Strømhard (alloy 1).
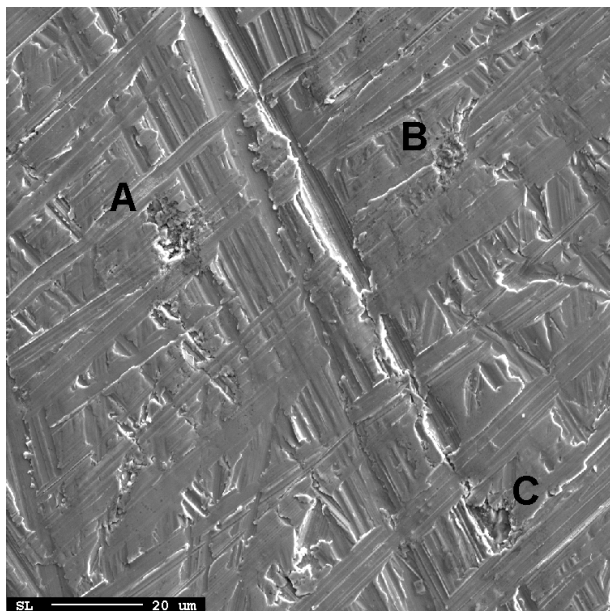
Figure 4.73. Secondary electron image of wear surface on alloy 4 after aging at 950 °C for 200 hours.
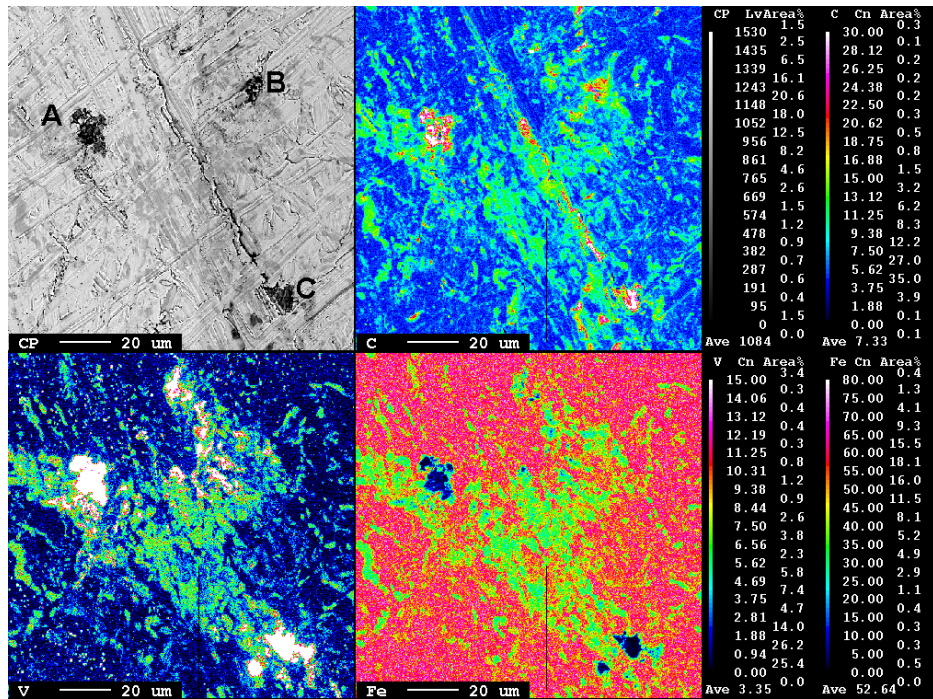
Figure 4.74. Electron backscatter image of alloy 4 after aging at 950 °C for 200 hours. The same are shown in Figure 4.73. The craters coincide with a medium dark phase, which from the WDS element maps of carbon and vanadium.

5   Discussion

5.1   Grain refinement of Strømhard steel

5.1.1 As-cast microstructures

The microstructure of the casts that were made during the grain refining experiments consisted of equiaxed grains with a eutectic constituent at the grain boundaries, Figures 4.17-4.24. The XRD spectrum in Figure 4.63 was recorded from casting 2, in the as-cast condition. A very weak peak from an M_3C carbide phase is present in the spectrum. This peak is corresponding to the cementite phase that is present at higher carbon contents and at high temperatures in the phase diagram of Figure 2.4 and the phase diagram of Figure 5.12, indicating that the eutectic at the grain boundaries of the as-cast alloys is the one that is present in the phase diagram of Figure 2.4 at about 16.5 at% carbon and 1100 °C and in the phase diagram of Figure 5.12 at about 4.3 % carbon and 1100 °C. The reason why the M_3C peak in the XRD spectrum is so low must be the large grain size of the alloy (about 0.5 mm, giving a small total carbide volume).

5.1.2 Cerium yield

Table 4.2 shows the measured contents of cerium in the experimental castings. The cerium yield varied between 30 and 52%, see Figure 5.1 where measured cerium content is plotted versus added cerium. Increased cerium additions leads to an increase in content of cerium in the solidified steel. Two lines corresponding to 40 % and 100 % yield are drawn in the figure, and it is seen that the experimental points are scattered around the 40 % yield line.
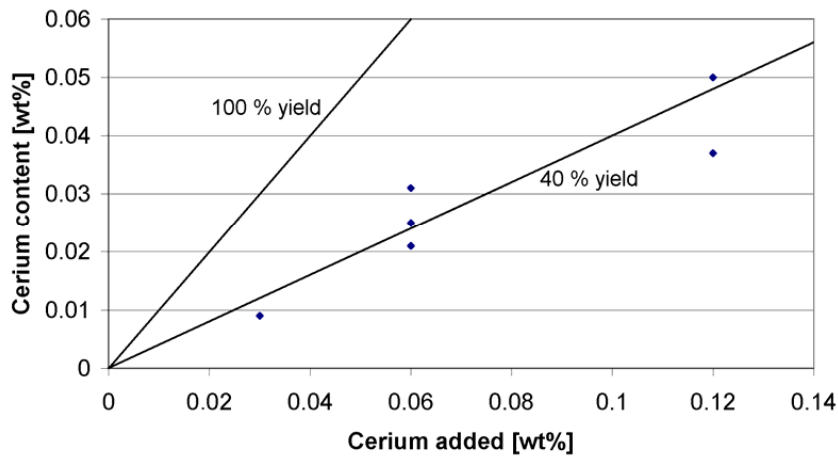
Figure 5.1. The weight percent cerium added plotted against the amounts of cerium measured in the steel castings

The cerium yield of a given casting is to some extent influenced by the addition done in the ladle during the previous casting, as there was an increase in yield when the addition in the previous casting was high, as for casting 6 that have the highest yield. This is probably caused by re-entrainment of cerium particles transferred to the ladle wall during the previous trial. Other mechanisms that can give differences in yield are given below, except for the difference in casting temperature, the circumstances should be fairly equal.

After addition and melting of EGR, cerium will quickly react with oxygen and sulfur and form particles, or react directly with the crucible wall or top slag. A portion of these free cerium particles formed can settle to the slag or the ladle walls. These effects will increase with stirring of the melt, higher surface-to-volume ratio of the melt, increasing contents of oxygen and sulfur in the melt, higher temperature of the melt when the cerium is added, and with longer time from addition of cerium until casting/solidification. Stirring and high surface-to-volume ratio will lead to increased settling of particles to the top slag and ladle walls. The three latter parameters will lead to coarsening and larger particles that again lead to increased settling. The addressed problem concerning the surface-to-volume ratio can be described by Figure 5.2 and the following deduction.

81
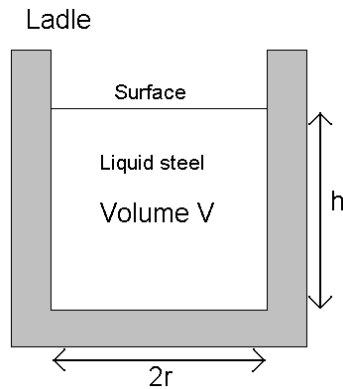
Figure 5.2. Schematic drawing of a ladle, were *r* is the internal radius of the ladle, *h* is height of the melt and *V* is the volume of the steel melt.

Consider a cylindrical ladle, furnace or crucible having an internal diameter *2r* and containing a steel melt that reaches *h* up from the bottom. The ladle walls and the top slag will probably react differently with the grain refining particles in the melt, but as a simplification it is assumed that the negative effects on particles here are the same. *h* will in most practical cases be of the same size as the diameter, so in this deduction *h* is set to be *2r*. By dividing the area by the volume the ratio between these two dimensions is found to be.

$$\frac{A}{V} \propto \frac{1}{r} \qquad (10)$$

Figure 5.3 shows how the ratio between the surface area and the volume of a melt is affected by its size given by the ladle radius. The surface/volume ratio will increase markedly if the radius of the ladle or crucible is reduced beneath approximately 10 cm. Because of the small dimensions involved in the laboratory scale experiments, any negative effect of the surface will have a crucial effect on the result. The surface effect will be less important in a larger pilot scale test like the one of the present work, and in an industrial scale, even a higher yield is attainable. From this assessment, a cerium yield of around 40 % that was obtained in the present work is an acceptable result. The yield is expected to be higher in an industrial scale, but the results from this test, with a ladle in the larger size of area marked "Pilot scale" in Figure 5.3, should not be far from what can be achieved in full scale production.
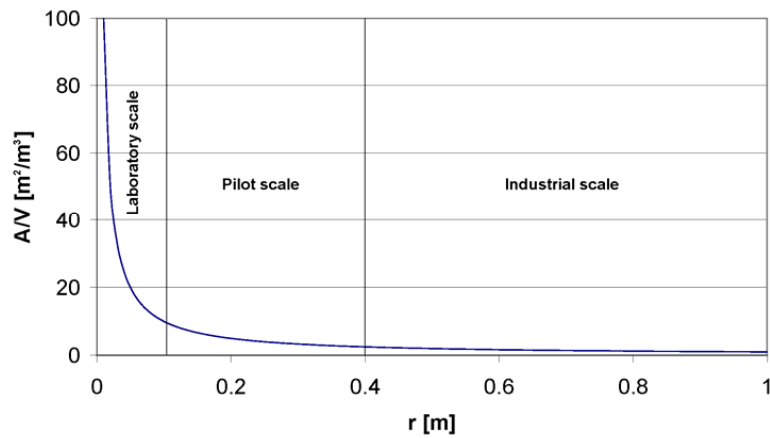
Figure 5.3. Surface area divided by volume as a function of the radius.

The only mixing of the melt in these experiments occurred by natural convection and by pouring the melt from the ladle to the sand mould. If gas is bubbled through the melt, flotation can occur. Flotation is the transportation of particles on bubbles to the top-slag. In industrial application of grain refiners in steels the use of gas purging may be omitted because of this mechanism, otherwise the substrate particles can be removed before any grain refinement is achieved. In the present experiments, aluminum and cerium were added simultaneously. The use of a deoxidizing agent together with a grain refiner, that also is expected to react with oxygen, should be reconsidered, as removal of too much oxygen will inhibit the formation of cerium oxides in the melt. The sequence, in which deoxidizer and grain refiner are added, might also have an effect.

5.1.3 The casting structure of Strømhard steel

The casting temperatures, grain sizes and lengths of the columnar zone are listed in Table 4.2. Casting 1 is omitted in this evaluation as its casting temperature was not measured. The casting temperatures have unfortunately a larger scatter than intended. This scatter will be the most significant uncertainty in the assessment of the grain refining experiments. The casting temperature is plotted against grain size in Figure 5.4. Although casting 8 which had the smallest grain size also had the lowest registered casting temperature, there is little coherence

between the casting temperature and the grain size. The small grain size in casting 8 is therefore probably an effect of another mechanism than just the low casting temperature.
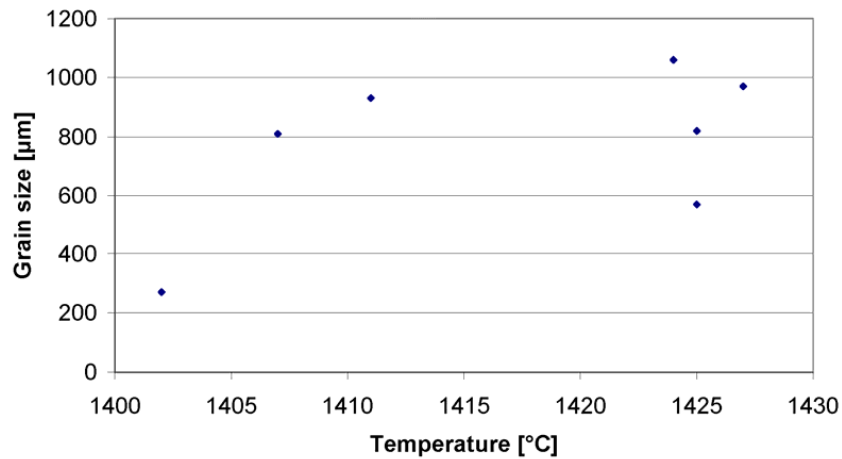
Figure 5.4. Casting temperature versus grain size.

The length of the columnar zone is plotted against the casting temperature in Figure 5.5. The shortest columnar zone was found in casting 8. There is no evident relation between these two parameters. Thus, the short columnar zone in casting 8 is probably also an effect of another parameter than the low casting temperature.
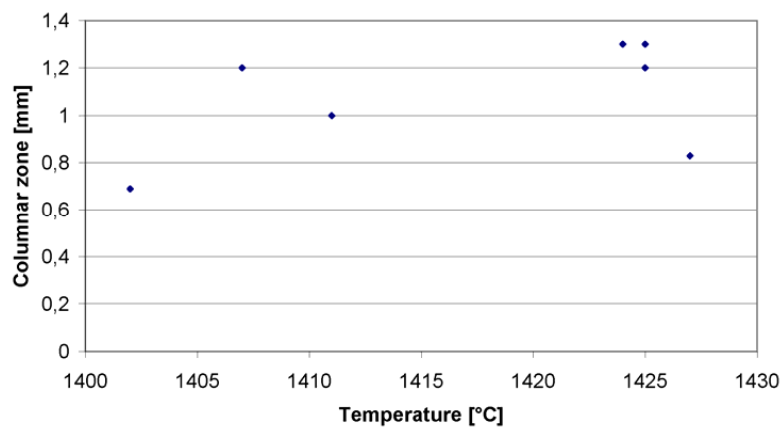
Figure 5.5. Casting temperature versus length of columnar zone.

The microstructures of the experimental castings can be divided into to main categories as shown in Figure 5.6. Castings 2-7 resemble case A, with large grains and a columnar zone of width 1.3 mm. Casting 8 resemble case B with a small mean grain size of 270 μm and with a columnar zone of half the width of the other castings.
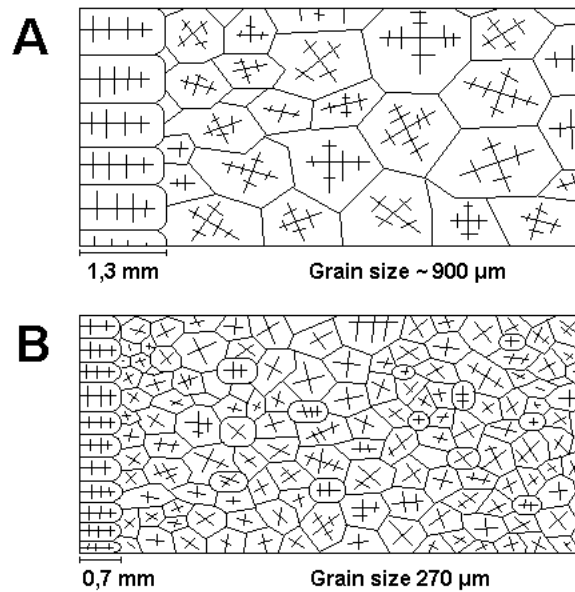
Figure 6. Schematic drawing of casting structures.

5.1.4 The connection between casting structure and cerium content

By comparing cerium content and grain size as is done in Figure 5.7, there seems to be a sudden drop in the grain size as the cerium content reaches a critical value. This can indicate that cerium is an effective grain refiner in this steel, but that a certain critical value of cerium content in the steel is required.
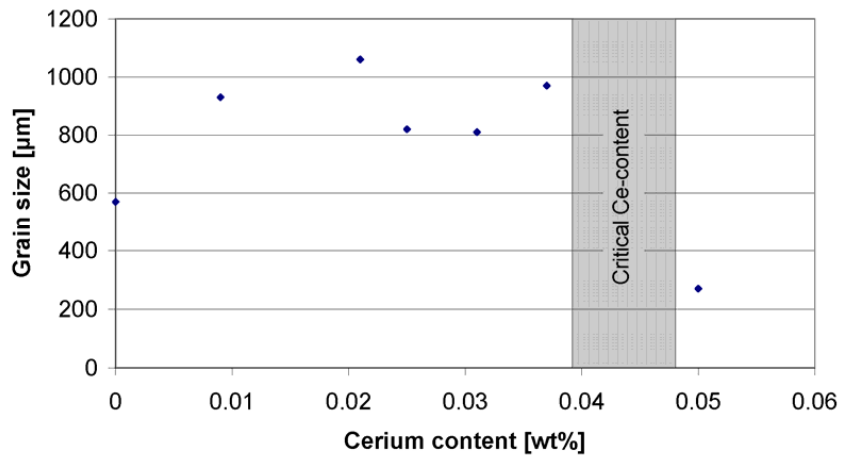
Figure 5.7. Cerium content versus grain size.

As is seen in Figure 5.8, the width of the columnar zone seems to be little influenced by the cerium content for low cerium levels, but it is reduced when the cerium content increases above approximately 0.035 %.
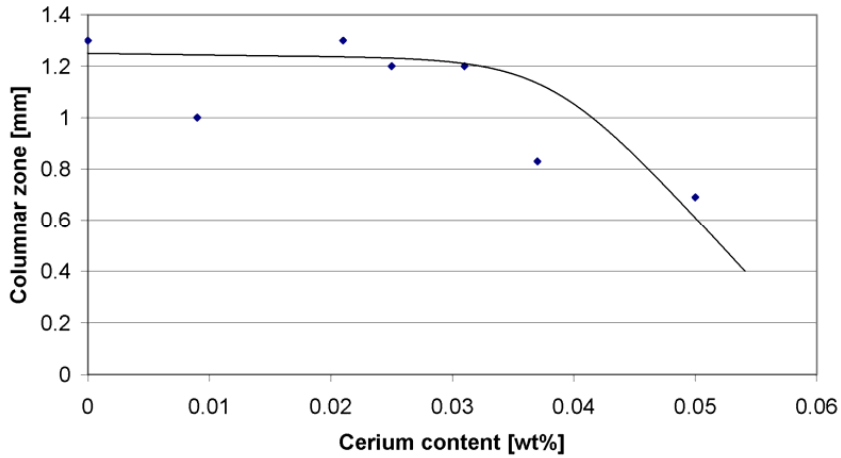
Figure 5.8. Cerium content versus length of columnar zone.

5.1.5 The effect of cerium containing particles on the cast structure

According to the theory of grain refinement, cerium based particles are nucleating equiaxed grains, giving a finer grain structure and a more narrow columnar zone. In Figures 5.9 and 5.10 the grain size and the width of the columnar zone are plotted against the number density of cerium particles. From a comparison with Figures 5.7 and 5.8, it is evident that the grain size and columnar width depend on the number density of cerium-based particles in the same way as they depend on the cerium content. To obtain a fine grain structure and shorten the width of the columnar zone, the number density of cerium particles in the steel has to be above a critical value.
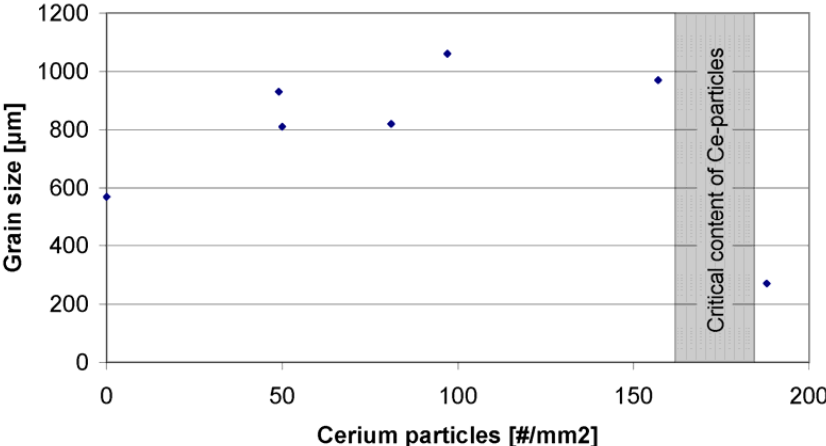
Figure 5.9. Number density of cerium particles versus grain size.
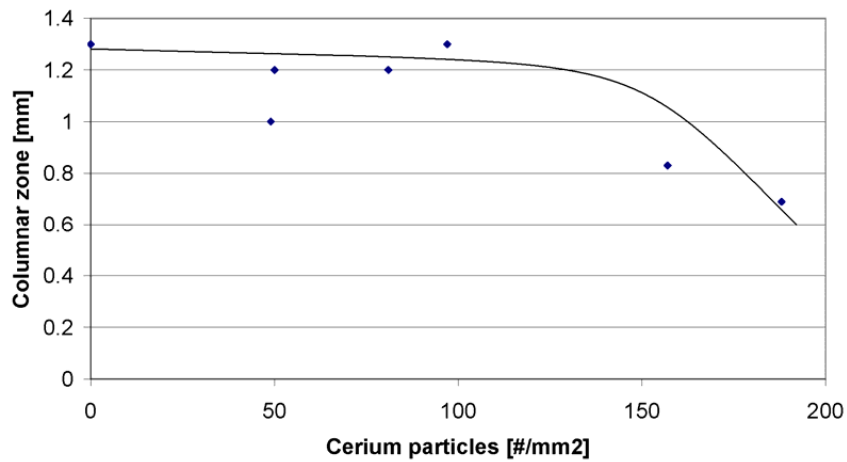
Figure 5.10. Number density of cerium particles versus length of columnar zone.

The number of cerium particles seems to be an almost linear function of the cerium content, as illustrated in Figure 5.11. The cerium content in the steel is again a result of the amount of cerium added, as shown in Figure 5.1. This relationship proves that higher additions of cerium give a larger number of particles, as long as the yield stays the same.
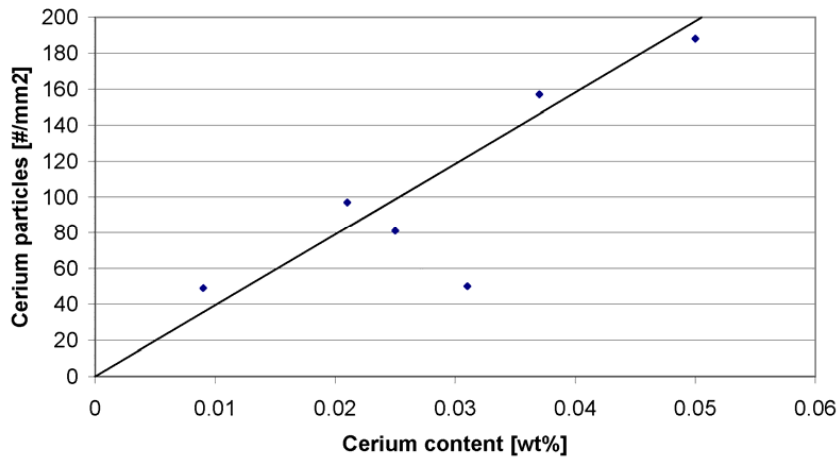
Figure 5.11. Cerium content versus number density of particles.

Different types of cerium-containing particles were found. These particles were concluded to be CeO_2, $CeAlO_3$ and Ce_2O_2S, as the atomic ratios measured with WDS in the EPMA matched these known cerium compounds fairly close. By looking at the added cerium and aluminum amounts, in Table 3.1, cerium obtained, in Table 4.2, and particles found in the

different castings, in Table 4.4, there seem to be an effect that small additions of cerium give $CeAlO_3$ inclusions. Even though no aluminum was added, the residue in the melt was enough to be incorporated in the cerium oxide phase. In the cases where moderate amounts cerium were added, in castings 4, 6 and 7, there are a mix of CeO_2, $CeAlO_3$ and Ce_2O_2S. Casting 7 was also added a relatively large amount of aluminum, but this only gave a slight predominance of $CeAlO_3$. The highest additions of cerium were applied to casting 5 and 8, in these castings almost all particles was CeO_2. Surprisingly, in alloy 8 that was added aluminum also, no $CeAlO_3$ was detected among the 20 analyzed particles. The reason for this correlation between amount of cerium added and type of inclusion precipitated is not understood, but it will be important if specific cerium compounds are required.

If the theoretical grain size is calculated, by assuming that all particles act as a nucleation point and are evenly distributed in the steel, the average grain size g for a two dimensional case is given by:

$$g = (\frac{1}{\sqrt{N}})$$

(11)

where N is number of particles per square millimetre. The theoretical grain size for the castings that were added cerium is, together with the obtained grain size, given in Table 5.1. It is seen that, for all alloys, there is a large difference between the theoretical and the real grain size. Only a few particles have therefore been active in the grain nucleation process. By replacing g in Equation 11 by the obtained grain size, the number of active particles per mm^2, $N_a = 1/g^2$, can be calculated, assuming that all grains have been nucleated by a cerium-based particle. The calculated N_a- values are given in Table 5.1. The table also gives the percentage of particles that have nucleated grains, i.e. the refiner efficiency.

Table 5.1. Summary of the experimental results obtained in the grain refining experiments.

Casting	Obtained grain size	Theoretical grain size	N, mm^{-1}	N_a, mm^{-1}	Refiner efficiency
3	930 μm	143 μm	49	1.2	2.4 %
4	820 μm	111 μm	81	1.5	1.9 %
5	970 μm	80 μm	157	1.1	0.7 %
6	810 μm	141 μm	50	1.5	3.0 %
7	1060 μm	102 μm	97	0.9	0.9 %
8	270 μm	74 μm	188	13.7	7.3 %

It is seen that the refiner efficiency varied a lot between the different castings, and that it generally is quite low. For alloy 8, which has the smallest grain size, the refiner efficiency is by far the highest. Compared to other alloy systems, the obtained yield values are not small, however. For instance, in a paper by Greer [27] on grain refinement of aluminium by means of TiB$_2$ particles, refiner efficiencies in the range 0.09% - 0.6 % are reported. The reason for low efficiency values is that most of the grain refining particles are too small to nucleate grains from the melt. Greer reports a minimum particle size in the order of 0.8-3 μm, depending on the type of grain refiner [27, 28]. For steels, the minimum particle size is assumed to be about 1 μm, see Section 2.8, without any specific proof of this. Table 4.4 shows that most of the cerium oxide particles in castings 3-8 are of a size that is equal to or larger than this assumed minimum size, and accordingly, they should have been more efficient than they proved to be. This could indicate that the critical size of cerium based grain refiners in austenitic manganese steels is somewhat larger that anticipated.

From Table 4.2 and 4.4 is difficult to draw any decisive conclusion regarding the efficiency of the different oxides as a grain refiner. Based on the mismatch to the austenite lattice at 1350 °C (Figure 2.13), where the solidification of Strømhard starts to occur, the approximate misfit is 3.2 % for CeAlO$_3$, and 4.8 % for CeO$_2$. CeAlO$_3$ is expected to be a better substrate for nucleating austenite than CeO$_2$ is. However, from types of particle found (Table 4.4) no such correlation between obtained grain size (Table 4.2) and type of grain refining particle can be deduced. For instance, a majority of CeO$_2$ particles were detected in both alloy 5 and alloy 8 which have, respectively, the lowest and highest refiner efficiency of all alloys. Neither is there any difference in the mean particle size that can explain the difference in refiner

efficiency between the two alloys. (Indeed, only 10 to 20 particles for each casting are included in the statistics for the data given in Table 4.4, but far more particles were observed during the work, and the impression was that there is no essential difference between the alloys with respect to size distribution of the cerium containing particles.)

The only parameter that could have influenced the refiner efficiency and the obtained grain sizes in the observed way is the casting temperature which varied slightly between the alloys. If refiner efficiency is plotted against casting temperature, as is done in Figure 5.12, one see that the refiner efficiency increases with decreasing casting temperature. Thus, the oxides are not active as grain refiners if the casting temperature is too high. A lower casting temperature will give a lower temperature gradient during solidification, this will in turn give a wider undercooled zone a head of the solidification front and increase the effect of the substrate particles as nucleation points.
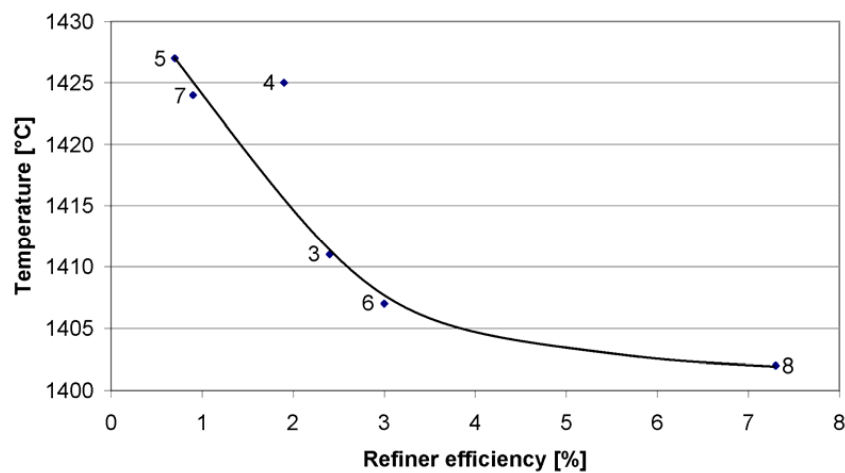
Figure 5.12. Refiner efficiency plotted against casting temperature. Each point is indicated with the appropriate casting number. Refiner efficiency increases with decreasing casting temperature.

The information in Figure 5.12 does not give any further indication to find a correlation between refiner efficiency and oxide type. This might indicate that the refiner efficiency of the two types of cerium oxides is relatively equal. A possible reason for this can be the relatively low mismatch of both oxides towards the austenite (4-6 %). Another reason could be that the surface energies of the oxides towards the melt and towards the austenite embryo are of greater importance for their nucleation ability than the lattice mismatch is. More work is needed to confirm any of these suggestions.

91

5.2 Effect of vanadium additions to Strømhard steel

5.2.1 Calculated phase diagram for Fe-20Mn-C

For obtaining a better understanding of the microstructures and phases that were formed in the various parts of this work, a pseudo binary phase diagram was calculated for a selected alloy composition. Since much of the work was focused on vanadium containing alloys, the diagram for one of these systems was chosen, i.e. Fe-19.5%Mn-2.5%Cr-1.0%V-C, see Figure 5.13. The diagram was calculated applying the ThermoCalc software package and the TCFE 3 database [29]. Since the chosen alloy system contains only a small amount of vanadium, it is also expected to have a certain applicability to the original Strømhard alloy that formed the basis for the grain refining experiments. (Section 5.1.1)
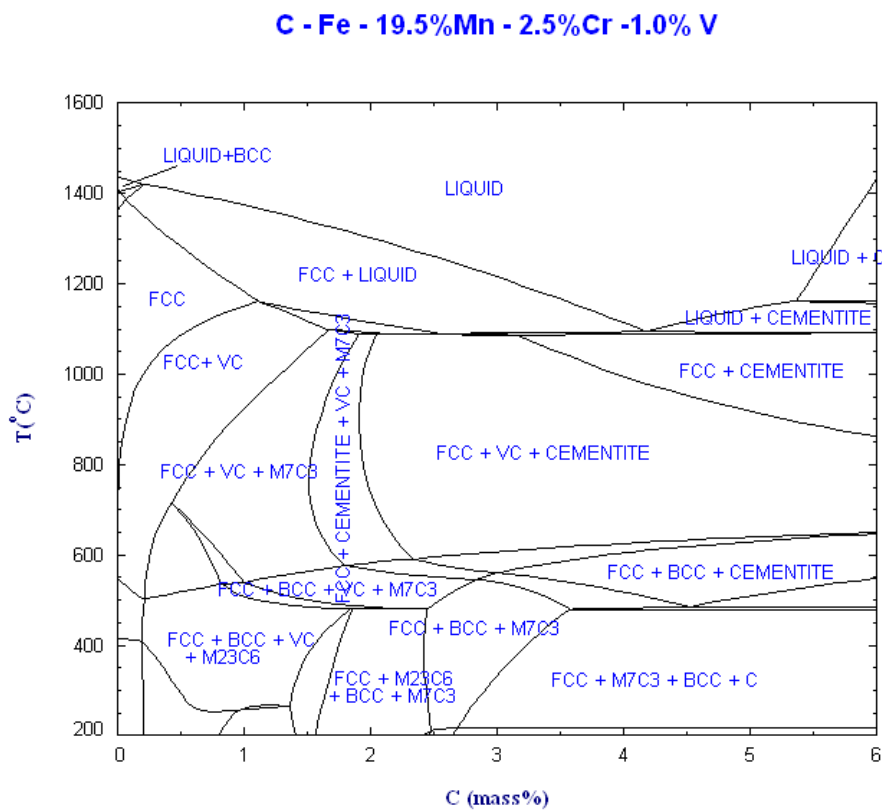
Figure 5.13. Phase diagram for Fe -19.5%Mn-2.5%Cr-1.0%V - C. [29]

5.2.2 Microstructure development in vanadium containing Strømhard steel

The chemical compositions of the alloys produced by vanadium additions are shown in Table 4.5. The higher carbon content in alloy 3 and 4 is most likely contamination from the graphite lid used as a hot topping. During the vacuum degassing, the steel melt has a tendency to "boil", causing the melt to splash so that it comes in contact with the graphite lid and knock lose particles that dissolve in the melt.

In the microstructure images of the steels modified with vanadium, shown in Figure 4.31-4.36, a higher fraction of undissolved carbides can be found that in the standard alloy 1 both on grain boundaries and within the grains, Figure 4.29-4.30. This is the case even though a higher austenitizing temperature was used for the vanadium containing alloys than for the standard alloy. The increased difficulty in removing carbides by heat treatment of the new alloys is a result of the higher amount of carbon and of the stronger affinity that carbon has to vanadium than to the other elements in the alloys. The austenitizing temperature of 1180 °C was not high enough to dissolve all the carbides formed during solidification. As this austenitizing temperature already is above the theoretical solidus temperature, a higher austenitizing temperature is not realistic as this could lead to local melting. The coarse eutectic carbide that still is present at some of the grain boundaries in the images, e.g. in Fig. 4.36, is expected to be of the type M_3C, c.f. the phase diagram in Figure 5.13 (cementite). This cementite is assumed to contain some vanadium. (M_3C is not present in the XRD spectra of the vanadium modified alloys, Figure 4.64-4.65, but this can be due to the large grain size that gives a low total volume of M_3C after austenitization.) Other phenomena, such as grain growth, decarburization and scale forming, would be additional problems associated with a higher austenitizing temperature, especially in an industrial context. The volume fraction of carbides increases with the addition of either carbon, vanadium or both. The amount of undissolved vanadium carbides in these alloys was expected to increase the wear resistance, but also to reduce the toughness of the alloys. The small particles present within the grain of alloy 4 were expected to have a positive effect on the abrasive wear resistance, without giving too much loss in toughness. As these particles are fairly evenly distributed within the grain, as opposed to on grain boundaries or within interdendritic zones, these particles were most likely precipitated during cooling after solidification.

Several different types of microstructures were formed during aging, all being various forms of precipitation of vanadium containing carbides. These carbides were precipitated on grain boundaries or they had grown out from these, and a certain fraction had precipitated within the grains. The alloys aged at 500 °C and 600 °C were magnetic after aging, indicating that ferrite had formed. This ferrite is assumed to be formed in connection with carbides, in pearlite-like colonies containing both phases. Such colonies were formed at all ageing temperatures, see Figures 4.39, 4.44 and 4.45, but after ageing at 700 °C, 800 °C, 900 °C and 950 °C, no magnetism was associated with them. These colonies are probably a result of cellular precipitation, during which a high growth rate is obtained by element partitioning either by lattice diffusion ahead of the advancing cell front or by diffusion in the moving boundary. [19] During cellular growth, the austenite between the growing carbides will become diluted on the carbide forming elements. If local equilibrium is maintained, this dilution will be stronger the lower the precipitation temperature is due to decreased solid solubility in the austenite. This is also evident from the phase diagram in Figure 5.13. This assumption is also in accordance with what is observed in Figures 4.39, 4.44 and 4.45, i.e. that more cellular carbide phase is formed the lower the transformation temperature is. It is believed that the depletion of alloying elements in the cellular austenite at 500-600 ºC results in a transformation to ferrite and carbide upon cooling. According to the phase diagram in Figure 5.13, ferrite should be present in the alloys at temperatures below about 550 ºC. The solute dilution will facilitate the transformation of the austenite since it reduces the amount of required diffusion (i.e. reduced hardenability). In addition, the heavy dilution on carbon, which is an austenite former, will destabilize the austenite, encouraging the transformation to ferrite. The possibility exists that the diffusion rate during cooling was too slow to allow the transition to ferrite, in which case martensite must have formed instead. At the higher aging temperatures, the solute depletion in the cellular austenite would be less, especially above 800 ºC, see Figure 5.13, preventing any ferrite/martensite formation.

The cellular precipitation got coarser with higher aging temperatures. This is as expected as higher temperatures increase the diffusivity so that the atomic elements, especially substitutionally dissolved elements, can move over longer distances.

Most aging treatments gave a structure that was considered unfavorable, with a high amount of carbides associated with grain boundaries. The most interesting heat treatment was the one of aging at 950 °C for 200 hours. This gave a structure of finely precipitated carbides within

the grains. The carbides appeared round and needle-shaped, with a few microns in width and needle length up to 20 μm. Both the round and needle-shaped carbides appear with the same brightness in the BSD-image (Figure 4.52), so most probably they are of the same composition. The possibility exist that also the particles that appear round, in reality are needle-shaped, with their longitudinal direction forming an angle with the image plane. The formation of needle shaped particles can be a result low diffusivity. For a round particle, continued growth would demand increasingly longer diffusion path for the carbide forming elements, while for a needle-shaped particle the necessary diffusion occurs in a direction normal to the growth direction. The growth can therefore proceed faster. Although some carbide particles were present on the grain boundaries, these seemed not to be continuous. The discontinuous carbides will not be as detrimental to the toughness as a continuous brittle phase. The microstructure of alloy 4 after only austenitizing and quenching, and alloys 2, 3 and 4 after austenitizing, quenching and aging at 950 °C for 200 hours, are most likely comparable with the structures described in Mackay's and Smith's patent [12].

Measured compositions of carbide particles of the type described above are given in Table 4.6. Both carbides on grain boundaries and carbides within the grains are included in the table, and it is seen that they contain chromium, manganese and possibly iron in addition to vanadium. The iron content is uncertain because the steel matrix is expected to contribute to the signal during the WDS analysis because of the relatively small carbide size. From the carbide compositions given in Table 4.6 the chemical formula M_4C can be deduced. This phase does not exist in the phase diagram of Figure 5.13, however, so the composition values given in the table should be adjusted. The simplest adjustment to do is an approximate matrix correction assuming that all the iron in the analyses is a contribution from the steel matrix. The steel matrix is also containing 20 % manganese, so the manganese content in the analyses should be reduced by about 1/4 of the iron content. By normalizing to 100 %, the composition of the analysed carbide particle in alloy 2 is then adjusted to 35 % C, 11 % V, 26 % Cr, 28 % Mn, i.e. $M_{65}C_{35}$, not far from M_7C_3. This is a phase that appears in the phase diagram of Figure 5.13, and it was detected by XRD, see Figure 4.65. Although the above estimate is very rough, and although there are reasons to question the accuracy of the carbon values, it is a reasonable assumption that the coarse carbide particles (1 μm and larger) precipitated during the ageing of the alloys, are of the type M_7C_3, where M probably includes some iron in addition to manganese, chromium and vanadium (a matrix correction that allows some iron in the particle, would adjust its composition towards M_7C_3).

The TEM investigation revealed precipitated particles down to 10 nm in alloy 4 after aging for 200 hours at 800 °C. These precipitates were in Section 4.2.3 identified as as being of the well-known NaCl type vanadium carbide phase. The smallest carbides were always oriented with their cubic unit cell parallel to the austenite unit cell. It is assumed that the obtained hardness increase of the steel matrix during the ageing of the alloys was caused by these small precipitates. Hardness increase in particle precipitated alloys is often explained by coherency strains. Coherency strains have earlier been demonstrated to exist around small VC particles in austenitic steels by Imai and Namekata (for particle sizes up to 16 nm) [14], Ainsley et al. [30] and Sagaradze et al. [31]. Although such strains were hardly observed in the TEM investigation performed in the present work, possibly due to the small particle size, the hardness increase upon ageing is still assumed to be partially caused by coherence strains, partly be the hardness of the carbides by interaction with dislocations.

The presence of a VC carbide phase is conformed by the calculated phase diagram in Figure 5.13. This diagram applies to alloy 2, but a similar diagram containing alloy 4 was also calculated, Figure 5.14, and only some shifts of the lines in the diagrams made the difference. From the diagrams it is evident that VC is a stable phase and could be present in the fully solidified steel at any temperature. A solution treatment, for steels often referred to as austenitization, followed by water quenching will generate an unstable microstructure at lower temperatures. By aging at intermittent temperatures after this process, the steel will accommodate a more stable structure and precipitation of VC, $M_{23}C_6$ and M_7C_3 can be a result. Of these carbides, only $M_{23}C_6$ was not detected in this work. The existence of the VC phase was also established by XRD in two different ageing conditions, see Figure 4.64-4.65.
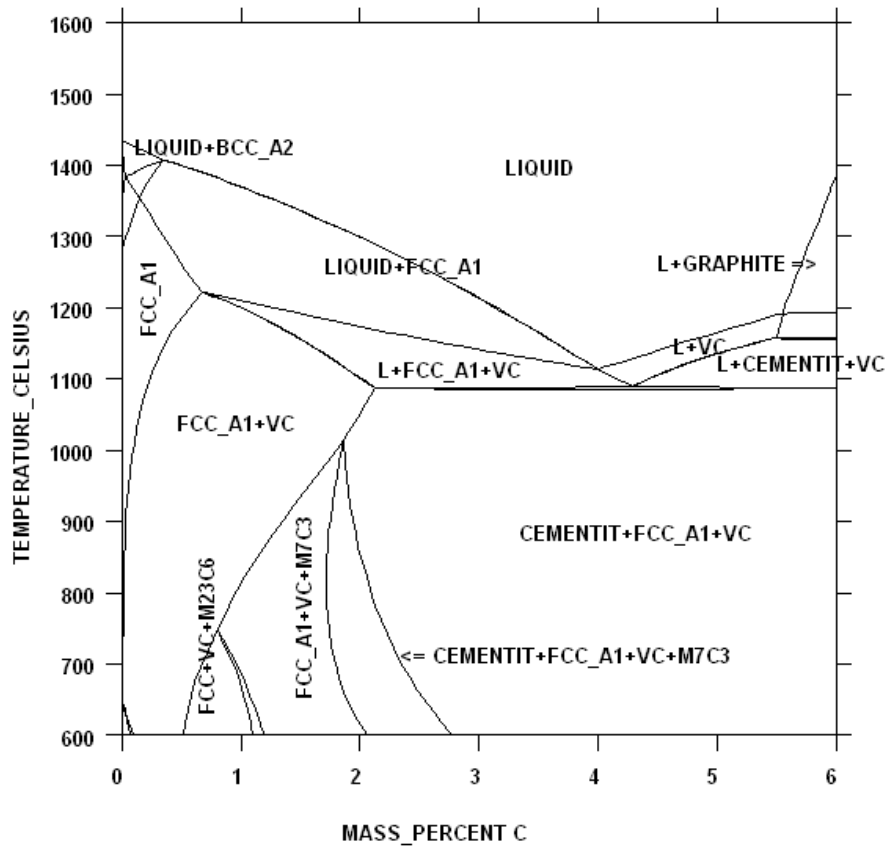
Figure 5.14. Phase diagram for Fe-C-19.1%Mn-2.5%Cr-2.2%V. [29]

The NaCl type of vanadium carbide exists in several modifications, i.e. as VC, V_4C_3, V_6C_5 and V_8C_7 [32], with common notation VC_{1-X}. The stoichiometric VC phase has a perfect NaCl-type crystal structure with vanadium and carbon on separate sublattices. The non-stoichiometric modifications arise when structural vacancies are introduced in the carbon sublattice. This occurs via an order-disorder transition in the temperature range 1100 °C -1300 °C, depending on composition. [33] [15] In V_4C_3 there is one carbon vacancy in the unit cell, e.g. at 000, giving a primitive cubic superlattice with a parameter that is only slightly smaller than that of VC [34] V_6C_5 and V_8C_7 have fewer vacancies on the carbon sublattice, but due to the ordering of vacancies, complex superstructures with large unit cells are generated. V_6C_5 has a monoclinic unit cell with parameters a = 0.509 nm, b = 1.018 nm, c = 0.882 nm, the angle between the a- and c- axes being 109.5° [26]. In steels, the carbides VC, V_4C_3 and V_6C_5 have been reported to precipitate. It seems, however, that some authors have not distinguished between VC and V_4C_3, e.g. in reference [13] where no superstructure reflections are present in

a diffraction pattern from V_4C_3 in an austenitic 13% Mn steel. In other works on manganese steels, e.g. [30] (13%Mn steel) and [31] (20% Mn steel), the precipitated carbides are identified as VC. Both VC and V_4C_3 are mentioned as possible phases in the patent by Mackay and Smith [12], a patent on a vanadium containing Hadfield steel. However, in the latter work, it is referred to "recent work" (no reference is given) suggesting that the precipitated phase is not the stoichiometric VC or V_4C_3, but a more general composition VC_{1-X} where X indicates the extent to which the carbon sublattice is filled. This suggestion is well in line with the present findings. In the present work, carbides up to a few 100 nm in size, Figure 4.60, were identified as V_6C_5, based on their superlattice diffraction spots that partly were streaked in one of the cubic 111 directions. (V_4C_3 would have given superlattice reflection spots halfway between all steel reflections.) The superlattice spots are very weak, and for small particles they are easily overlooked. Thus, there is a large possibility that also the smallest carbides observed in the present work, Figure 4.56-4.57, are of the type V_6C_5. In the XRD analysis, no distinction between the various variants of the NaCl-type vanadium carbide could be made due to the low volume fraction of particles and due to the weakness of the superlattice spots. Only fundamental reflections were recorded by this technique.

In summary, from the above discussion and short presentation of previous experimental result, it might be concluded that the vanadium carbides precipitated in the present steels are not of the frequently reported VC or V_4C_3 phase, but rather V_6C_5. The cross-shaped precipitates that were observed after the austenitizing treatment, are most certainly of the V_6C_5 phase, and there is no reason for believing that the small carbides formed during ageing are of another phase, especially not VC since this is the stoichiometric high temperature phase that is the origin of the various vacancy ordered superstructures that form at temperatures below 1100-1300 °C. [33, 15]

5.2.3 The effect of vanadium carbides on wear resistance

In the aged samples containing vanadium, there is a clear trend that the alloys aged at 500 °C have increased wear resistance with increasing steel matrix hardness. (All hardness indents were made between the carbide particles that could be resolved in the light microscope.) For the alloys aged at 600 °C, there was an increase in hardness for alloys 2 and 4, and alloy 3 had

a negligible hardness change. But the ageing at these temperatures seems to have had little influence on the wear resistance compared to the resistance after the austinitizing treatment. After aging at 700 °C, 800 °C, 900 °C and 950 °C the wear resistance decreased with increasing (matrix) hardness. As the correlation between hardness and abrasion wear resistance is generally accepted, there must be another effect increasing the weight loss after aging at higher temperatures. In all alloys at most aging temperatures and times there are developed an unfavorable microstructure, with either heterogeneously formed carbides and/or cellular structures containing carbides and austenite/ferrite. These cells were typically formed in conjunction with grain boundaries. There is known that austenite is more abrasion resistant than ferrite, pearlite and martensite of the same hardness due to a higher strain-hardening rate and a higher ductility. [35] The ability of high strain-hardening is in fact the basic property of the austenitic manganese steel. For this reason, the cellular precipitation resulting in ferrite formation in the alloys aged at 500 °C and 600 °C is expected to be unfavorable for the wear resistance.

It was expected that an analysis of the wear surfaces would answer some of the questions raised above. This analysis showed that the dominant abrasive wear mechanism was ploughing, creating furrows and grooves in the wear surface. In the wear surface of the reference Strømhard alloy, the furrows were wider and deeper than in the vanadium containing alloy 4 (aged at 950 °C). This is a somewhat surprising result since the Strømhard alloy experienced a lower weight loss than alloy 4 after aging at high temperatures. The reason for this apparent contradiction may be that some smearing and sticking occurred in the softer Strømhard wear surface, so that worn material was not efficiently removed. In the precipitate-hardened alloy, more shallow furrows were formed, but due to higher brittleness, less smearing and more efficient removal of worn material could have taken place.

Crushing and removal of coarse carbides that formed during prolonged ageing could be the reason for the observed increase in wear with increased ageing time at the higher ageing temperatures. However, the analysis of the wear surfaces revealed that these carbides had very little impact on the wear of the alloys. Only occasionally, debris of vanadium containing carbide particles had fallen out, forming craters in the wear surface. And compared to the furrows and grooves, these craters represented only a small fraction of the total weight loss. The reduced wear strength with ageing at high temperatures is therefore not caused by crushing of coarse carbides formed during ageing.

Generally, an increase in hardness is expected to be accompanied by an increase in wear resistance. However, in this investigation, the increased matrix hardness obtained during ageing did only give increased wear strength after ageing at the lowest ageing temperature, i.e. 500 °C. The obtained hardness increase is most likely caused by the fine precipitation of V_6C_5 (or VC) that has been verified for the ageing temperature 800 °C. The reason why these particles did not give a general increase in wear strength may be the result of an existing balance between wear resistance offered by small particles and wear resistance offered by carbon in solid solution (in combination with manganese). It is known from earlier work that particles that are precipitated to obtain increased hardness can, during abrasion, be shared if they are coherent, or fail to block dislocations if they are incoherent. [35] The positive effect of the smallest carbide particles can therefore have been limited, and in fact lost if the precipitation extracted so much carbon from solid solution that the well-known positive effect of solute carbon on the wear strength of austenitic manganese steels was too much reduced. It is expected that the amount of precipitated carbides did increase with temperature and time during ageing. This would result in increased carbon depletion in the austenite lattice with increased ageing temperature and time, which does explain the obtained wear results.

Table 4.7 gives some carbon concentration values that were measured in the steel matrix after ageing at 950 °C. The decreased carbon level in the matrix compared to the total carbon concentration in the steel is mainly a result of the relatively coarse M_7C_3 precipitation which occurred during the ageing, see Figure 4.52 for alloy 2. These carbides have reduced the carbon contents in the matrix by some 1/10 weight% during ageing at 950 °C for 200 hours (i.e. 0.2-0.7 %), and the residual matrix carbon concentrations are lower than for the reference alloy. The carbon concentrations given in Table 4.7 include the carbon precipitated within the small vanadium carbide particles. Thus, the austenite lattice will contain even less carbon than what is read from the table.

Rough estimates of the dilution in carbon solute due to the precipitation of carbides can be done from the crystallographic data for the involved phases. The lattice parameter of austenite is 0.367 nm [25], and it contains 4 metal atoms per unit cell. The lattice parameter of the cubic *fundamental* unit cell of V_6C_5 can be approximated with the lattice parameter of VC, i.e. 0.421 nm [25], and it contains 3.33 carbon atoms. Several modifications of M_7C_3 exist, but it is reasonable to apply the unit cell parameters for Mn_7C_3, being orthorhombic with parameters

a = 0.6959 nm, b = 11.976 nm, c = 4.546 nm and containing 12 carbon atoms [36.] Furthermore, the atom weight of carbon is 12, and the average atom weight of the austenite metal atoms is taken as 55. Applying these values, it is easily calculated that, per volume percent of precipitated M_7C_3, respectively V_6C_5, the carbon solute in the austenite lattice is reduced by about 0.08 weight % and 0.12 weight %. The latter value is adjusted to 0.15 % if VC is assumed precipitated. A volume fraction of 9 % M_7C_3 would then reduce the matrix concentration of carbon in alloy 4 by 0.8 weight % to about 1.1 weight %, which corresponds well with the value given in Table 4.7 for alloy 4 aged at 950 °C for 200 hours. A volume fraction in the order of 9-10 % is a reasonable estimate when the particle density in Figure 4.52 is considered. The volume fraction of V_6C_5 has not been measured, but knowing that the detection limit of XRD is in the order of 1 mass %, some few volume % of V_6C_5 can be assumed. (The cross-shaped V-carbides are not expected to contribute to the XRD peaks because their volume is much less than 1 %.) A carbon solute content below 1 weight % can therefore be expected as a result of the ageing. This is, however, a much higher value than what can be read from the phase diagram in Figure 5.1. According to this diagram, the solubility of austenite at 950 °C is about 0.2 weight %, so equilibrium has probably not been reached during the ageing. A solute concentration of 0.2 weight % C would have been reached in alloy 4 if V_6C_5 precipitated in an amount of 7-8 volume % during ageing for 200 hours at 950 ºC (0.91 weight % reduction from the carbon concentration given in Table 4.7). This high value can be excluded taken the low XRD peaks into consideration (a comparable amount of M_7C_3 gave much higher peaks).

Anyway, the above estimates show that a strong reduction in the amount of solute carbon will result from the carbide precipitation during ageing. This is the probable reason for the reduction in wear resistance that in general was obtained after ageing. The precipitated carbides were too small to give an increase in wear strength that exceeded the loss in wear strength caused by the reduction in dissolved carbon in the austenite lattice. An exception from this general trend was observed after aging at 500 °C when an increase in wear resistance was observed upon ageing. May be this "low" temperature resulted in less precipitation and less carbon dilution so that a net positive effect was obtained. After 600 °C ageing, the positive and negative effects of the precipitation cancelled each other, giving essentially no effect on the wear strength.

Precipitation or addition of larger particles could, however, have a positive effect on wear resistance depending on their size compared to the size of the abrasive medium. To be effective, the hard particles in the wear component should be larger than the abrasive grains. If they are considerably smaller than the abrasive grains, the particles can be removed together with the matrix. In the present abrasive wear test, the abrasive grains were approximately 200 μm in size. Thus, being much smaller than the abrasive grains, the alloy carbides have most likely been removed together with the matrix without giving wear resistance. This view applies even to the relatively large M_7C_3 carbides that precipitated within the grains during the ageing.

In summary, carbon in solid solution in the austenite has a high effect on the wear resistance of manganese steel. If the effect of the precipitated carbides is lower than the effect of carbon in solid solution, the result of the carbide precipitation will be a reduced wear resistance. The effect of large abrasive media and small precipitated carbides combined with the depletion of carbon in solid solution is undoubtedly the reason of the poor wear resistance in the aged vanadium-modified alloys. After austenitization, the vanadium-modified alloys seemed to have equal to better wear resistance than the reference alloy of Strømhard steel. This thesis has been focused on a way to increase the wear resistance in the Strømhard steel without defining the outer conditions during use. Abrasive media, temperature, speed, deformation mode, load and corrosive effects are among several parameters that will affect the ability of the alloy to resist wear. Wear of any of these experimental alloys in an industrial application might be completely different from the wear result obtained in this work.

6   Conclusion

The conclusions based on this work are as follows:

- With the correct amount of additions of cerium and aluminum grain refinement of an austenitic high manganese steel is attainable, as long as the other influencing parameters are within favorable conditions.

- Increased wear resistance may be achieved in vanadium modified Strømhard steel by austenitization at 1180 °C for 4 hours, followed by water quenching and aging at 500 °C for 8 hours to 24 hours.

- Fine precipitates of vanadium carbides in an austenitic manganese steel may be obtained with the correct heat treatment, but this will be followed by a certain amount of carbides on the grain boundaries.

- Nano-sized VC or V_6C_5 was found in a vanadium added alloy after aging. These gave a hardness increase by coherence strains or by pinning the dislocations.

- Precipitated vanadium carbides do not necessarily improve the abrasive wear resistance in an austenitic manganese steel. The efficiency of the hard phase will depend on the external conditions that the wear component is exposed to.

Proposal for further work

The effect of the grain refiner should be tested in industrial scale. A larger volume of melt will most likely have an effect on the as-cast grain structure. The amount of EGR and aluminum additions should be optimized for the industrial production, and the effect of variation in oxygen and sulfur content of the steel should be investigated. A more thorough investigation of the inclusions formed by the cerium additions can give an answer to which particle that has the best effect on grain refinement of austenitic manganese steels.

The effeciency of a second phase in austenitic manganese steel can only truly be tested in the actual setting. To have a conclusive answer if these have a positive effect, full scale trials have to be conducted. Continued electron microscopy work can give a better characterization of the phases precipitated during aging of vanadium alloyed manganese steel.

References

[1]   R. Hadfield, "Manganese steel", Oliver and Boyd ltd., Edinburgh, UK, 1956.

[2]   D.K. Subramanyam, "Austenitic manganese steel", Metals Handbook 10. Edition, volume 1, "Properties and selection: stainless steels, tool materials and special-purpose metals", ASM International, 1995.

[3]   K.O. Gjerde, "Arbeidsherdings- og slitasjemekanismer for austenittisk Mn-stål", hovedoppgave, Høgskolesenteret i Rogaland, 1991.

[4]   George E. Dieter, "Mechanical metallurgy", McGraw-Hill Book Company, 1988.

[5]   R.C. Tucker, "Wear failures", Metals Handbook 9. Edition, Volume 11, "Failure analysis and prevention" ASM International, 1986.

[6]   D.L. Olson, C.E. Cross, "Friction and wear in the mining and mineral industries", ASM Handbook, Volume 18, "Friction, lubrication and wear technology", ASM International, 1992.

[7]   D.K. Subramanyam, "Austenitic manganese steel", Metals Handbook 10. Edition, volume 1, "Properties and selection: stainless steels, tool materials and special-purpose metals", ASM International, 1995.

[8]   P.H. Adler, G.B. Olson, W.S. Owen, "Strain hardening of Hadfield manganese steel", Metallurgical transactions A, Volume 17A, p 1725-1737, 1986

[9]   Y.N. Dastur, W.C. Leslie, "Mechanism of work hardening in Hadfield manganese steel", Metallurgical transactions A, Volume 12A, p 749-759, 1981

[10]   B.K. Zuidema, D.K. Subramanyam, W.C. Leslie, "The effect of aluminum on the work hardening and wear resistance of Hadfield manganese steel", Metallurgical transactions A, Volume 18A, p 1629-1639, 1987

[11] F. Borik and W.G. Scholz, "Gouging abrasion test for materials used in ore and rock crushing, part II", Journal of materials, Vol 6 (No. 3), 1971, p 590-605.

[12] W.B. Mackay and R.W. Smith, "Hadfield's steel containing 2% vanadium", United States Patent 4,377,422, Queen's University at Kingston, 1983.

[13] O.A. Atasoy, K. Ozbaysal, O.T. Inal, "Precipitation of vanadium carbides in 0.8% C-13% Mn-1% V austenitic steel", Journal of materials science 24, 1989, p 1393-1398.

[14] Y. Imai, J. Namekata, "Precipitation behaviours of austenitic steel of manganese-chromium type containing vanadium", The research institute for iron, steel and other metals, 1970.

[15] T.B. Massalski, "Binary alloy phase diagrams", American Society for Metals, Metals Park, 1986

[16] Handbook of ternary alloy phase diagrams, ASM International, 1995.

[17] W. Kurz, D.J. Fisher, "Fundamentals of solidification", Trans tech publications ltd., 1998.

[18] John Campbell, "Castings", Elsevier, 2004

[19] D.A. Porter, K.E. Easterling, "Phase transformations in metals and alloys", Nelson Thornes Ltd, Cheltenham, UK, 2001

[20] B.L. Bramfitt, Metall. Trans., 1, 1970, p 1987-1995.

[21] Ø. Grong, P. Jonsson, O.S. Klevan, "The future role of ferroalloys in iron and steel", The Ninth International Ferroalloys Congress and the Manganese 2001 Health Issues Symposium, Quebec City, Canada, 2001, p 562-572.

[22]   H. Figenschuh, "Einfluss von kornfeinenden zusätzen auf korngrösse und mechanische eigenshäften umwandlungsfreier austenitischer und ferritischer stahlgusslegierungen", Dr.Ing. avhandling, Technischen Universität Berlin, 1980.

[23]   C. Eijk, J. Walmsley, Ø. Grong, O.S. Klevan, "Grain refinement of fully austenitic stainless steels using a Fe-Cr-Si-Ce master alloy", 59th Electric Furnace and 19th Process Technology Conferences, Phoenix AZ, 2001.

[24]   Casper van der Eijk, "Progress in the development and use of grain refiner based on cerium sulfide or titanium compound for carbon steel.", ISIJ International Volume 49, No.7 Special Issue, 2009.

[25]   P. Villars, L.D. Calvert, "Pearsons handbook of crystallographic data for intermetallic phases", Volume 2 and 3, American Society for metals, 1985.

[26]   J. Billingham, P. S. Bell, and M. H. Lewis, Phil. Mag. **25**, 1972, p. 661.

[27]   A.L. Greer, A.M. Bunn, A. Tronche, P.V. Evans, and D.J. Bristow, "Modelling of inoculation of metallic melts: Application to grain refinement of aluminium by Al-Ti-B", Acta Mater. **48,** 2000, p. 2823-2835.

[28]   A. Tronche and A.L. Greer, "Electron-backscatter diffraction study of inoculation of Al", Philos. Mag. Lett. **81,** 2001, p. 321-328.

[29]   Thermo-Calc Software, www.thermocalc.com.

[30]   M.H. Ainsley, G.J. Cocks, D.R. Miller, "The ageing characteristics of an austenitic Fe-13Mn-2V-0.8C alloy", Scripta metallurgica, Vol. 14, p. 539-543.

[31]   V.V. Sagaradze, I.I. Kositsyna, M.L. Mukhin, Y.V. Belozerov, Yu.R. Zaynutdinov, "High-strength precipitation-hardening austenitic Fe-Mn-V-Mo-C steels with shape memory effect", Materials science and engineering A 481-282, 2008, p. 747-751.

[32]   A.I. Gusev and A.A. Rempel, "Superstructures of Non-Stoichiometric Interstitial Compounds and the Distribution Functions of Interstitial Atoms", phys. stat. sol. (a) **135,** 1993, p. 15-58.

[33]   K. Hiraga, "Vacancy ordering in vanadium carbides based on V_6C_5", Phil. Mag. **27,** 1973, p. 1301-1312.

[34]   H. Liu, J. Zhu, Y. Liu, and Z. Lai, "First-principles study on the mechanical properties of vanadium carbides VC and V_4C_3", Materials Letters **62,** 2008, p. 3084-3086.

[35]   Joseph H. Tylczak, "Abrasive wear", ASM Handbook, Volume 18, "Friction, lubrication and wear technology", ASM International, 1992.

[36]   J.P. Morniroli and M. Gantois, "Etude Microstructurale de Carbures M_7C_3", J. Appl. Cryst. **16,** 1983, p. 1-10.

Appendix 1

Hardness measurements before and after aging, from the vanadium modified Strømhard steel and the reference steel.

Austenitized							Average	STDEV
12	296	279	279	276	291	297	286	9,4
25	299	307	275	272	294	318	294	18,0
26	284	287	265	312	281	307	289	17,4
27	308	327	319	329	313	324	320	8,2
28	312	307	305	299	298	314	306	6,6
29	279	273	265	283	258	285	274	10,6
13	297	302	294	289	290	285	293	6,1
35	330	326	321	329	318	337	327	6,8
36	317	301	294	297	284	296	298	10,8
37	296	292	298	292	290	283	292	5,2
38	320	340	310	289	323	319	317	16,8
39	330	308	320	312	314	306	315	8,8
14	269	285	279	259	263	272	271	9,7
45	309	358	359	283	300	356	328	34,1
46	342	358	330	331	324	352	340	13,5
47	323	328	316	332	327	329	326	5,6
48	277	307	322	297	285	318	301	18,0
49	394	398	347	331	379	334	364	30,2

Aged 8 h								
12	296	279	279	276	291	297	286	9,4
25	341	360	346	361	338	372	353	13,4
26	383	359	387	376	385	395	381	12,3
27	429	438	434	432	443	446	437	6,6
28	368	387	389	383	389	379	383	8,1
29	328	351	331	359	322	343	339	14,4
13	297	302	294	289	290	285	293	6,1
35	369	370	362	379	322	339	357	21,8
36	343	300	347	323	320	334	328	17,3
37	373	380	385	419	369	414	390	21,3
38	325	344	359	354	331	301	336	21,4
39	389	400	346	392	375	400	384	20,6
14	269	285	279	259	263	272	271	9,7
45	344	387	325	350	374	351	355	22,1
46	402	423	406	415	410	430	414	10,6
47	472	470	493	471	469	466	474	9,8

							Average	STDEV
48	436	429	410	377	372	362	398	31,5
49	406	376	401	374	387	367	385	15,7

Aged 24 h							Average	STDEV
12	296	279	279	276	291	297	286	9,4
25	422	427	415	402	393	398	410	13,8
26	366	350	358	360	363	341	356	9,3
27	453	444	441	453	452	419	444	13,1
28	383	385	356	369	364	375	372	11,2
29	338	390	387	341	309	322	348	33,6
13	297	302	294	289	290	285	293	6,1
35	366	364	359	365	386	325	361	19,9
36	264	273	303	284	303	310	290	18,6
37	453	441	453	382	403	427	427	28,8
38	371	380	393	331	388	383	374	22,5
39	416	386	400	452	419	407	413	22,4
14	269	285	279	259	263	272	271	9,7
45	351	363	366	359	375	418	372	23,9
46	404	437	392	442	391	390	409	24,0
47	478	505	486	460	463	484	479	16,5
48	416	413	458	400	459	472	436	30,1
49	451	408	439	454	404	447	434	22,2
950-0 (8)								
2	365	364	392	389	384	402	383	15,3
3	354	347	337	365	337	355	349	11,0
4	375	424	400	423	386	398	401	19,6
950-0 (200)								
2	372	327	342	355	340	333	345	16,3
3	370	371	381	384	392	369	378	9,3
4	374	389	396	407	410	399	396	13,1
950-8								
2	349	343	348	348	328	352	345	8,7
3	361	354	364	367	366	385	366	10,3
4	387	362	372	365	361	369	369	9,6
950-200								
2	436	424	393	426	430	438	425	16,4
3	323	384	433	433	351	372	383	44,1
4	506	495	504	498	515	484	500	10,6

110

Appendix 2

Chemical analysis of cerium based particles in the castings added EGR, from the EPMA.
The size of the particles is in the last column.

Atomic ratio

Casting	Al	O	Fe	S	Mn	Ce	Phase	Size
8	0,0000	62,0042	3,7396	0,1863	0,8861	33,1838	CeO2	4,5
8	0,0019	53,4298	8,5905	4,8538	2,0457	30,9327	CeO2	2
8	0,0000	48,1108	18,5919	2,8898	4,6491	25,7584	CeO2	1
8	0,0247	54,4474	15,2327	0,0793	3,7699	25,9957	CeO2	1
8	0,0000	56,9910	8,9437	0,1230	2,4423	31,2199	CeO2	1
8	0,0118	65,4021	3,8103	0,0958	1,0965	29,3303	CeO2	2,5
8	0,0901	58,3536	4,5449	0,2374	0,9655	35,5300	CeO2	3
8	4,1840	55,1836	4,6566	0,0804	1,0445	32,7742	CeO2	2
8	0,0000	47,1060	25,7001	0,5165	5,3762	20,7775	CeO2	1
8	0,0045	58,2868	7,1272	0,0834	1,6642	32,6845	CeO2	1
8	0,0329	59,7804	5,3497	0,5359	1,6399	31,7651	CeO2	2,5
8	0,0083	60,0803	5,8428	1,7296	1,7834	30,5556	CeO2	0,5
8	0,0000	58,3156	7,4990	0,3457	1,6662	31,5398	CeO2	1
8	0,0000	59,8117	5,7911	0,2831	1,2892	32,6798	CeO2	1,5
8	0,0000	56,7357	7,6265	1,0761	1,5844	31,2494	CeO2	0,7
8	0,0950	70,1780	3,8737	0,6720	0,9763	23,8867	CeO3	3
8	0,0224	58,8183	4,4484	0,3491	1,0539	35,0332	CeO2	1
8	0,0000	61,3343	4,5724	0,0197	1,1362	32,9374	CeO2	2
8	0,0000	65,8618	3,6904	0,3457	0,9840	28,8260	CeO2	2,5
8	0,0000	60,1545	3,9405	0,4471	1,1669	34,1113	CeO2	1,5
								1,6
	Al	O	Fe	S	Mn	Ce	Phase	Size
5	0,0121	63,7567	3,4740	0,0000	0,6988	32,0050	CeO2	2
5	0,0164	61,5513	4,2156	1,8644	1,2837	31,0324	CeO2	1
5	0,8860	59,7760	5,6070	0,0070	1,2341	30,9952	CeO2	2,5
5	0,0222	62,5622	6,3879	0,5091	1,4754	29,0336	CeO2	1
5	0,0000	41,4542	9,2063	12,4766	2,0706	34,4668	Ce2O2S	3
5	0,0000	60,7237	4,6260	0,1387	0,9130	33,5987	CeO2	1,5
5	1,1492	58,6138	6,9492	0,0704	1,6234	26,4040	CeO2	0,75
5	0,0000	50,4395	5,3631	9,5333	1,0004	33,1262	Ce2O2S	1
5	0,0000	51,1693	21,9231	0,0660	4,9292	18,3612	CeO2	1,5
5	0,0000	56,2493	6,3367	0,1526	1,2985	35,4673	CeO2	1
5	0,0000	52,8912	11,2016	3,7591	2,4002	29,4558	CeO2	1,5
5	0,0000	55,6989	5,1331	3,7389	1,0404	34,3844	CeO2	3
5	0,0000	57,8677	7,7991	1,3310	1,5850	30,9258	CeO2	1
5	0,0000	55,1954	9,1842	0,0333	2,3834	33,0107	CeO2	1
5	0,0000	59,2082	10,6342	1,5997	2,2597	26,1970	CeO2	2,5
5	0,0000	59,5556	5,4060	0,4819	1,1792	33,3470	CeO2	1
5	0,0000	60,9690	4,3124	0,2777	1,1575	33,1036	CeO2	1,5

	Al	O	Fe	S	Mn	Ce	Phase	Size
5	0,0000	60,7715	4,1336	0,8796	1,0678	33,1475	CeO2	3
5	0,0441	55,0804	11,6958	0,1545	2,7502	29,6427	CeO2	1
5	0,0000	60,3282	6,3326	2,7446	1,3991	28,4411	CeO2	1,25

	Al	O	Fe	S	Mn	Ce	Phase	1,6 Size
7	14,1004	56,6761	4,1572	2,9819	1,2274	20,5012	CeAlO3	1
7	13,1805	55,9249	7,3719	1,4093	1,9690	17,9864	CeAlO3	1
7	8,4540	45,3486	16,6614	2,4083	4,3137	22,1986	CeO2	0,8
7	14,9937	56,9712	3,7592	2,3483	0,8562	20,6263	CeAlO3	1
7	7,6733	48,9870	10,2471	5,9098	2,3897	24,6979	Ce2O2S	0,75
7	8,0816	45,7451	4,6512	9,3098	1,8403	29,0593	Ce2O2S	2
7	1,2596	36,6699	12,2213	13,6446	3,4364	31,6368	Ce2O2S	1
7	13,1608	57,1587	5,9653	2,6604	1,5609	19,3939	CeAlO3	1,25
7	0,0642	34,8451	13,1929	15,2362	2,9625	33,6034	Ce2O2S	1,5
7	6,7082	54,1705	6,3475	4,8962	1,5511	25,9874	CeO2	1
7	16,0630	60,2560	4,8936	0,0605	0,9866	17,6015	CeAlO3	0,75
7	10,5027	45,1338	10,7212	5,6633	5,0760	22,8947	CeO2	1
7	0,5937	30,5975	18,4331	13,4960	4,0286	32,8511	Ce2O2S	0,5
7	5,1822	48,1379	12,7968	4,1038	3,5374	23,6639	CeO2	1
7	2,0755	32,5316	20,0705	12,7332	6,6576	25,9316	Ce2O2S	1
7	12,5726	51,6568	9,4407	3,2095	2,5924	20,2490	CeAlO3	1
7	0,3335	32,8395	17,4441	11,8126	5,5272	28,2016	Ce2O2S	0,75
7	9,1919	52,0237	9,8104	4,3226	2,1927	22,4020	CeAlO3	1,5
7	10,5376	48,1413	9,2529	4,8362	4,5184	22,0534	CeAlO3	1,5
7	18,9859	40,5227	4,4044	3,2846	2,3841	28,7958	CeAlO3	3

	Al	O	Fe	S	Mn	Ce	Phase	1,2 Size
4	1,3726	42,5755	9,9842	12,0054	3,0507	30,3906	Ce2O2S	2,5
4	8,4427	47,8448	11,4378	5,8400	2,7875	23,4996	CeO2	1
4	0,1264	36,9091	9,7068	14,5072	3,1158	35,6116	Ce2O2S	1,5
4	0,0000	30,8322	24,2594	12,1542	5,8546	26,6714	Ce2O2S	1
4	14,4385	59,1677	6,4195	0,1032	1,4218	17,9798	CeAlO3	1,5
4	2,3164	47,4077	17,2716	2,9707	4,2149	24,8002	CeO2	1
4	4,8378	57,2287	4,1053	0,0623	1,8213	25,9409	CeO2	1
4	14,0791	61,1464	3,7278	0,1431	0,8646	19,6288	CeAlO3	1
4	0,5556	63,1174	3,4770	0,3383	1,1752	31,1422	CeO2	1
4	5,3818	51,4261	5,0200	7,1890	1,0316	29,1142	CeO2	1,5

	Al	O	Fe	S	Mn	Ce	Phase	1,3 Size
3	15,4765	58,4437	5,4697	0,0070	1,2452	17,4428	CeAlO3	1
3	15,5005	58,4814	6,3133	0,0000	1,4296	17,0309	CeAlO3	1
3	14,7053	57,0639	7,5186	0,0000	1,6702	17,1448	CeAlO3	1
3	16,1543	55,4370	5,8415	0,0000	1,6458	18,5136	CeAlO3	0,75
3	16,2083	60,2771	4,2622	0,0000	1,0643	17,3450	CeAlO3	1,5
3	15,7913	45,6024	13,8028	0,0132	3,3428	16,3222	CeAlO3	0,5
3	15,0688	55,6081	8,2273	0,0000	1,8523	17,5547	CeAlO3	0,8
3	15,6987	58,1936	4,7902	0,0070	1,4261	17,5787	CeAlO3	1,5
3	14,9451	60,2601	2,9219	0,0000	1,4171	17,3184	CeAlO3	1

112

	Al	O	Fe	S	Mn	Ce	Phase	Size
3	14,0317	51,6455	12,4073	1,5848	4,0318	15,4994	CeAlO3	0,8
								1,0
6	1,1803	39,8742	10,0085	13,3939	2,1927	33,3457	Ce2O2S	1
6	1,3302	53,9359	6,1017	6,0322	2,3960	29,7427	CeO2	1
6	6,5428	58,5217	8,3800	0,3214	2,6156	22,0018	CeO2	1,5
6	3,0740	57,4759	7,9170	2,4562	2,1412	25,6688	CeO2	1
6	3,1804	52,4557	4,9075	5,9332	1,3441	32,0154	CeO2	1,5
6	5,8615	61,1061	5,8967	0,0010	1,4042	24,1285	CeO2	2
6	9,7830	60,1868	6,8186	0,7705	1,4559	20,2228	CeAlO3	1,5
6	14,6764	61,7247	3,4866	0,4333	0,9341	17,9939	CeAlO3	4
6	5,7587	61,1471	2,8255	3,5084	1,3099	22,3130	CeO2	3
6	1,2172	43,5212	5,7580	13,7999	1,8781	33,3863	Ce2O2S	1
								1,8

Appendix 3

XRD-mappings of cerium type particles in the castings added EGR, acquired in the EPMA.
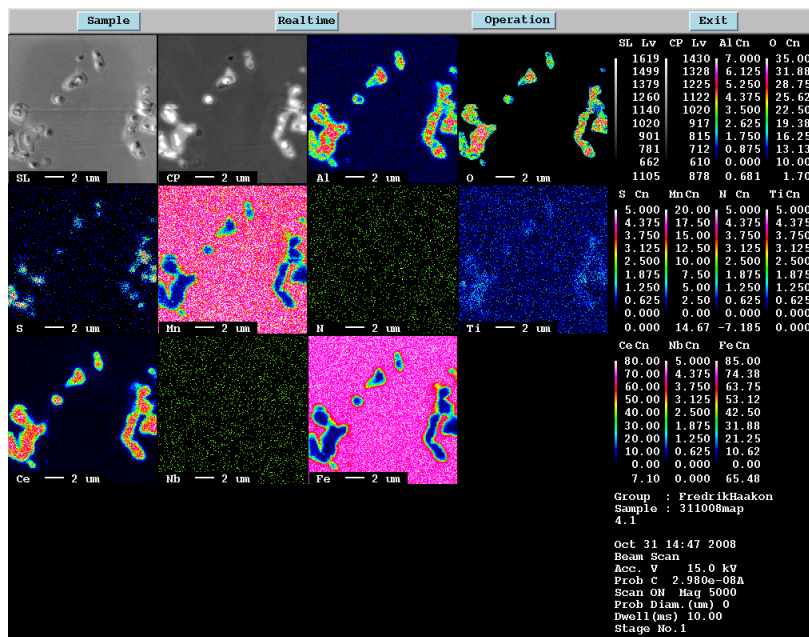
Figure A-1. Casting 4.
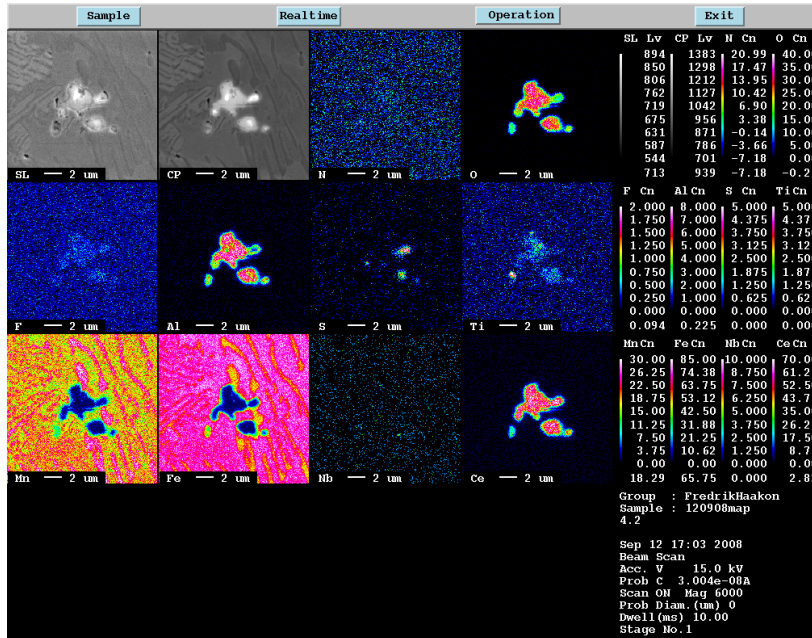
Figure A-2. Casting 4.
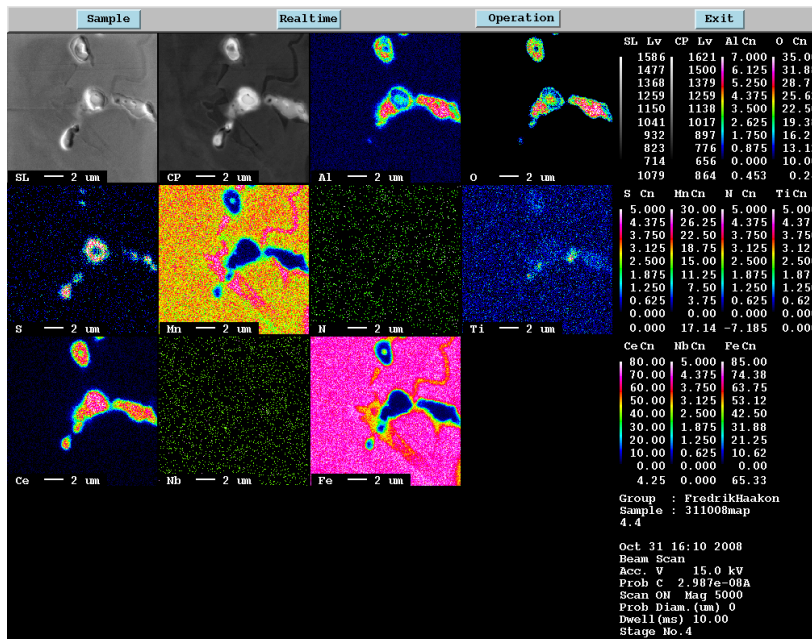
Figure A-3. Casting 4.

115
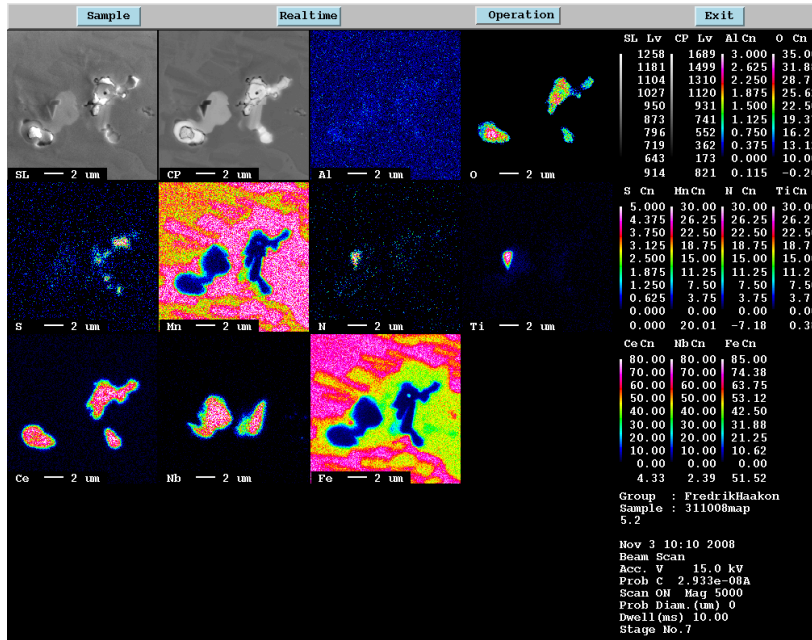
Figure A-4. Casting 5.
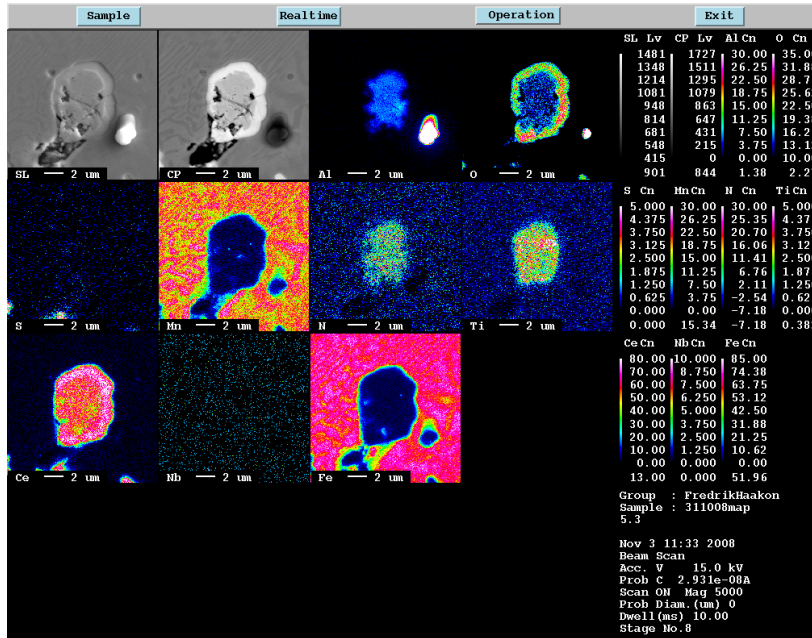
Figure A-5. Casting 5.
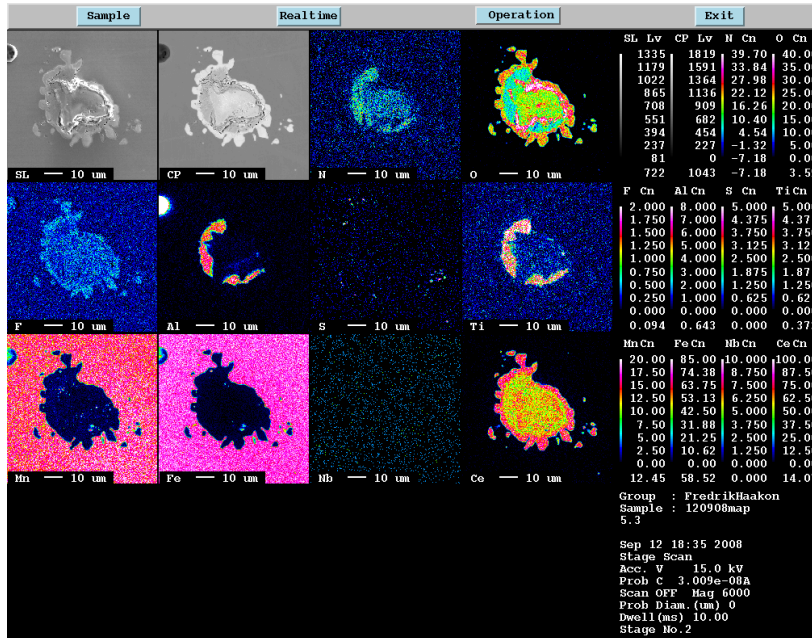
Figure A-6. Casting 5.
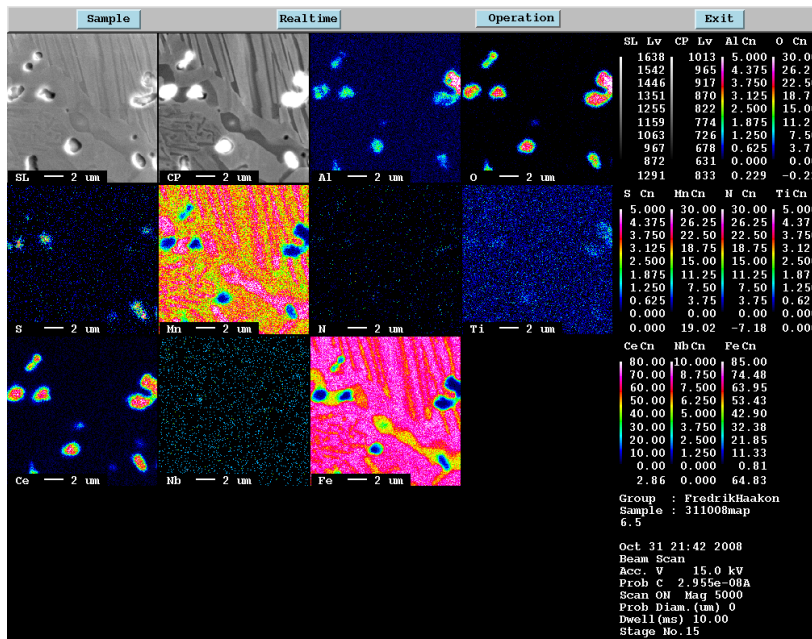
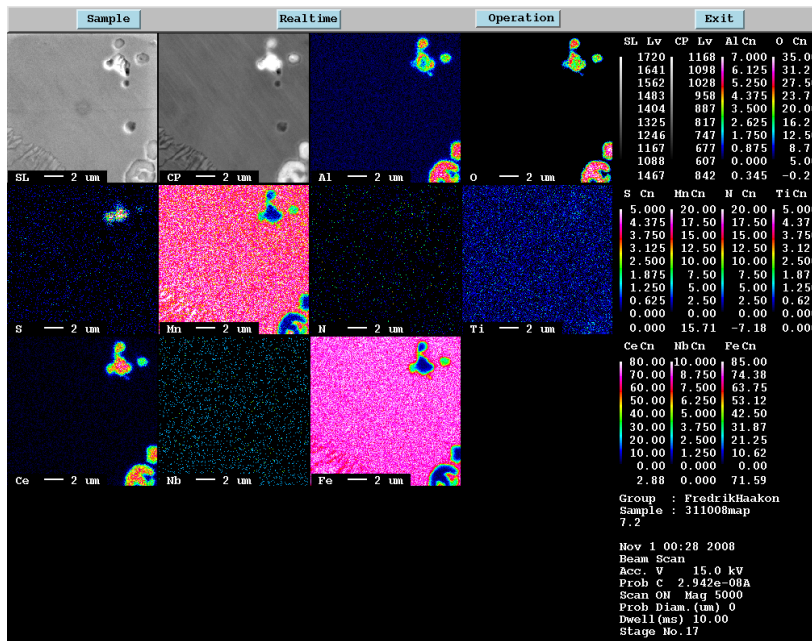**Figure A-7. Casting 6.**

117
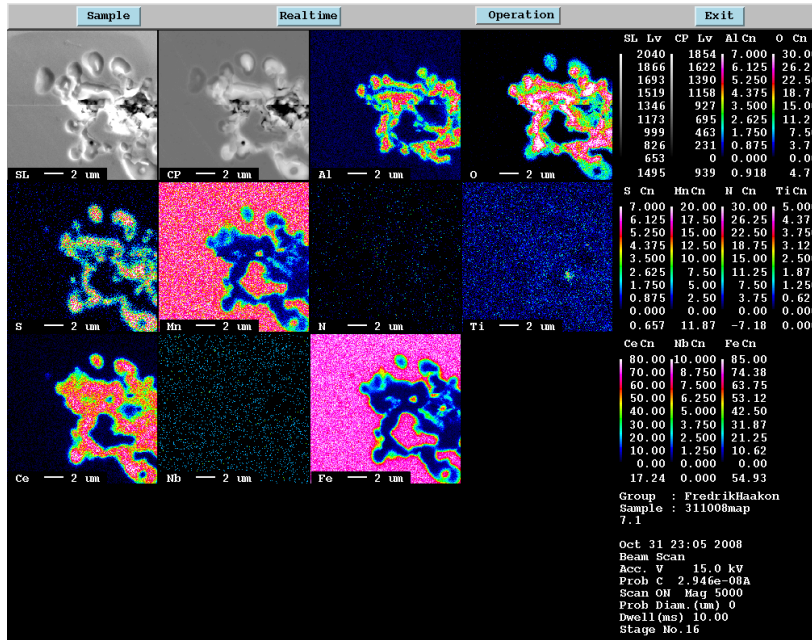
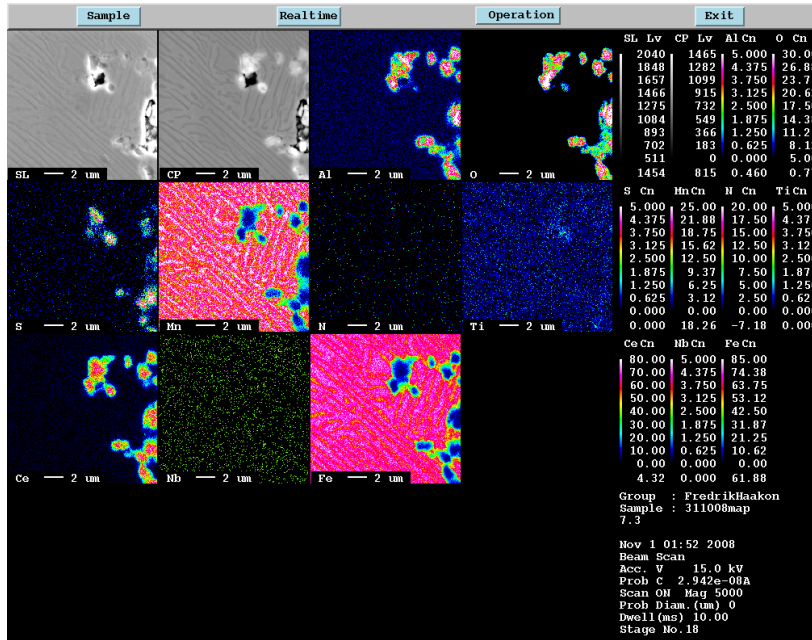**Figure A-8. Casting 7.**
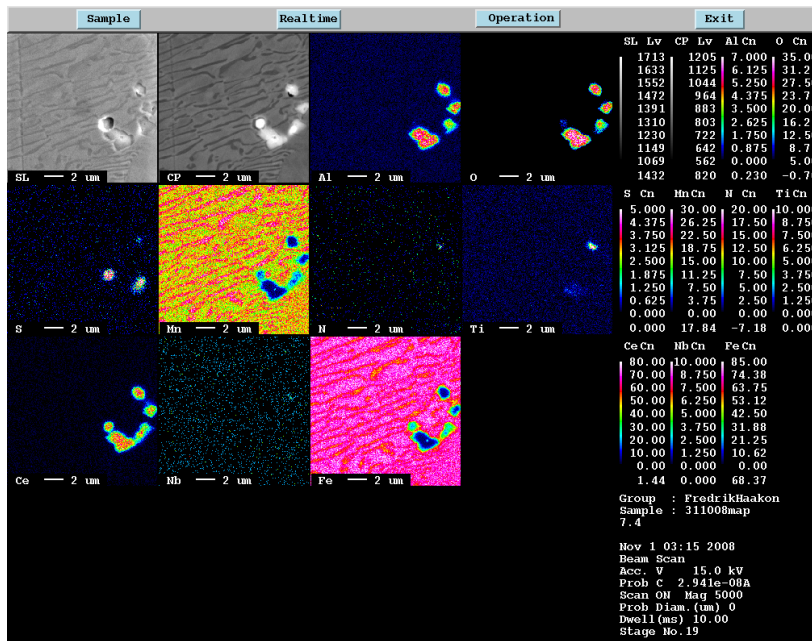

Figure A-9. Casting 7.
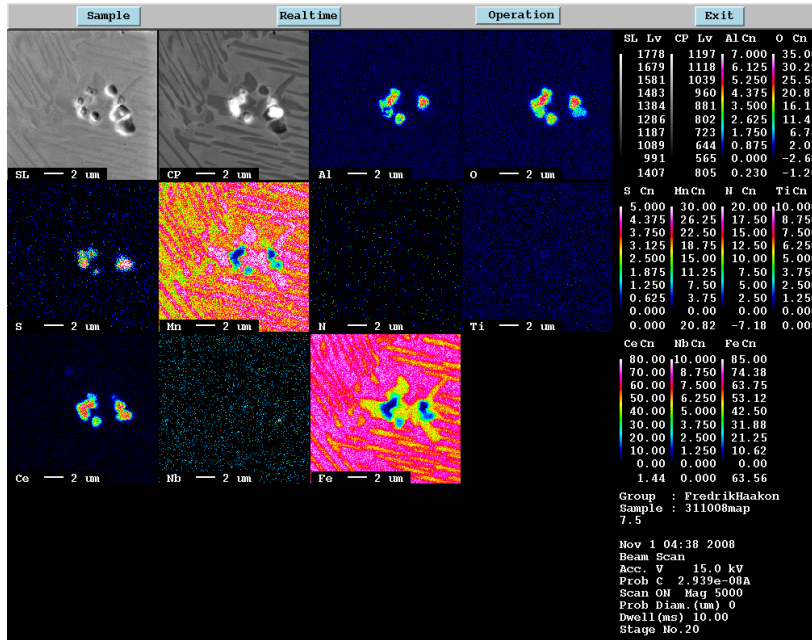
Figure A-10. Casting 7.
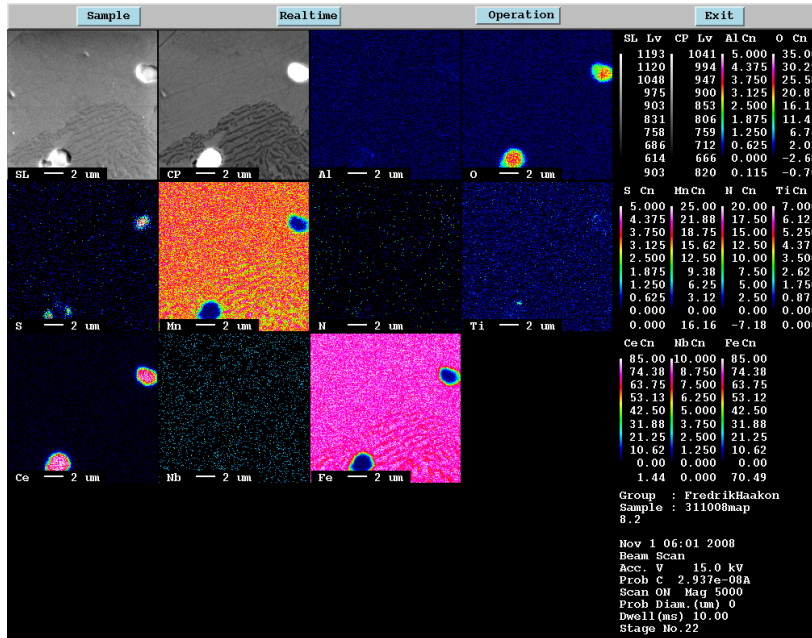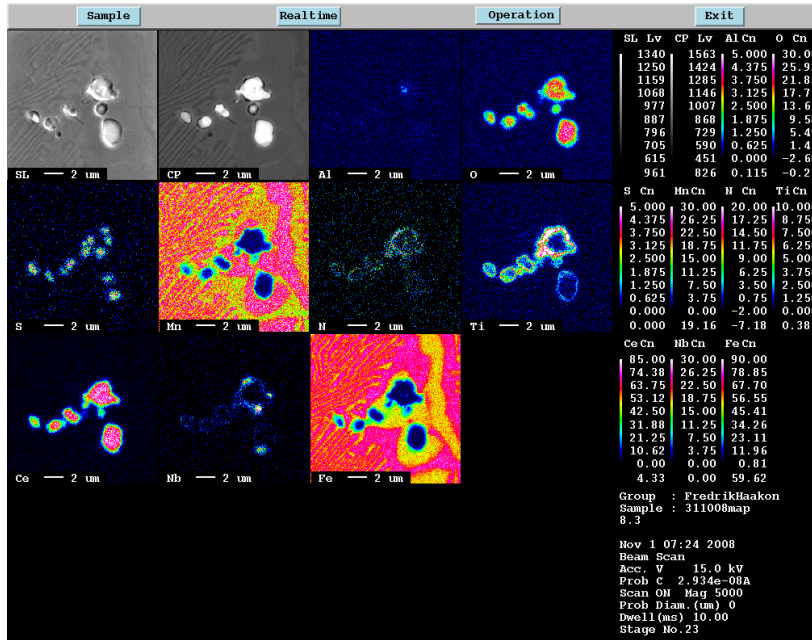

Figure A-11. Casting 7.

Figure A-12. Casting 7.

Figure A-13. Casting 8.
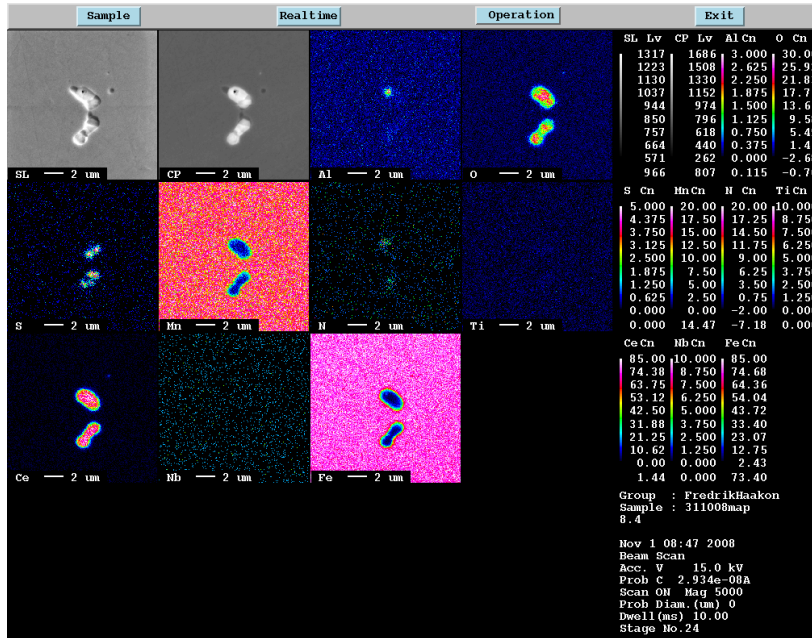
120

Figure A-14. Casting 8.
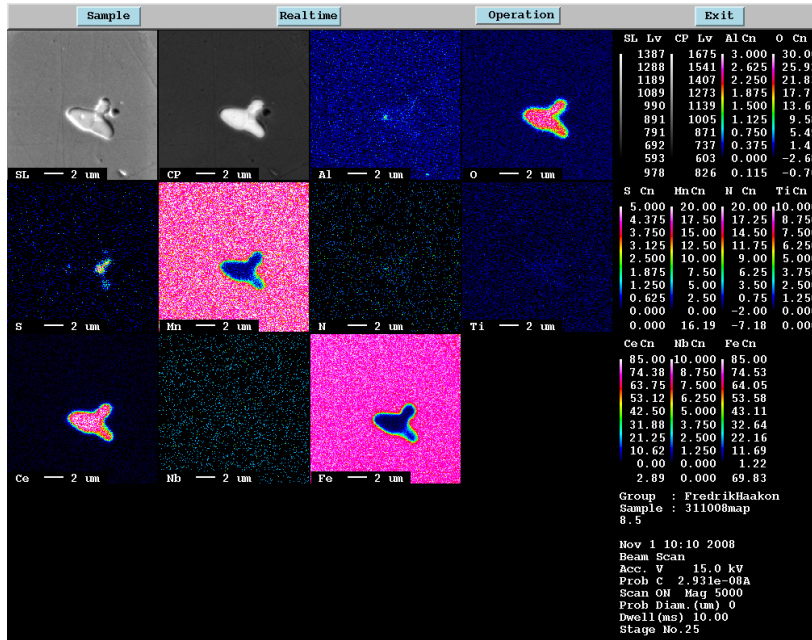

Figure A-15. Casting 8

Figure A-16. Casting 8.

Appendix 4

Line scan results from the EPMA to detect decarburization in the aged samples. The sample is alloy 3 aged at 950 °C for 200 hours.